Title
Rare Earth Element Biosorption onto Bacterial Surfaces in Engineered and Soil Systems

Author
Chang, Elliot Suk-Hyun

Publication Date
2020

Peer reviewed|Thesis/dissertation

Rare Earth Element Biosorption onto Bacterial Surfaces in Engineered and Soil Systems

by

Elliot Suk-Hyun Chang

A dissertation submitted in partial satisfaction of the

Requirements for the degree of

Doctor of Philosophy

in

Environmental Science, Policy, and Management

in the

Graduate Division

of the

University of California, Berkeley

Committee in charge:

Laura N. Lammers, Co-Advisor

Céline Pallud, Co-Advisor

Arash Komeili

Mary Firestone

Fall 2020

ABSTRACT

Rare Earth Element Biosorption onto Bacterial Surfaces in

Engineered and Soil Systems

by

Elliot Suk-Hyun Chang

Doctor of Philosophy in Environmental Science, Policy, and Management

University of California, Berkeley

Bacterial surfaces can be used in engineered systems through the implementation of bioreactors as unconventional means of extracting critical metals. This dissertation discusses a genetically modified gram-negative bacterium, dLBTx8 induced *Escherichia coli*, which possesses lanthanide binding tag peptides that chelate and preferentially adsorb rare earth elements over other co-existing metals. A thermodynamic surface complexation model was first built to compare the cell surface terbium binding mechanisms of wild type and dLBTx8 engineered *E. coli* (Ch. 2). This surface complexation model was then expanded upon to include adsorption of yttrium and thirteen lanthanide elements (Ch. 3). The engineered dLBTx8 *E. coli* cells were immobilized in a non-sorbing polyethylene glycol diacrylate (PEGDA) polymer and packed into fixed-bed columns to demonstrate proof-of-principle bioreactor designs. A one-dimensional reactive transport model incorporating advective inter-bead and diffusive intra-bead transport of lanthanides was developed to account for the complex competitive adsorption processes taking place within the dLBTx8 *E. coli* packed fixed-bed column. After careful calibration and testing of the reactive transport model, predictions were made to optimize separation of valuable rare earths, exemplified by europium vs. lanthanum separation. This dissertation demonstrates the power of surface complexation and reactive transport modeling to allow for future engineering designs that can improve the efficacy of rare earth element bio-extraction and separation from geothermal fluid and mining leachate feedstocks.

Bacterial surfaces can also play an important role in soils, surface water, and subsurface geologic systems, where the cell surface-based ligands can adsorb various metals. Due to the reactive nature of their cell surfaces, bacteria can influence fate, transport, and mobility of naturally occurring and anthropogenically introduced metals in soils. While many scientists have investigated the adsorption of divalent metals, such as lead and copper, onto bacterial surfaces found in soils and sediments, a knowledge gap currently exists in understanding how trivalent lanthanides impact these dynamic subsurface transport processes. In general, soil bacterial surfaces have been shown to have particularly strong electrostatic interactions with rare earths, implying that these trivalent metals can act as important controls over the transport of divalent metals. In this dissertation, a gram-positive soil bacterium, *Arthrobacter nicotianae*, has been shown to adsorb lanthanides through multiple different surface complexation mechanisms, including phosphodiester, phosphoryl, carboxyl, and carbonyl-based amide binding (Ch. 4). These results, supported through attenuated total reflectance Fourier transform infrared spectroscopy measurements (ATR-FTIR), are qualitatively corroborated by thermodynamic modeling of the bacterial cell wall. Notably, the modeling results suggest the relatively high affinities imposed by

each of these site types, particularly through phosphate and amide monodentate adsorption. This work contributes to the currently existing knowledge gap whereby soil transport of divalent metals may significantly be affected by the presence of even low concentrations of trivalent rare earth elements.

LIST OF PUBLICATIONS

Paper 1 (Chapter 2):

Chang, Elliot, Aaron W. Brewer, Dan M. Park, Yongqin Jiao, and Laura N. Lammers. 2020. "Surface complexation model of rare earth element adsorption onto bacterial surfaces with lanthanide binding tags." *Applied Geochemistry* 112 (May 2019): 104478. https://doi.org/10.1016/j.apgeochem.2019.104478.

Paper 2 (Chapter 3):

Chang, Elliot, Aaron W Brewer, Dan M Park, Yongqin Jiao, and Laura N. Lammers. 2020. "Selective biosorption of valuable rare earth elements among co-occurring lanthanides." *Environmental Engineering Science* 00 (00): 1–11. https://doi.org/10.1089/ees.2020.0291.

Paper 3 (Chapter 4):

Chang, Elliot. Laura N. Lammers, Céline Pallud. "*Arthrobacter nicotianae* adsorption of neodymium to investigate multi-site surface complexation mechanisms of gram-positive soil bacteria." [Manuscript in preparation].

CONTENTS

FIGURES

TABLES

ACKNOWLEDGEMENTS

I extend my deepest thanks to Dr. Laura N. Lammers for her guidance during my Ph.D. program. We grew and learned in tremendous ways together through mutual respect, care, and honesty. I would also like to thank my committee co-chair, Dr. Céline Pallud, for her mentorship which allowed me to explore the last chapter of my dissertation more richly and fully. Thank you to my committee members, Dr. Mary Firestone and Dr. Arash Komeili, for their critical feedback and vital support from the start of my dissertation work. This work was made possible through the research funding provided by the U.S. Department of Energy, Office of Energy Efficiency and Renewable Energy, Geothermal Office and by the National Science Foundation Graduate Research Fellowship Grant No. 1752814.

On a personal level, I express deep gratitude to my parents, Mi Ok and Bill Chang, for their steadfast, unflinching support during my Ph.D. work, and my brother Paul Chang, for his loving humor and friendship. To my godparents, Elizabeth and Dr. Morgan Tench, I express a special thanks for inspiring me to pursue this degree and to always dream bigger. Thank you to my partner, Jana Lee, for her love, comfort, and dedication.

CHAPTER 1

Introduction: Reactive cell walls of bacteria and their propensity to adsorb rare earth elements

1.1 Reactivity of bacterial surfaces

Bacteria have existed on Earth for 3 billion years and are considered the oldest known forms of life on this planet (Cavalier-Smith, Brasier, and Embley 2006). In present time, bacteria are commonly found in soils and sediments roughly on the order of 10^7 to 10^{10} cells/gram (Raynaud and Nunan 2014). There are a wealth of different kinds of bacteria in nature, ranging from those that can use biomineralization (Bayer and Bayer 1991) as a de-toxification mechanism to others that can re-orient themselves based on the Earth's magnetic field (Komeili 2012). Despite this incredible diversity, one strong commonality exists across all strains: the bacterial surface. The surfaces of bacteria act as the interface between the living microbial organism and the environment. Whether it be pore water from soils, surface water from streams, or engineered solutions from bioreactors, the bacterial surface plays an important role in the control and transport of metals in both natural and engineered systems.

The bacterial surface possesses many different functional groups, including carboxyl, phosphate, hydroxyl, and amine groups. Dating back to a study by Gram (1884), scientists have used a staining procedure to distinguish between two large groups of bacteria based on their fundamental structural differences in the cell envelope. The surfaces of gram-negative bacteria consist of outer membranes and thin peptidoglycan layers, which often possess a wealth of carboxyl and hydroxyl groups (Texier et al. 2000) in the form of lipopolysaccharides. The surfaces of gram-positive bacteria, which lack outer membranes, are mostly made up of thick peptidoglycan layers, containing carboxyl, hydroxyl, and amide functional groups in the form of N-acetylmuramic acids and N-acetylglucosamines. While some of these sites are unavailable for metal binding due to their role as cross-linking units, many are still present as anionic functional groups. Wall teichoic acids (WTAs) are covalently anchored to the thick peptidoglycan mesh and can make up 60% by weight of the cell wall (Ellwood 1970). The repeating units that make up the anionic glycopolymer WTA chains are each linked by phosphodiester moieties that can readily adsorb counter ions such as magnesium (Thomas and Rice 2015). Furthermore, WTAs not only participate in charge neutralization, but also play a critical role in regulating cell division and cell shape structure (Brown, Santa Maria, and Walker 2013). While the WTAs have an abundance of phosphodiesters, gram-positive bacteria possess phosphate groups that also consist of phosphoryl sites. To this end, phosphoryl moieties are most notably present on the polar heads of phospholipids that make up the bilipid plasma membrane. In this dissertation, I investigate *Escherichia coli* as a model gram-negative bacterium and *Arthrobacter nicotianae* as a model gram-positive bacterium. I demonstrate in this work how the two bacteria can be modeled differently to obtain more accurate characterizations and interactions between their surface moieties and the metals present in the surrounding environment.

1.2 Lanthanide chemistry in the environment

Rare earth elements (REEs) have become increasingly important in today's society. In particular, REEs are now highly contested critical materials for their application in the world

production of sustainable energy and high-technology advancements (Kamenopoulos, Shields, and Agioutantis 2015). Although not all REEs are rare due to their natural abundance in the earth's crust, elements such as neodymium and europium tend to exist only in low concentrations in minable ore deposits (Long et al. 2012). Thus, it behooves us to better understand the geochemistry of REEs present in natural systems. To this extent, REEs are most commonly investigated in soils, minerals, and subsurface geologic solutions.

REEs can form a wide variety of mineral phases, ranging from phosphates to carbonates and silicates (Tyler 2004). While some minerals, such as pyrochlore, can be rich in light rare earth elements (lanthanum, cerium, praseodymium, neodymium) (Chakhmouradian 1996), others, such as zircon, are enriched in heavy rare earth elements (erbium, thulium, ytterbium, lutetium) (Watson 1980). Furthermore, soil alterations that cause fluctuations in pH, water fluxes, aqueous composition, and secondary intermediate minerals, lead to large changes in REE abundance (Price et al. 1991). Despite the wide range of REE concentrations and compositions that can be found in natural solutions, soils, and sediments, a few important thermodynamic trends control the underlying geochemistry of these metals. Lanthanides possess partially filled 4f shells and filled 5s, 5p, 5d, and 6s subshells (Cotton 2006), making them particularly large in ionic radii and dense in charge. As the atomic number increases, the charge density also increases, resulting in a lanthanide contraction effect whereby ionic radius decreases. This contraction is quite stark, with the middle lanthanides having ionic radii comparable to Ca^{2+}. Due to this unique lanthanide contraction effect, many REEs can readily displace Ca^{2+} present in biological systems, such as the counter-ions on the outer membrane of gram-negative bacteria (Peng et al. 2004). Lanthanides also act as strong Lewis acids, coordinating with highly electronegative donors and forming tightly bound complexes with organic compounds found in soils, such as siderophores (Emmanuel et al. 2012; Ahmed and Holmström 2014). As discussed previously, bacterial surfaces also possess a wealth of different anionic functional groups. Due to these sites having naturally high electrostatic interactions with trivalent REEs (Fein, Martin, and Wightman 2001; Ngwenya et al. 2009), bacterial surfaces can strongly influence the transport of lanthanides in soils and plants (Tyler 2004) as well as in minerals and rock substrates (Zaharescu et al. 2017).

REEs found in the environment also possess complex aqueous speciation. While all REEs are most commonly found in their +3 oxidation state in natural soil and subsurface geologic conditions, they tend to form strong aqueous complexes with many co-occurring anions, ranging from fluoride, chloride and hydroxide ions to carbonate, sulfate, bicarbonate, nitrate, and orthophosphate ions (Haas, Shock, and Sassani 1995). Although aqueous speciation strongly depends on the pH and chemical composition of the solution, REE complexation is most commonly controlled by Cl^- and F^- under acidic and neutral pH conditions, respectively, and REE precipitation is controlled by OH^- at neutral to basic pH conditions. Furthermore, light REEs (LREEs) complex strongly with chloride ions whereas heavy REEs (HREEs) form particularly stable complexes with fluoride ions. These important differences in speciation behavior contribute to the complexity of REE geochemistry in soils and subsurface hydrothermal solutions.

1.3 Importance of bacterial surfaces in engineered applications and soil systems

REE biosorption onto bacterial surfaces has been studied for the past two decades (Texier et al. 2000; Andrès, Le Cloirec, and Texier 2003; Takahashi et al. 2005; Ngwenya et al. 2009; Martinez, Pourret, and Takahashi 2014). Many of these studies have implemented time-resolved laser-induced fluorescence spectroscopy (TRLFS) and extended X-ray absorption fine structure

(EXAFS) spectroscopy to elucidate the binding mechanisms underlying the macroscopic batch adsorption process. However, these mechanisms have not been rigorously translated into surface complexation models that allow for predictions of REE adsorption given variations in geochemical parameters, such as pH, solution composition, and metal loading. For example, while Ngwenya et al. (2009) develops a model for gram-negative *Pantoea agglomerans* bacterial adsorption of lanthanides, a significant shortcoming is presented due to single-site modeling whereby only single-site carboxyl adsorption or phosphoryl adsorption is accounted for. In reality, the bacterial surface has multiple different site types simultaneously participating in REE binding, making multi-site complexation models essential in describing the competition of various site types for REEs.

To address this knowledge gap, I investigate the single- and multi-site adsorption reactions present in naturally occurring wild-type *E. coli* and engineered dLBTx8 induced *E. coli* cell surfaces (Chapter 2). The engineered dLBTx8 induced *E. coli* (Park et al., 2016) poses an interesting case study for multi-site adsorption because the cell surface, in conjunction with its naturally occurring surface moieties, has been modified to also express lanthanide binding tag peptides on the outer membrane protein A. Through surface complexation modeling of acid-base titration data and terbium (Tb) batch adsorption isotherms, I demonstrate the importance of allowing multiple sites to simultaneously adsorb REEs. While certain adsorption mechanisms may dominate at low surface excess, others may only become relevant at higher metal loadings when high-affinity sites become saturated. This study illustrates how multiple site types can compete for Tb binding at various pH and metal loading conditions, posing strong implications for what mechanisms control REE adsorption on the cell surface. Ultimately, a trade-off is presented between the low-concentration, high-affinity engineered site type and the high-concentration, low-affinity naturally occurring functional groups.

In Chapter 3, I further build upon this model to investigate the influence of multi-site adsorption on the selective separation of heavy and light REEs. Because many REEs co-exist together in feedstocks, such as geothermal fluids and mining leachates (Park et al., 2017), it is essential to characterize the competitive surface adsorption reactions of all relevant REEs. This work avoids using unconstrained optimization of REE binding constants for carboxyl- and lanthanide binding tag-based adsorption reactions because these algorithms may lead to overparameterization. Instead, linear free energy relationships are implemented to ground the modeling effort in chemical principles based on thermodynamic trends. Chapter 3 also expands upon the engineering applications of dLBTx8 induced *E. coli*. Specifically, I focus on the model characterization of fixed-bed columns designed for extraction of REEs (Aaron Brewer et al. 2019) by utilizing a one-dimensional reactive transport modeling approach. Advective inter-bead and diffusive intra-bead transport provide an accurate physical description of the dual-porosity flow process and the previously described linear free energy relationships incorporate chemical descriptions of the bacterial surface adsorption reactions taking place with each of the REEs. Upon calibration and testing of the model, predictions were made to optimize separation of REEs in the hopes of obtaining higher value extractants. Europium (Eu) vs. lanthanum (La) separation dynamics were investigated, with Eu exemplifying a valuable, critical metal and La exemplifying a less precious metal.

While Chapters 2 and 3 explore bacterial surface-rare earth metal adsorption dynamics for a gram-negative bacterium, Chapter 4 discusses the different binding mechanisms that influence rare earth metal adsorption onto gram-positive bacteria. The lack of an outer membrane in gram-

positive strains affects the way we model and characterize the cell surface. Notably, modeling efforts over the past two decades have not incorporated stability constants or binding mechanisms attributed to phosphodiester moieties present in the wall teichoic acids that are anchored onto the thick peptidoglycan layer. In this chapter, attenuated total reflectance fourier transform infrared spectroscopy (ATR-FTIR) measurements provide important qualitative constraints to multi-site surface complexation modeling. Adsorption of neodymium (Nd), another valuable rare earth metal, is studied by varying metal loading and pH conditions. Acid-base titrations are again implemented to understand the protonation behavior and site concentrations of the relevant adsorbing site types. A carbonyl-based amide binding mechanism is also observed on the bacterial surface. As trivalent REEs are strong Lewis acids that draw in negative charge, neutrally charged carbonyls on amide groups are transformed into negatively charged $C\text{-}O^-$ sites that are readily available for favorable electrostatic interactions with REEs. A resonance mechanism based on lone pair and pi bond electron movement is suggested (Sigel and Martin 1982; Edington et al. 2018), providing an explanation for the large contributions of carbonyl-based amide binding as measured by IR difference spectra. To incorporate this mechanism, I developed a novel surface complexation model for gram-positive bacteria that simultaneously incorporates carboxyl, phosphodiester, phosphoryl, and amide adsorption reactions. Multi-site modeling outputs provide valuable insights into the competitive adsorption behavior of each of these site types whereby different functional groups have varying optimal chemical regimes for controlling the overall batch REE adsorption process. These findings demonstrate the disproportionate contribution of both phosphodiester and amide functional groups, particularly at the low REE surface loadings most relevant to natural soils and sediments.

Presented together, these three body chapters and the dissertation as a whole fill a knowledge gap in the thermodynamic understanding and surface chemistry governing rare earth metal biosorption onto bacterial surfaces. Novel modeling efforts to characterize engineered fixed-bed column designs and to elucidate REE adsorption dynamics of naturally occurring soil bacteria highlight the widespread relevance and applicability of this work.

CHAPTER 2

Surface complexation modeling of lanthanide binding tag induced *Escherichia coli* to characterize terbium biosorption onto the bacterial cell wall

2.1 Introduction

Rare earth elements are essential for clean energy technologies (e.g. wind turbines), consumer products (e.g. smartphone batteries), and military applications (e.g. defense missiles) (Du and Graedel 2011; Alonso et al. 2012; Tukker 2014). In producing REEs, conventional extraction and mining methods can be energetically and chemically intensive, harming the environment through waste production and high energy usage. Liquid-liquid extraction, for example, separates rare earths from other metals based on the reagents' increased selectivity for the lanthanides relative to the other metals. This process, however, can be chemically intensive due to the large amount of organic solvents used in each partitioning step. Rare earth ore deposits consist of mixtures containing variable proportions of REEs (Alonso et al. 2012), including the lanthanides, scandium, and yttrium; in general, however, the heavy lanthanides (HREEs) are of greatest economic importance (Dent 2012). The extraction and separation of these specific REEs is costly. In response to these technological challenges and associated environmental impacts, we have recently engineered bacteria with high selectivity for REEs, particularly the HREEs, found in geothermal brines and mining leachates (Park et al., 2016, 2017).

The geochemical behavior of the REEs is characterized by their complex speciation behavior, complicating their separation from natural fluids. While all REEs are found predominantly in the +3 oxidation state under Earth surface conditions, they form strong aqueous complexes with numerous anionic species including fluoride, chloride and hydroxide, as well as carbonate, sulfate, bicarbonate, nitrate, and orthophosphate (Haas, Shock, and Sassani 1995). Speciation depends strongly on the pH and chemical composition of the source hydrothermal fluids, and in general REE complexation is controlled by Cl^- at acid pH and REE precipitation is controlled by OH^- at neutral to basic pH. The aqueous complexation of REEs tends to increase with increasing temperature, which mobilizes these elements in hydrothermal fluids. Importantly, the REEs can form strong complexes with organic acidic functional groups, particularly carboxylate sites (Kolat 1970). This property leads to the relatively high affinity of REEs for natural microbial cell surfaces (Moriwaki and Yamamoto 2013), but genetic engineering of the cell surface has been demonstrated to effectively enhance REE adsorption, particularly for the separation of valuable HREEs, in complex solutions (D. M. Park et al. 2017).

Scientists have begun expressing lanthanide binding tags (LBTs), short peptides with high affinity for REEs, on bacterial cell surfaces to selectively bind trace rare earth metals (D. M. Park et al. 2016; 2017). LBT affinity for REEs has been tested under rapid luminescence detection (Nitz et al. 2004) and NMR spectroscopy (Martin et al. 2007). Nitz et al (2004) show that the Terbium (Tb^{3+}) - LBT complex is in a state of eight coordination by monodentate oxygen ligands of aspartic acid (Asp)1, asparagine (Asn)3, and Asp5, bidentate carboxyl ligands from glutamic acid (Glu)9 and (Glu)12, and the backbone carbonyl group of tryptophan (Trp)7. An analysis of the electrostatic potential further shows a neutrally charged Tb^{3+}-LBT complex despite the positively charged terbium ion and the multitude of negatively charged ligands. The high affinity of the LBT towards rare earths stems from its chemical binding environment, where the peptide-based ligands exclude water from the first coordination sphere. Martin et al (2007) report another reason for the lanthanide binding tag's high rare earth affinity: the tag is able to mediate alignment between the

lanthanide ion and the protein to dramatically lower the mobility of the complex. Both Nitz and Martin argue for enhanced binding of trivalent rare earths through a unique steric effect between the protein ligands and the metal.

To determine mechanisms of enhanced REE biosorption on engineered cell surfaces, REE complexation by wild type (e.g., non-engineered) cell surfaces must first be understood. Bacteria cell walls are complex and contain multiple types of functional groups, including carboxyl, hydroxyl, phosphoryl (Fein et al. 1997), sulfhydryl (Yu and Fein 2015; Mishra et al. 2017), and amine groups (Borrok, Turner, and Fein 2005; Guiné et al. 2006). Rare earth element biosorption onto bacterial surfaces has been shown to be predominantly controlled by carboxyl and phosphoryl functional groups (Texier et al. 2000; Markai et al. 2003; Ngwenya et al. 2009; 2010). Findings from time-resolved fluorescence spectroscopy (Texier et al. 2000; Markai et al. 2003; Ozaki et al. 2006) suggest that lanthanide biosorption onto the wild type cell surface occurs through inner-sphere carboxylate binding. Furthermore, Ngwenya et al (2009) show through EXAFS that phosphoryl groups dominate sorption at lower pH while carboxyl groups dominate sorption at higher pH. Texier et al (2000) and Takahashi et al (2005) both suggest that rare earths form inner-sphere complexes with both carboxylate and phosphoryl groups. More specifically, Ngwenya et al (2010) show that the phosphoryl groups dominate sorption of light and middle rare earths while carboxylate coordination may be favored for some middle and heavy lanthanides. Thus, surface complexation mechanisms vary even within the rare earth series. Moreover, because prior experiments were performed over a limited range of concentrations and surface loadings, the relationship between loading and complexation has not been well studied.

Surface complexation modeling (SCM) has previously been used to characterize REE sorption onto cell surfaces (Markai et al. 2003; Ngwenya et al. 2010). Markai et al (2003) and Ngwenya et al (2010) both use SCM to fit carboxyl-REE or phosphoryl-REE stability constants to experimental sorption edge data ranging from pH 3 to 6.5. Prior to sorption edge modeling, potentiometric titrations, which informs the protonation state of each site type at a given pH, were modeled to obtain pK_a values for carboxyl, phosphoryl, and hydroxyl functional groups. These values typically range from 2-6, 5.65-7.20, and 9.6-10.8 for carboxyl, phosphoryl, and hydroxyl functional groups, respectively (Hong and Brown 2006). Both studies implement a one-site carboxyl or phosphoryl constant capacitance model in an attempt to best-fit results to experimental sorption edge data. A variety of SCMs have been shown to successfully capture REE sorption as a function of pH: both a one-site carboxyl model and a one-site phosphoryl model can adequately fit the sorption edge data.

The current study presents sorption isotherm results and implements a surface complexation model for Tb^{3+} adsorption onto engineered bacterial surfaces. Our objective is to develop an SCM that accurately models Tb biosorption onto *E. coli* bacteria both with or without LBTs, allowing us to compare the affinities of wild type and LBT surface site types for Tb. This study presents results from sorption isotherm experiments at a constant pH of 6, the pH of maximum REE adsorption (Park et al., 2016), allowing us to deduce stability constants at the studied pH that apply for a wide range of different metal concentrations in solution. In this manner, we illustrate how addition of different site types due to LBT engineering can alter sorption capacity and the cell surface's affinity for Tb under varying metal loadings and pH. This becomes relevant as feedstock from geothermal fluids and mining leachates have highly variable rare earth concentrations. Finally, we will show the partitioning of Tb binding onto different site types over

a range of aqueous Tb concentrations, illustrating how a quasi-mechanistic sorption model could be applied to an engineered bioreactor setup with a wide range of REE inlet concentrations.

2.2 Methods

2.2.1 Cell preparation and harvesting

For a full description of LBT expression see Park et al (2017). Briefly, the *E. coli* strains harboring a *lpp-ompA*-dLBTx8 expression plasmid was grown in LB media supplemented with 50 μg/mL ampicillin. Expression of *lpp-ompA*-dLBTx8 was induced at mid-exponential phase using 0.002% arabinose for 3 h at 37 °C. Wild type, un-induced (WT) cells contained the *lpp-ompA*-dLBTx8 expression plasmid but were not treated with arabinose. Cells were harvested by centrifugation at 4,000 x*g* for 10 min, washed once in 10 mM MES (2-(N-morpholino)-ethanesulfonic acid) pH 6, and normalized by wet weight for acid/base titrations. Cell suspension densities ranging from 108 to 125 wet grams/L and 32 to 48 wet grams/L were obtained for wild type *E. coli* and dLBTx8 *E. coli*, respectively. Wild type and dLBTx8 cells were massed as wet cell pellets before baking for 24 hr at a temperature of 65 °C. The dry mass of cells were then measured to obtain wet:dry mass ratios for both strains of *E. coli*.

2.2.2 Acid/base titration of wild type (WT) and dLBTx8 induced (LBT) strains of E. coli

Triplicate acid-base titrations were conducted on wild type (WT) and dLBTx8 (LBT) strains of *E. coli* cells harvested at mid-exponential phase. The solution was initially acidified with 0.1 M HCl to a pH of 3.5. The bacterial suspension was purged with N_2 gas for thirty minutes before and throughout the titration. A base titration using 0.1 M NaOH titrant was conducted at room temperature using a Titronic 300 automatic titrator. A monotonic equivalence point titration method was used to add the same volume of titrant at each step. This study focuses on a pH range of 3.5–10.0. pH below 3.5 has been shown to irreversibly damage bacteria by displacing structurally bound Mg and Ca (Borrok, Fein, and Kulpa 2004; Borrok, Turner, and Fein 2005). Although bacterial surfaces have been cited to have substantial buffering capacity below our studied pH range (Fein et al. 2005), our current titrations avoid lower pH values in order to determine proton and cation exchange properties of surface functional groups on undamaged bacterial cell surfaces. A post-titration bacterial suspension was centrifuged and its supernatant (no biomass) was used to blank-correct all of the net proton charge data (Figure 2.1, 2.2) in order to obtain proton charge values of only the bacterial cell surface. Raw titration data were converted to net proton charge values using the expression (Sposito 2016):

$$(1) \qquad d\,\sigma_{H,titrant} = \frac{(n_A - [H^+]V) - (n_B - [OH^-]V)}{m_s}$$

where n_A and n_B are moles of acid and base added, respectively, $[H^+]$ and $[OH^-]$ are measured concentrations of hydronium and hydroxyl ions, V is the total volume of solution, and m_s is the dry weight of the biomass. In converting from wet to dry biomass, a measured wet:dry cell weight ratio of 8:1 was used for the wild type *E. coli*, which is consistent with Borrok et al (2005)'s estimate. For the dLBTx8 cell titration curves, a measured wet:dry cell weight ratio of 14:1 was used.

2.2.3 Surface complexation modeling

Site concentrations and protonation equilibrium constants were fit using a PHREEQC-compatible optimization program, PhreePlot. The wild type strain *E. coli* was modeled using 1, 2, 3, and 4-site protonation models based on the following proton dissociation reactions:

(2) $R\text{-}COOH \leftrightarrow R\text{-}COO^- + H^+$

(3) $R\text{-}POH \leftrightarrow R\text{-}PO^- + H^+$

(4) $R\text{-}OH \leftrightarrow R\text{-}O^- + H^+$

(5) $R\text{-}NH_3^+ \leftrightarrow R\text{-}NH_2 + H^+$

where R- is the bacterium the respective functional groups are attached to. Reactions (2), (3), (4), and (5) represent carboxyl, phosphoryl, hydroxyl, and amine deprotonation, respectively. The least number of sites required to constrain the observed protonation behavior was used for the remainder of the modeling.

The many proton-dissociable ligands on the lanthanide binding tag can be attributed to the carboxyl groups present on the side chains of the LBT protein, such as on amino acids Asp1, Asp5, Glu9, and Glu12. Because we do not know the total amount of protonatable carboxyl groups, we allowed for this site density to be optimized based off the following reaction:

(6) $LBT\text{-}COOH \leftrightarrow LBT\text{-}COO^- + H^+$

where LBT- is the lanthanide binding tag peptide and -COOH indicates the side chain carboxyl groups present on the amino acids of the tag.

To account for the Tb-complexing and proton-sorbing ligands on the LBT peptide, we developed a simplified three-proton adsorption/desorption reaction that could achieve charge neutrality through sorption to three H^+ ions:

(7) $LBT\text{-}OH_3 \leftrightarrow LBT\text{-}O^{-3} + 3\ H^+$

Because Nitz et al (2004) show that a Tb^{3+}-LBT complex is charge neutral, despite simplifying multiple proton dissociation reactions into a simple three-proton sorption/desorption reaction (7), our expression allows us to adequately describe LBT charge neutrality by either sorption to one Tb^{3+} ion or three H^+ ions. Furthermore, all remaining proton dissociable sites on the LBT that are not involved in Tb complexation have been accounted for by reaction (6).

Associated mass action equations used to optimize fit to titration data are as follows:

(8) $K_1 = \frac{[R-COO^-]a_H{}^+}{[R-COOH]}$

(9) $K_2 = \frac{[R-PO^-]a_H{}^+}{[R-POH]}$

(10) $K_3 = \frac{[R-O^-]a_H{}^+}{[R-OH]}$

(11) $K_4 = \frac{[LBT-COO^-]a_H{}^+}{[LBT-COOH]}$

(12) $K_5 = \frac{[LBT-O^{-3}]a_H{}^{+3}}{[LBT-OH_3]}$

where K is the conditional stability constant for each given reaction and a_H^+ is the proton activity. A surface area of 140 m^2/dry grams (Fein et al. 1997), which assumes rod-shaped cells 5.0 μm long and 1.0 μm wide with 10^{10} cells/mL in a 2.5 g/L cell suspension, was used to convert model output site densities in sites/nm^2 to moles/dry gram for each individual titration curve and for subsequent surface complexation modeling.

2.2.4 Wild type E. coli (WT) surface complexation model

Our surface complexation models were implemented under a temperature of 24 °C, pH 6, and 10 mM NaCl ionic strength. We initially created a model for Tb sorption onto the wild type, un-induced *E. coli* bacterial surface. As the carboxylate group is the most readily deprotonated site type amongst carboxylate, phosphoryl hydroxyl, and amine functional groups at a pH of 6, we investigated Tb sorption using a three-site carboxyl, phosphoryl, and hydroxyl protonation model, with Tb sorption being accounted for only via carboxyl functional groups (herein after called a 1-site wild type carboxyl model). Protonation equilibrium constants and site concentrations for all three site types were accounted for based on modeling of the acid-base titration experiment.

The following reaction for wild type *E. coli* Tb sorption was used:

(13) $R\text{-}COO^- + Tb^{3+} \leftrightarrow R\text{-}COOTb^{2+}$

Wild type carboxyl sites were assumed to form monodentate surface complexes with Tb^{3+} cations (Texier et al. 2000). However, we note that it has been suggested that multidentate binding could be possible (Ozaki et al. 2006). The Tb-carboxyl stability constant was optimized and solved for by fitting to Tb adsorption capacity experimental data. More specifically, Tb adsorption capacity data were converted to surface excess (n) and equilibrium Tb concentration (c) values to compute distribution coefficient (K_d) values through the following expressions:

(14) $$n = \frac{\text{µmol of Tb sorbed}}{\text{dry grams of biomass}}$$

(15) $$c = \text{Tb added (µM)} - \text{Tb sorbed (µM)}$$

(16) $$K_d = \frac{n}{c}$$

We optimized Tb stability constants based on experimental n and K_d values, which would yield the best overall fit to both experimental sorption capacity and sorption affinity. While fitting to n can be useful to match experimental sorption capacity results, fitting to K_d can yield more accurate results at low surface loadings. Thus, when optimizing for Tb stability constants, we pooled n and K_d experimental values and optimized to both types of values. Uncertainties on fitted stability constants are estimated using bounds computed by optimizing carboxyl-Tb stability constants to experimental surface excess data $\pm$ 1 standard deviation. In propagating error associated with a fixed site concentration obtained from titration fitting, $\pm$ 1 standard deviation of the calculated carboxyl site concentration from the acid-base titration modeling was also applied while fitting to surface excess data. In this way, we establish the maximum range of values that can be obtained via optimization of the carboxyl-Tb stability constant accounting for $\pm$1 standard deviation of experimental surface excess and titration modeling error.

2.2.5 LBT E. coli surface complexation model

In addition to a wild type 1-site carboxyl model, we created an LBT + native carboxyl site model wherein LBT-carboxyl, native carboxyl, phosphoryl, and hydroxyl sites can adsorb/desorb protons, but only LBT sites and native carboxyl groups participate in metal complexation. Carboxyl-Tb biosorption was accounted for using reaction (12) and LBT-Tb biosorption was accounted for using the following simplified 1:1 monodentate reaction:

(17) $LBT\text{-}O^{3-} + Tb^{3+} \leftrightarrow LBT\text{-}OTb^{0}$

Although Tb^{3+}-LBT complexes are eight-point coordinated (Nitz et al. 2004) we consolidated the polydentate Tb binding into a single Tb binding constant, similar to how Nitz et al (2004) developed a Tb^{3+}-LBT binding constant based off a simplified 1:1 binding stoichiometry. Similar to the WT model, the model describing dLBTx8 induced *E. coli* cells uses a surface area of 140 m^2/gram dry cell weight. The number of $LBTOH_3$ sites were fixed at 5.93×10^{-5} $\frac{\text{moles}}{\text{dry gram}}$ based on estimates of the number of dLBTx8 peptides induced onto the outer membrane protein A (Supporting Information 2.1). The LBT-Tb stability constant was optimized based off both *n* and K_d experimental values. We then compared the obtained value with 7.24 based on Nitz et al. (2004) and the wild type *E. coli* - Tb binding constant we previously solved for using the wild type 1-site carboxyl modeling.

2.2.6 Treatment of electrostatic potential of bacterial surfaces

The presence of charged complexes and adsorbed ions on surfaces generates surface charge, which impacts the thermodynamic affinity of surface complexation reactions (Goldberg 1992). Previous studies have implemented a constant capacitance model (CCM) approach, allowing the capacitance parameter (C) to be optimized in order to create a better model fit with experimental sorption data (Fein et al. 1997) This approach is limited because it relates surface charge to surface potential using a C value that is unconstrained in optimization and relies on only the curve-fitting procedure without external physiological validation. Some studies approach electrostatics as playing a much smaller role in bacterial sorption behavior compared to other parameters such as site density, surface area, and functional group pK_a's (Borrok, Turner, and Fein 2005). Despite the limitation of a constant capacitance model, we adopt a CCM approach in this study to importantly account for the high valence of lanthanides when sorbed to the wild type bacterial surface sites. Not accounting for electrostatics using any charge model (non-electrostatic model) would pose an even more troubling assumption that charge build-up from lanthanide biosorption is negligible. In this study the capacitance value in the CCM was fixed to 8.0 $\frac{F}{m^2}$ based on optimization calculations conducted by Fein et al (1997). Furthermore, Ngwenya et al (2009, 2010) use this 8.0 $\frac{F}{m^2}$ capacitance value in calculating REE-bacteria stability constants. By using the same capacitance parameter, we maintain consistency with past sorption studies, allowing us to compare our calculated Tb-carboxyl binding constant with values calculated by others.

2.3 Results and Discussion

2.3.1 Acid-base properties of wild type and engineered cell surfaces.

Wild type *E. coli* acid-base titration data were fit using models containing a range of one to four site types (Figure 2.1). One and two site types did not adequately capture the protonation

behavior of the cells, while three and four site types fit to experimental data equally well. To minimize the number of unconstrained pK_a and site concentration values, a three-site model was used for the wild type strain in a similar fashion as Ngwenya et al (2009, 2010), accounting for the protonation reactions given in Eqs. (2)-(4). Fourth and fifth reactions given in Eq. (6) and (7) are incorporated to model the protonation behavior of the dLBTx8 induced *E. coli* strain. Fitted site concentrations and pK_a values obtained from modeling fits to titration data for the 3-protonation site carboxyl WT model and the 5-protonation site LBT + native carboxyl model are given in Table 1.1 and Figure 2.2. Standard deviations are calculated based on modeling results obtained from titration experiments for a given strain run in triplicate. The total site concentrations we computed fall within an appropriate range of total moles of sites/dry gram compared to values found in the literature (Table 2.1). The total sites on the WT cells are notably similar to Martinez et al (2014)'s multisite Langmuir model that uses a linear programming regression method (LPM) to solve for site densities based on REE sorption data.

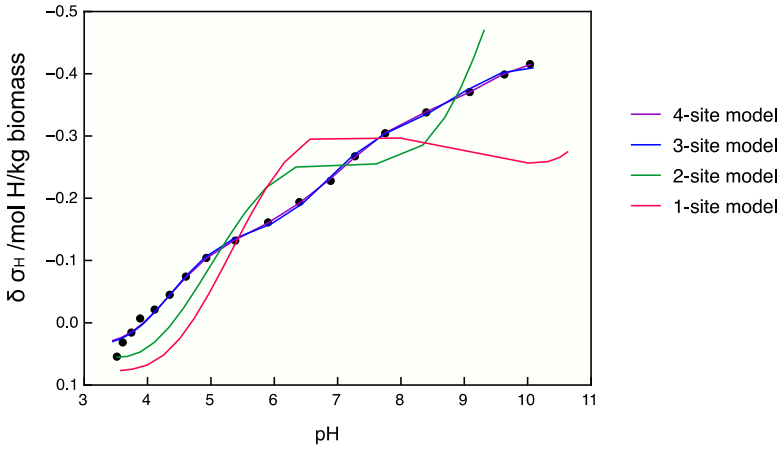

Figure 2.1 Wild type *E. coli* CCM acid/base titration data (black symbols) and model fits for a typical titration experiment. Models with varying amounts of proton-dissociable site types are shown as curves.

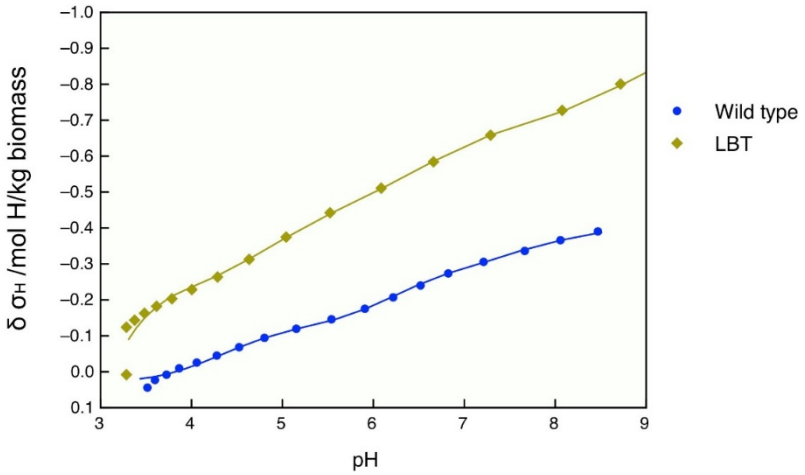

Figure 2.2 Averaged experimental data of acid/base titrations run in triplicate (filled symbols) with corresponding 3-protonation site wild type and 4-protonation site LBT *E. coli* CCMs (curves). Site concentrations and pK_as for the modeling fits to titrations are given in Table 2.1. The 3-protonation site wild type CCM contains carboxyl, phosphoryl, and hydroxyl site types while the

5-protonation site LBT CCM contains the same site types but also includes a lanthanide binding tag – carboxyl site type and an $LBTO^{-3}$ site type.

Table 2.1 Total site concentrations and pK_as of various models describing bacterial surface protonation of wild type and LBT-displayed *E. coli*. Sites 1, 2, 3 and 4 are attributed to the proton-dissociable carboxyl, phosphoryl, hydroxyl and LBT binding sites corresponding to protonation reactions given in Eqs. (2), (3), (4), and (5), respectively.

Model Type	Site concentrations (mol sites/dry gram × 10^{-4})					pK_a			
	Site 1	Site 2	Site 3	Site 4[a]	Total	Site 1	Site 2	Site 3	Site 4
Multisite Langmuir									
Martinez et al (2014)	n/a	n/a	n/a	n/a	5.49	n/a	n/a	n/a	n/a
4-protonation site non-electrostatic	8.80±	7.28±	4.24±	5.28±					
Borrok et al (2005)	0.56	3.04	1.68	2.4	25.6	3.1	4.7	6.6	9.0
5-protonation site CCM (LBT)	1.97±	1.78±	1.96	0.80±	7.10±	4.98±	6.82±	9.15±	4.86±
[this work]	0.0.56	0.49	±0.79	0.59*	1.23	0.13	0.29	0.70	0.20
3-protonation site CCM (wild type)	1.53±	1.37±	0.75±		3.65 ±	4.23±	6.68±	9.01±	
[this work]	0.07	0.52	0.14	n/a	0.54	0.05	0.10	0.28	--
3-protonation site CCM Ngwenya et al (2003)	5.0±0.7	2.2±0.6	5.5±2.2	n/a	12.7	4.3± 0.2	6.9± 0.5	8.9± 0.5	--
3-protonation site CCM						4.82±	6.9±	9.4±	
Fein et al (1997)	1.20	4.40	5.20	n/a	10.8	0.14	0.5	0.6	--

[a]Site 4 for a 4-site non-electrostatic model (Borrok et al, 2005) refers to a naturally-occurring fourth site type, while for our 5-site CCM (LBT), it refers to the engineered LBT site's carboxyl moieties present on amino acid side chains. The 5-site CCM (LBT)'s 5th site type is a LBT site type (reaction 6) with a fixed site density of 0.59 mol/dry g and an optimized pK_a of 9.96±0.10.

Phosphoryl (Site 2) and hydroxyl (Site 3) pK_a values are within error between the two strains, while carboxyl group pK_as between strains are both reasonable values for the carboxyl moiety (Hong and Brown 2006). This suggests that the induction of LBTs does not significantly alter the inflection points in the acid-base titration of the *E. coli* surface. A two-sample t-test assuming unequal variances was performed for carboxyl, phosphoryl and hydroxyl site concentrations, with a null hypothesis that for each site type, the mean site concentration difference between WT and LBT strains was 0. Using $p < 0.05$, the resultant t stat values for carboxyl, phosphoryl, and hydroxyl site types were -1.33, -1.00, and 2.63, respectively. As the two-tailed t critical values for carboxyl, phosphoryl, and hydroxyl site types were 4.30, 2.78, and 4.30, respectively, we cannot reject the null hypothesis for any of the sites. Mean carboxyl, phosphoryl, and hydroxyl site concentrations are statistically indistinguishable between WT and LBT strains Figure 2.3 illustrates the differences in fitted pK_a and site concentration values between the wild type and engineered bacterial strains, with error bars indicating $\pm$ 1 standard deviation.

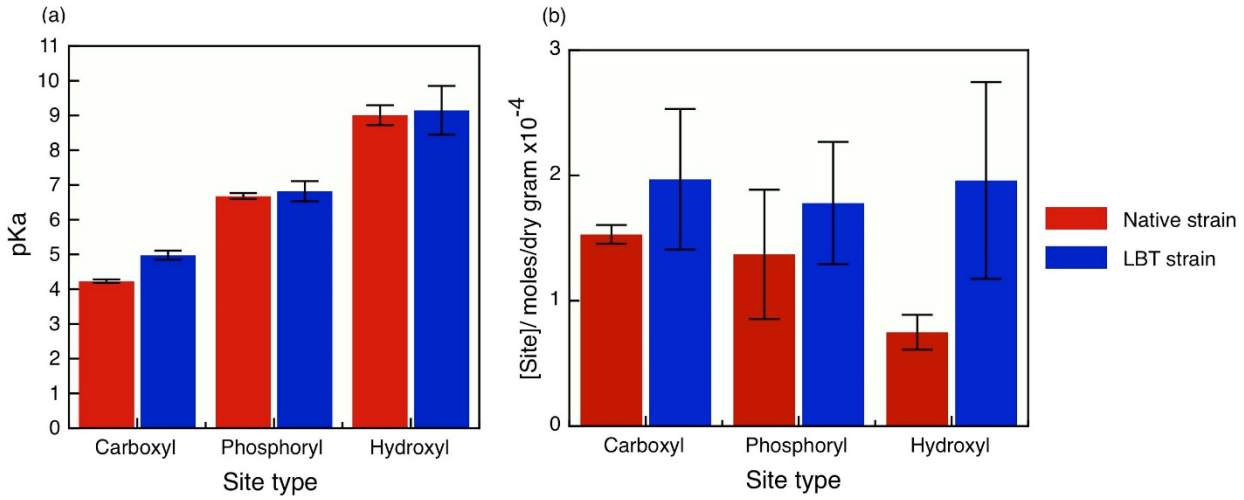

Figure 2.3 Fitted pK_a and site concentration values for wild type and LBT strains of *E. coli* based on surface complexation modeling of acid/base titration data. Error bars indicate ±1 standard deviation as calculated by triplicate experiments.

2.3.2 One-site native carboxyl model describing Tb sorption onto wild type cells

Markai et al (2003) and Ngwenya et al (2010) use a one-site CCM to study lanthanide sorption onto the gram-positive bacteria, *Bacillus subtilis,* and the gram-negative bacteria, *Pantoea agglomerans*, respectively, as it has been postulated that the carboxyl functional group dominates sorption in the pH range of 5-6 (Takahashi et al. 2010a). Although it is clear from our titration data that multiple types of proton-dissociable surface functional groups are present on the wild type cell surfaces, it is not clear whether all site types contribute substantively to REE adsorption. To determine whether a single metal exchangeable site is sufficient to capture REE adsorption data, we applied a 1-REE site carboxyl CCM (WT model in Figure 2.4) with a fixed pK_a of 4.23 and site concentration of $1.53 \pm 0.07 \times 10^{-4}$ $\frac{\text{moles}}{\text{dry gram}}$ to fit our Tb adsorption isotherm data. This 1-REE site carboxyl CCM incorporates the Tb-carboxyl surface complexation reaction given in Eq. (13) in addition to the protonation reactions given in Eqs. (2)-(4). Optimization of the wild type 1-REE site carboxyl model to fit experimental distribution coefficient, K_d, values and surface

excess, *n*, values resulted in a carboxyl-Tb stability constant of 5.12 [5.00, 5.25] (with a lower bound of 5.00 and an upper bound of 5.25). Optimization to a pooled dataset of *n* and K_d values results in a good holistic fit to sorption capacity (*n* vs *c*) and sorption affinity (K_d vs *n*) plots (Figure 2.4a,b). A one-REE site carboxyl model was sufficient in capturing the total Tb sorption capacity of the wild type *E. coli* surface.

Table 2.2 1-REE site carboxyl wild type and 2-REE site LBT plus carboxyl CCM parameters used in addition to the protonation parameters in Table 1 to model Tb binding data.

Model Type	Site Type	Site-Tb $\log_{10}K$	Site concentration (moles/dry gram x 10^{-4})
Wild type model			
	Carboxyl	5.12* [5.00, 5.25]	1.53±0.07
LBT model			
	Carboxyl	5.12*	1.97±0.56
	LBT	7.51 [7.01, 8.56]	0.59

*Carboxyl-Tb stability constant fixed from the carboxyl-Tb $\log_{10}K$ constant obtained from the wild type model

‡Fixed binding constant value obtained from Nitz et al (2004)

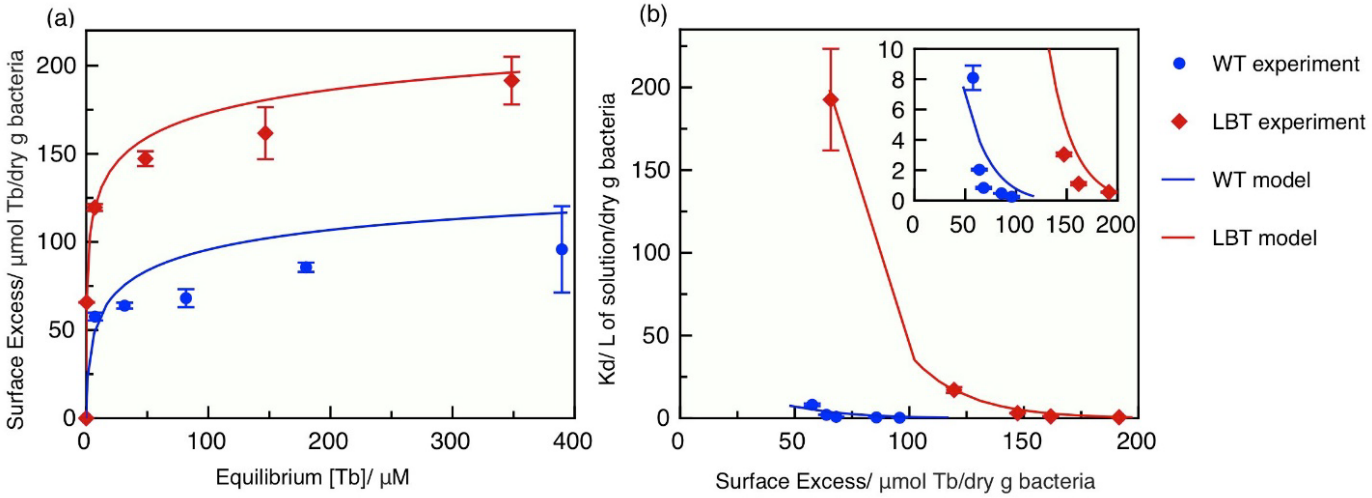

Figure 2.4 (a) Sorption isotherm and (b) distribution coefficient modeling fit at a pH of 6. Wild type (WT) model refers to a 1-site carboxyl model describing the sorption of Tb to the wild type strain. The WT model shown here was fit to a pooled surface excess and distribution coefficient dataset. The LBT model refers to a native carboxyl and lanthanide binding tag model describing the sorption of Tb to the LBT strain. Experimental data have been previously published in Park et al (2017).

Our Tb-carboxyl stability constant estimate of 5.12 [5.00, 5.25] is two orders of magnitude higher than *Enterobacteriaceae* Zn-carboxyl binding ($\log_{10}K$ = 3.3±0.1) and one order of magnitude higher than Pb-carboxyl binding ($\log_{10}K$ = 3.9±0.8) (Ngwenya, Sutherland, and Kennedy 2003). This suggests that the wild type carboxyl group may be more selective for Tb compared to some heavy metals. In order to recover REEs from environmental fluids containing a mixture of competing metals such as Pb, we require a higher-affinity site type to increase the selectivity of the surface for REEs. Our calculated average $\log_{10}K$ of 5.12 for Tb binding is comparable to Ngwenya et al (2010)'s reported Tb stability constant of 5.37 and Martinez et al (2014)'s value of 4.95A one-site carboxyl CCM is sufficient to model Tb sorption onto the wild type *E. coli* cell surface at pH 6 and for Tb aqueous concentrations up to 1.30 mmol/dry g bacteria in this study.

2.3.3 LBT and native carboxyl site model describing Tb sorption onto LBT cells

To model adsorption data for the dLBTx8 induced strain of *E. coli*, we implement a bottom-up approach and superimpose Tb binding by LBTs while assuming the interaction between a carboxyl group and a Tb ion to be the same for the wild type and engineered strains. Surface protonation reactions given in Eqs. (2)-(4), (6), and (7) and Tb-complexation reactions given in Eqs. (13) and (17) are all included in the SCM. We fix the carboxyl-Tb stability constant at our previously calculated value of 5.12 [5.00, 5.25] from the wild type 1-REE site model and optimize for the LBT-Tb binding constant. We obtain a value of 7.51 [7.01, 8.56] – we attribute the large upper and lower bound range to the propagation of error carried over from carboxyl-Tb stability constant and carboxyl site concentration uncertainties. Our average LBT-Tb binding constant of 7.51 is markedly similar to 7.24 reported by Nitz et al (2004). The average LBT-Tb stability constant of 7.51 is two orders of magnitude higher than the average carboxyl-Tb binding constant of 5.12, highlighting the substantially higher affinity of LBT sites for REEs compared to wild type carboxyl sites.

A major advantage of implementing a quasi-mechanistic modeling approach compared to pure empirical adsorption modeling is our ability to distinguish chemical features of the surface and conditions of the aqueous solution that favor REE recovery. Our SCM results can be used to infer dominant surface Tb speciation as a function of aqueous concentration (Figure 2.5). Overall, LBT sites dominate Tb surface complexes at low aqueous concentrations, while native cell surface functional groups become dominant at higher loadings, once LBT sites become saturated. At aqueous Tb concentrations exceeding 20 μmol/dry gram bacteria, carboxyl sites play an equal or greater role in sorption of Tb than the more REE selective LBTs. Thus, both pH and equilibrium REE concentration influence surface speciation. Such insights will be useful in interpreting the results of spectroscopic techniques such as EXAFS and TRLFS, which have yielded varying conclusions as to whether carboxyl or/and phosphoryl functional groups act as the dominant sorption site of REEs. Texier et al. (2000) conducted TRLFS on *P. aueruginosa* exposed to high concentrations of Eu (8 mM) at pH 5 and concluded that binding occurs on both carboxyl and phosphoryl groups. At lower Eu concentrations (up to 500 μM) at the same pH, Markai et al. (2003) report that binding by carboxylate alone is sufficient to describe Eu sorption on *B. subtilis*. Thus, we hypothesize that at pH ~5-6, carboxyl groups are the dominant sorption site at low to intermediate aqueous REE concentrations, while at higher concentrations (>~1mM), both carboxyl and phosphoryl groups contribute significantly to REE complexation.

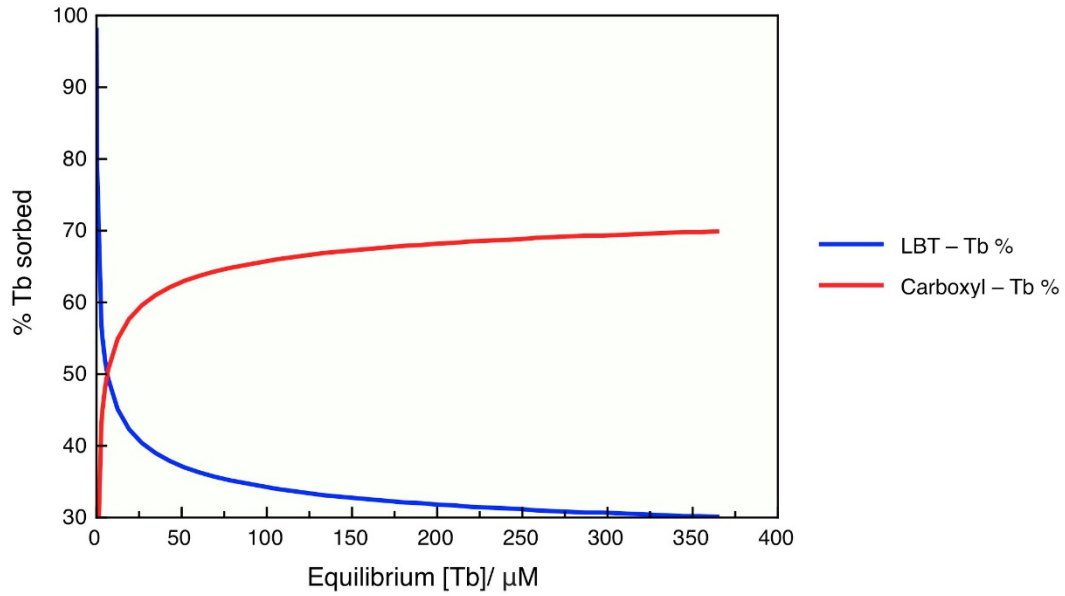

Figure 2.5 Percent Tb sorbed to LBT and carboxyl sites calculated from LBT model at a pH of 6 as a function of equilibrium Tb concentration, using a cell suspension density of 0.36 dry g bacteria/L. At low loadings of < 20 µM, lanthanide binding tag sites dominate Tb sorption, while at higher loadings > 20 µM, carboxyl groups play a large role in Tb sorption due to the saturation of LBT sites.

2.3.4 Optimal Tb recovery as a function of pH and equilibrium aqueous concentration

From an REE recovery and product purity standpoint, it is advantageous to design conditions of the bioreactor or flow system that maximize the fraction of REEs sorbed (and specific REE type) to LBTs compared to other surface site types, while minimizing sorption of non-REE metals. Conditions that optimize for separation may compromise overall recovery, so striking the right balance requires a quantitative exploration of parameter space that is not realistic to access using experiments alone. Figure 2.6 gives a plot of % Tb recovered as a function of equilibrium aqueous concentration and pH. Based on our results in simple buffered solutions at a 10 mM ionic strength and 24 °C temperature, low equilibrium Tb concentrations likely provide for optimal REE recovery at the studied pH range of 3 to 8. Due to the high pK_a of 9.96 of lanthanide binding tag sites, changes in pH from 3 to 8 have a minimal effect on LBT-Tb sorption behavior under low equilibrium Tb concentrations. However, at higher loadings of ~690 µmol/dry g bacteria, when LBT sites are saturated and carboxyl groups are the dominant sorbing site type, a pH of 6 provides optimal % Tb recovery. Thus, we demonstrate how both pH and equilibrium Tb aqueous concentrations are important factors in understanding what parameter space achieves most efficient recovery of rare earths. Our future work focuses on extending this SCM to account for other ionic species that compete with the REEs for surface sites, as well as to predict selectivity among the REEs, both in batch adsorption mode and under flow. As temperature can dramatically affect the thermodynamics of aqueous and surface reactions, future work should also investigate sorption behavior of engineered cells at elevated temperatures consistent with environmental

samples from geothermal brines. Sorption isotherms with changing temperature would allow for the development of temperature-dependent surface site-REE stability constants.

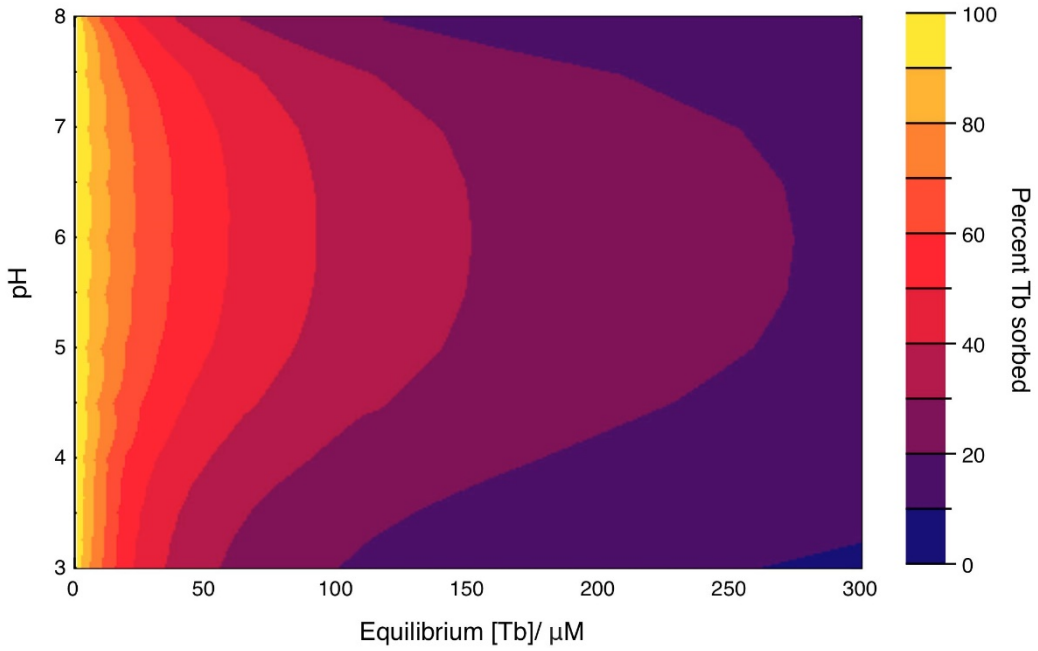

Figure 2.6 Percent Tb sorbed to LBT-engineered bacterial surface (adsorption to both carboxyl and lanthanide binding tag sites) calculated from LBT model as a function of pH and aqueous Tb concentration, using a cell suspension density of 0.36 dry g bacteria/L. Optimal sorption for low metal loadings occurs at all pH (3 – 8), while optimal sorption for higher metal loadings (~250 µM) occurs at a pH of ~6.

2.4 Conclusions

We report that the incorporation of LBTs into the *E. coli* outer membrane poses two major benefits: (1) sorption onto lanthanide binding tags increases REE selectivity and affinity of the cell surface, which is relevant at low metal loadings, and (2) the presence of these tags increases the total concentration of available sorbing sites, thus also increasing overall sorption capacity. Tb binding is controlled by the presence of high-affinity, but low capacity, lanthanide binding tags as well as lower-affinity, but more abundant, wild type functional groups that increase overall sorption capacity at higher aqueous REE concentrations.

In this study, we observe the wild type *E. coli* surface complexation of Tb at a pH of 6 to be well modeled with a monodentate carboxylate binding mechanism. We propose a new surface complexation model for studying lanthanide binding tag sorption of Tb to *E. coli* through a constant capacitance model electrostatic treatment and monodentate binding mode simplification of LBTs. We observe that cells with lanthanide binding tags possess both high-affinity LBT sites and lower-affinity wild type functional groups. Protonation behavior and site concentrations of sorbing carboxyl functional groups were indistinguishable between WT and LBT strains. We thus attribute an increase in Tb sorption affinity and capacity to the presence of lanthanide binding tags on the cell surface. Future work will focus on studying the competition for engineered and wild type surface sites in the presence of other naturally occurring metals, such as Cu, Mg, and Pb,

found in geothermal brines and mining leachates. Further work should also be conducted on desorption studies in order to optimize removal of rare earths from bacterial surfaces once biosorption has occurred (Bonificio and Clarke 2016).

CHAPTER 3

Developing a predictive reactive transport model of bead encapsulated engineered *Escherichia coli* for the selective extraction of co-existing lanthanides

3.1 Introduction

Rare earth elements are critical for the advancement of a variety of different technologies, ranging from flat panel displays and fluorescent lamps (Humphries 2013) to high-performance magnets for electricity generation and industrial catalysts (Du and Graedel 2011). REEs derived from natural resources require post-processing for separation of co-occurring lanthanides because each lanthanide has distinct applications and commercial value. Lanthanum, for example, is a light rare earth element used mainly in catalysis that cannot be used in the permanent magnets required for wind turbines and magnetic resonance imaging (Du and Graedel 2011). Europium, in comparison, is valued in the commercial industry for its ability produce red color in LED displays due to its unique luminescent behavior (Rabie et al. 2007). Biosorption technologies using bacterial surfaces have been developed to selectively extract REEs from low-grade feedstocks such as mining leachates, acid mine drainage, coal fly-ash, and geothermal fluids (Wood 2001; D. M. Park et al. 2017). While microbes can be a cost-effective and regenerative biosorbent with a relatively high natural capacity for REE adsorption (Texier et al. 2000; Takahashi et al. 2005; Ngwenya et al. 2010; Dodson et al. 2015), they often possess similar relative affinities for all the lanthanides (Takahashi et al. 2005; 2010a; Bonificio and Clarke 2016), making it difficult to separate specific elements from REE mixtures.

In an effort to increase selectivity for rare earths, scientists have recently engineered the cell surface to selectively extract REEs in the presence of competing metals commonly found in mine tailings (Moriwaki et al. 2016; D. M. Park et al. 2016). One such method involves inducing the expression of lanthanide binding tags (LBT) on the cell surface of gram-negative bacteria (D. M. Park et al. 2016; 2017; A. Brewer et al. 2019). The LBT protein forms an eight-fold coordination complex with trivalent rare earth elements that excludes water molecules and is highly REE-selective. Lanthanide affinity in LBT complexes is governed by the ionic radius (Nitz et al. 2004) – the most common separation principal among REEs – with Tb^{3+} being the most strongly binding and La^{3+} being the least strongly binding. Thus, LBT-engineered *E. coli* cell surfaces possess unique binding free energies for each lanthanide, and we exploit this property to effectively separate specific rare earth elements using a fixed-bed column approach.

Here we report laboratory demonstration and validation of a scalable REE extraction and separation process on fixed-bed columns using dLBTx8-induced microbial biomass embedded in porous, non-adsorbing polyethylene glycol diacrylate (PEGDA) hydrogel beads (Figure 3.1). Immobilizing bacteria in a porous polymer matrix not only eliminates the necessity for the energy intensive procedures common to batch scale operations, such as centrifugation and filtration, but the carrier material also provides increased mechanical strength and a means to immobilize a high density of cells without inhibiting adsorption capability (Dodson et al. 2015). Breakthrough curves are generated under a continuous flow column setup to mimic a packed-bed bioreactor that can be scaled up in future for industrial processes. Optimal separations can only be achieved under specific conditions that are not easily identified by direct experimentation. Instead, we investigate the underlying chemical and physical phenomena that enable the cell surface to preferentially bind middle and heavy rare earth elements compared to lighter lanthanides. A quasi-mechanistic, one-dimensional reactive transport model is developed and implemented to characterize experimental

batch adsorption and breakthrough curve data. We then apply this model to identify the chemical and operational parameters that maximize the recovery of europium from a mixed-REE solution.

Figure 3.1 Experimental setup for dual porosity transport of rare earth elements through a fixed-bed column packed with encapsulated dLBTx8 *E. coli* cells.

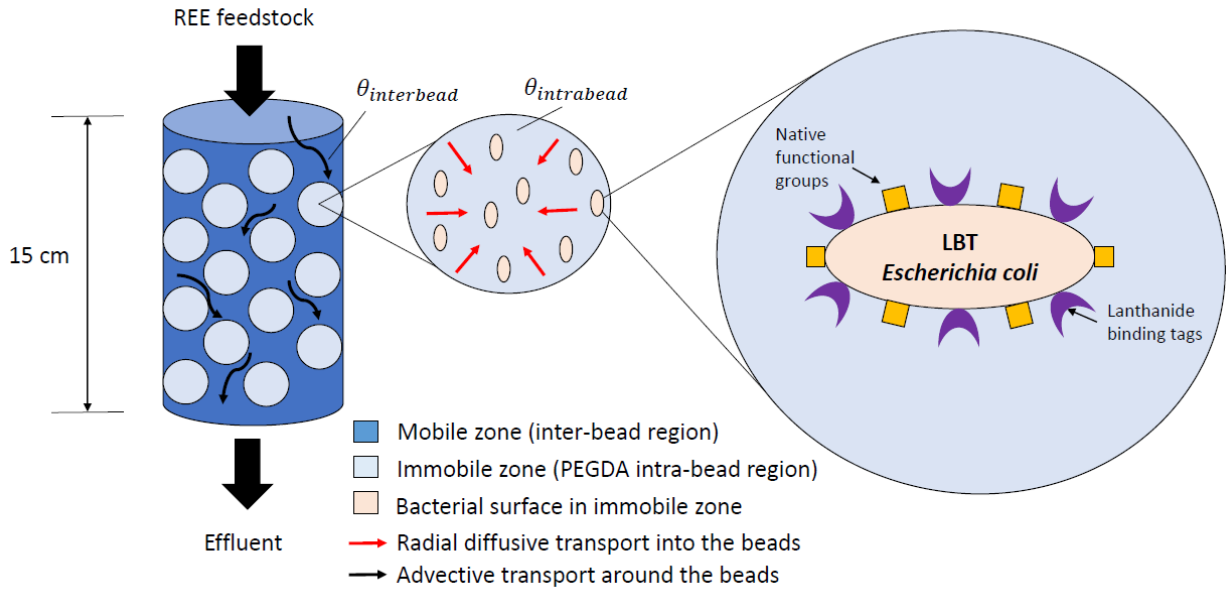

3.2 Methods

3.2.1 Bacterial strain and growth conditions

E. coli cells engineered with lanthanide binding tags (LBT) were grown in LB media and expression of LBT was induced at mid-exponential phase at 37°C. The full procedure for plasmid construction and LBT expression can be found in Park et al. (2016, 2017). We washed the induced cells once in 10 mM MES (2-(N-morpholino)-ethanesulfonic acid) at pH 6, and normalized by OD_{600} prior to microbe bead preparations.

3.2.2 Microbe bead synthesis

Polymer beads with a high density immobilized cells were synthesized using a bulk emulsion method as described by Brewer et al. (2019a). Briefly, concentrated cell suspensions were mixed with a polymer precursor mixture and agitated for 15 seconds prior to UV light exposure for 120 seconds. The resultant polymerized droplets of PEGDA and engineered *E. coli* were size selected by filtration and washed in MES buffer before being used in the columns. Dry and wet weights of beads were also measured as described by Brewer et al. (2019a). 76 ± 2.1 wt% of the beads consisted of water while the remaining amount was made up of cells and PEGDA polymer. Based on the known cell and PEGDA masses added during bead synthesis, we estimate that the dry beads were ~13 wt% microbial biomass and ~87 wt% PEGDA.

3.2.3 Batch adsorption of mixed lanthanides

A batch adsorption capacity experiment was conducted by introducing a mixture of 15 rare earth elements (14 lanthanides and yttrium) to the engineered microbe beads. 5 µM of each REE-chloride was added to a solution containing a cell suspension density of 0.36 dry g/L. The cell suspension density was calculated as 13 wt% of the total hydrogel beads used. A previous study by Brewer et al., (2019) demonstrated the non-sorbing characteristic of the encapsulating PEGDA polymer. Furthermore, the encapsulation process does not hinder the bacteria's ability to adsorb or desorb REEs. Based on these results, we assume that the 13 wt% bacterial mass present in the hydrogel beads are readily adsorbing and hold the same thermodynamic biosorption properties as using pure, un-encapsulated wet cell suspensions. We buffered the pH at 6 using a solution of 10 mM MES. The mixed REE-microbe solution was centrifuged at 20,000*g* for 8 minutes. The extracted supernatant was analyzed using an inductively coupled plasma mass spectrometer (ICP-MS) to measure the amount of each rare earth remaining in solution, and a mass balance calculation provided the microbe bead's adsorption capacity for each rare earth. To check adsorption dynamics with varying metal loadings, we conducted similar batch adsorption experiments on an example rare earth, Nd, at pH 6 (Supporting Information 3.1, 3.2, 3.3, Figure SI-1). This REE was chosen as the one metal to further study because it occurs solely in the +3 oxidation state and is important industrially for production of permanent magnets. We define surface excess, n, to describe adsorption capacity of the cell surface as a function of Nd loading:

$$(1)\ n = \frac{moles\ of\ Nd\ adsorbed\ to\ bacterial\ surface}{dry\ grams\ of\ bacteria}$$

3.2.4 Breakthrough curve experiments

We packed our microbe beads in Econo-Column glass chromatography columns (Biorad) for continuous flow experiments. First, columns of dimensions 15 x 0.5 cm, 20 x 0.5 cm, or 100 x 1 cm were gravimetrically loaded with bead suspensions and then were packed down by applying minimal fluid pressure to the top of the column with a hand-pumped syringe. Extra volume created under this pressure was re-packed with more microbe beads until the entire column was completely filled. We conditioned the breakthrough columns with 10 mM, pH 6 MES buffer >5 times the bed volume prior to flow-through of rare earths. All breakthrough curve experiments were conducted at 1±0.1 mL/min flow rate, with flow rates being checked periodically by weighing effluent volumes over a known period of time. REE feedstocks pumped through the column consisted of varying concentrations of Nd (50, 500, 1500 µM) at a 10 mM ionic strength and buffered pH 6. Further details on the breakthrough curve experiments are detailed in Brewer et al. (2019).

3.2.5 ICP-MS analysis of lanthanide breakthrough curve

When measuring breakthrough curve effluents for experiments containing 14 lanthanides and yttrium, a Thermo XSeriesII ICP-MS instrument was run in standard mode at UC Santa Cruz (Bank, T.; Roth, E.; Tinker, P.; Granite 2016). The sample introduction system was an ESI PFA-ST nebulizer pumped at 120 µL/min. We used an internal rhodium standard to correct all samples for instrumental variability.

3.2.6 Surface complexation modeling of lanthanide adsorption

In order to predict rare earth adsorption behavior, we developed a surface complexation model that captures the underlying thermodynamics of lanthanide adsorption to the bacterial cell

surface. Acid-base titrations of dLBTx8 induced *E. coli* cells reported in Ch. 2 (Chang et al. 2020a) give constraints on proton association behavior and site concentrations for the following reactions:

(2) $>R - COOH \leftrightarrow >R - COO^- + H^+$

(3) $>R - POOH \leftrightarrow >R - POO^- + H^+$

(4) $>R - OH \leftrightarrow >R - O^- + H^+$

(5) $>LBT - COOH \leftrightarrow >LBT - COO^- + H^+$

(6) $>LBT - OH_3 \leftrightarrow >LBT - O^{-3} + 3\ H^+$

where >R- refers to the cell membrane and -COOH, -POOH, and -OH are carboxyl, phosphoryl, and hydroxyl functional groups, respectively. As described by Chang et al. (2020a), the induction of lanthanide binding tag peptides creates two types of protonatable site types: (1) additional potential carboxyl groups (>LBT-COOH) found on the amino acids of the peptide chain, and (2) the net -3 charged set of LBT ligands that chelates with REEs (>LBT-OH_3). Proton binding constants for the following five types of functional groups can be expressed as:

(7) $K_1 = \frac{(>R - COO^-)\,(H^+)}{(>R - COOH)}$

(8) $K_2 = \frac{(>R - POO^-)\,(H^+)}{(>R - POOH)}$

(9) $K_3 = \frac{(>R - O^-)\,(H^+)}{(>R - OH)}$

(10) $K_4 = \frac{(>LBT - COO^-)\,(H^+)}{(>LBT - COOH)}$

(11) $K_5 = \frac{(>LBT - O^{-3})\,(H^+)^3}{(>LBT - OH_3)}$

As previous studies have demonstrated through EXAFS (Takahashi et al. 2010a) and time-resolved fluorescence spectroscopy (Texier et al. 2000), binding of rare earth elements to bacterial cell surfaces at pH 6 is typically dominated by carboxyl functional groups. Proton adsorption was captured via the proton binding constants from the previous chapter (Chang et al. 2020a), and a linear free energy relationship (Ngwenya et al. 2010) between rare earth-acetates and rare earth-cell surface carboxyl groups was used to estimate carboxyl-REE binding for the following reaction:

(12) $>R - COO^- + REE^{+3} \leftrightarrow >R - COOREE^{+2}$

where $>R - COOREE^{2+}$ is a +2 charged surface complex between an anionic native carboxyl group and a trivalent rare earth. We implemented a site concentration for the binding carboxyl group of $1.97 \pm 0.56 \times 10^{-4}$ mol/dry g based on prior work, and we invoke an allosteric inhibition mechanism to explain why >R – COOH sites but not >LBT – COOH sites participate in REE complexation (Chang et al. 2020a). More specifically, naturally occurring carboxyl groups can complex with REEs while carboxyl groups present on LBT peptides do not have the steric orientation to allow for large, trivalent REEs to electrostatically bind to the moiety present on the long peptide.

The chelation of the rare earth elements to the engineered lanthanide binding tag (LBT) protein was modeled using another surface complexation reaction:

(13) $>\text{LBT-O}^{-3} + \text{REE}^{+3} \leftrightarrow >\text{LBT-OREE}^{0}$

We used rare earth-native carboxyl binding constants from Fein et al. (2001) and Ngwenya et al. (2010)'s linear free energy relationships (LFER) to first estimate all the carboxyl-based affinity constants and also obtained rare earth-LBT stability constants from Nitz et al. (2004) (See Table 3.1). These studies did not directly report a stability constant for Y-carboxyl binding, so this value was approximated. Because Y and Ho have similar ionic radii of 1.019 and 1.015 Angstroms, respectively, and because carboxyl groups are a non-selective site type that binds all metals, we incorporated a Y-carboxyl constant equal to Ho-carboxyl binding. Similarly, lanthanide binding tag complexation to the elements Y, Pr, Sm, Ho, and Tm were not mentioned by Nitz et al. (2004), so we estimated their binding constants based on the reported relationship between LBT-REE binding affinity and the effective ionic radii of the rare earths discussed in Nitz et al. (2004). Notably, this approach avoids tuning stability constants to match our measured breakthrough data and instead relies on systematic relationships in chemical affinity reported in prior works (Fein, Martin, and Wightman 2001; Ngwenya et al. 2010; Nitz et al. 2004).

3.2.7 One-dimensional reactive transport modeling

We integrated this surface complexation model into a dual porosity reactive transport model in the code PhreePlot (Kinniburgh & Cooper, 2019). The advection-reaction-dispersion (ARD) equation, based on conservation of mass for a chemical being transported, can be used to describe one-dimensional flow. The ARD equation is as follows:

$$(14)\ \frac{\partial C}{\partial t} = -v\frac{\partial C}{\partial x} + D_L\frac{\partial^2 C}{\partial x^2} - \frac{\partial q}{\partial t}$$

where C is concentration in water (mol/L), t is time (seconds), v is pore water flow velocity (m/s), D_L is the hydrodynamic dispersion coefficient (m^2/s), and q is concentration in the solid phase. D_L can be expressed as $D_L = D_e + v^*\alpha$, where D_e is the effective diffusion coefficient and α is the dispersivity (m). $-v\frac{\partial C}{\partial x}$ refers to advective transport, $D_L\frac{\partial^2 C}{\partial x^2}$ refers to dispersive transport, and $\frac{\partial q}{\partial t}$ is the change in concentration due to the chemical reactions defined by our constant capacitance surface complexation model as developed by Chang et al. (2020).

The packed, fixed-bed columns were modeled as sub-divided vertical cells. The first and last cells of the column were subject to the type three Cauchy boundary condition (e.g. a mixed Dirichlet and Neumann boundary condition) as follows:

$$(15)\ C\ (x_{end}\ ,\ t) = C_o + \frac{D_L}{v}\frac{\partial C(x_{end},t)}{\partial x}\ ;\ t \geq 0$$

where the concentration at the ends of the columns, x_{end}, is known to be a combination of the inlet concentration, C_o, and a dispersive term. Many authors have used both the Dirichlet boundary condition (Rao et al. 1980; Van Beinum et al. 2000; Roden and Scheibe 2005; Rotter et al. 2008; H. J. Park and Tavlarides 2010) and the Cauchy boundary condition (Walter et al. 1994; Coelho, Faria, and Marques 2017) to model breakthrough of a constant solution influx – which condition to implement to solve the transport problem is determined by the system and what information is known about the system. In our case, we used the Cauchy boundary condition at both the inlet and

outlet cells, because both the concentration value and the derivative of the concentration over time at the specified boundaries are known.

The PEGDA polymer that immobilized the bacterial cells is porous and the packing of the beads into a fixed-bed column creates its own distinct pore structure, so we implemented a dual porosity model to account for the exchange in fluid associated with interbead (between beads) and intrabead (within beads) porosity. The intrabead region was associated with only diffusive transport as pore size limits advection within the bead. The interbead region, however, experiences significant diffusive and advective transport. Modeled columns were discretized along the direction of flow into 100 cell units of equal volume. The model flow rate was set to match the experimental value of 1.0 mL/min. Each cell contained one interbead region with 0.28 porosity (fraction of total column volume) and one intrabead region with 0.54 porosity (fraction of total column volume). Porosities were determined geometrically by estimating the number of beads in a column given a fixed and uniform volume for each bead (assumed no deformation during compaction and packing). During each time step, exchange between these two regions was defined by a first-order equivalent exchange approximation according to the following expression (Van genuchten, M. Th., Dalton 1986):

$$(16)\ \frac{dM_{intrabead}}{dt} = \alpha(C_{interbead} - C_{intrabead})$$

where $M_{intrabead}$ is the moles of chemical within the bead and α is a time factor (s^{-1}) that determines the rate of exchange of chemical between the intra- and interbead regions. The exchange factor α is related to specific geometries and diffusion properties of the intrabead region; for a spherical region, the relationship is defined as:

$$(17)\ \alpha = \frac{D_{IPD}\,\theta_{intrabead}}{(a\,f_{s\to 1})^2}$$

where D_{IPD} is the intraparticle diffusion coefficient (m^2/s), $\theta_{intrabead}$ is the intrabead porosity (defined previously as 0.54), a is the radius of the sphere (m), and $f_{s\to 1}$ is a shape factor for sphere-to-first-order-model conversion (0.21 for a sphere).

A calibration breakthrough curve of 500 µM Nd continuously flowing through a packed 20 cm column was used to optimize for dispersivity and intraparticle diffusion coefficient (Figure 3.3, Supporting Information 3.4). Because these values are inherent physical properties of the column flow dynamics, we fixed the obtained values as constants in later transport models. For model runs involving transport of multiple rare earth elements, multicomponent diffusion was enabled such that individual diffusion coefficients for each element were defined using values reported in Martelli et al. (2013) (Table 3.1). Because a diffusion coefficient was not reported for Y, we used the diffusion coefficient of Ho for Y as the two elements are similar in ionic radius.

The total REE adsorption capacity of a column as well as total adsorption of individual REEs were calculated from measured or modeled breakthrough curves via mass balance (Brewer et al., 2019a; Tan & Hameed, 2017):

$$(18)\ q = \frac{QC_o \int_{t=0}^{t=\infty} 1-\frac{C}{C_o}dt - \varepsilon\frac{\pi D^2 L}{4}C_o}{m}$$

where q is the adsorption capacity (mg/g), Q is the inlet flow rate (mL/min), C_o is the feedstock rare earth concentration (mg/mL), C is the effluent concentration (mg/mL), D is the column

diameter (cm), L is the bed height (cm), ε is the bed void fraction (mL void/mL bed), m is the mass of bioadsorbent (grams), and t is time (minutes).

3.3 Results and Discussion

3.3.1 Biosorption of Mixed REE in Batch Mode

We developed a chemical model that characterizes rare earth adsorption in batch mode to the PEGDA-encapsulated microbe beads. Small differences in ion size can lead to differential sorption behavior of the REEs to both native and LBT surface sites. While we incorporated LBT-REE binding constants from Nitz. et al. (2004), values for carboxyl-REE binding were estimated using a linear free energy relationship developed initially by Fein et al. (2001). A LFER may be implemented if a strong correlation exists between the binding free energies of a surface site-metal complex and an aqueous organic acid-metal complex. This can occur when both surface and aqueous complexes share similar binding modes with the metal of interest. In our case, acetate binding to REEs is representative of monodentate complexation of REEs to naturally occurring carboxyl surface sites on *E. coli* cells (Fein, Martin, and Wightman 2001; Ngwenya et al. 2010).

Using our combined LFER approach and use of Nitz. et al (2004) stability constants (Table 3.1), our model agrees well with the experimentally generated batch adsorption data for a mixed-REE solution (Figure 3.2a). Importantly, this approach is based on chemical trends of the adsorption thermodynamics of carboxyl and LBT sites with REEs and other metals. Thus, we avoid the need for empirically fitting individual REE surface stability constants. Middle/heavy REEs such as Sm and Eu are the strongest binding elements to the engineered surface. In contrast, light rare earths La and Ce are the weakest binders. The model predicts a similar trend, generally giving adsorbed concentrations within ± 1 standard deviation of the experimentally measured values. This binding affinity trend is correlated with the relative contribution of LBT sites to the overall adsorption (Figure 3.2b). Approximately 50% of the adsorbed Sm and Eu is bound to LBT sites, compared to <10% of the total adsorbed La and Ce. Because the LBT sites bind rare earths with $\log_{10}K$ two orders of magnitude greater than that for carboxyl-REE complexation, we attribute the increased Sm and Eu binding affinity to a more prevalent LBT binding mechanism.

We note that the model slightly overpredicts Y adsorption. While small discrepancies between experimental and modeled batch adsorption data can be reduced by allowing binding constants to carboxyl and LBT sites to be optimized to better fit the batch adsorption data, we did not attempt to parameterize the stability constants for the individual REEs, because this would generate 15+ additional model parameters with very few additional constraints. Furthermore, these solved variables would be co-dependent and highly conditional, limiting their use to this specific solution chemistry. We conclude that the reported binding constants (Table 3.1) are appropriate approximations in successfully predicting the batch adsorption behavior of all the rare earths to the engineered dLBTx8 *E. coli* cell surface.

Table 3.1. Binding constants for LBT- and carboxyl-REE surface complexation reactions and respective diffusion coefficients for multicomponent diffusion transport

REE	LBT-REE $\log_{10}K$ *Nitz et al. (2004)*	Carboxyl-REE $\log_{10}K$ *Ngwenya et al. (2010)*	Diffusion coefficient × 10^6/ cm^2/sec *Martelli et al. (2013)*
La	5.46	4.62	6.29
Ce	6.02	4.83	6.26
Pr	6.30	4.81	6.12
Nd	6.57	4.76	6.18
Sm	6.99	4.97	6.09
Eu	7.21	4.92	5.85
Gd	7.08	4.74	5.76
Tb	7.24	4.74	5.64
Dy	7.15	4.74	5.57
Ho	7.18	4.72	5.65
Er	7.11	4.72	5.61
Tm	7.05	4.72	5.71
Yb	7.00	4.63	5.39
Lu	6.89	4.74	5.52
Y	7.18	4.72	5.65

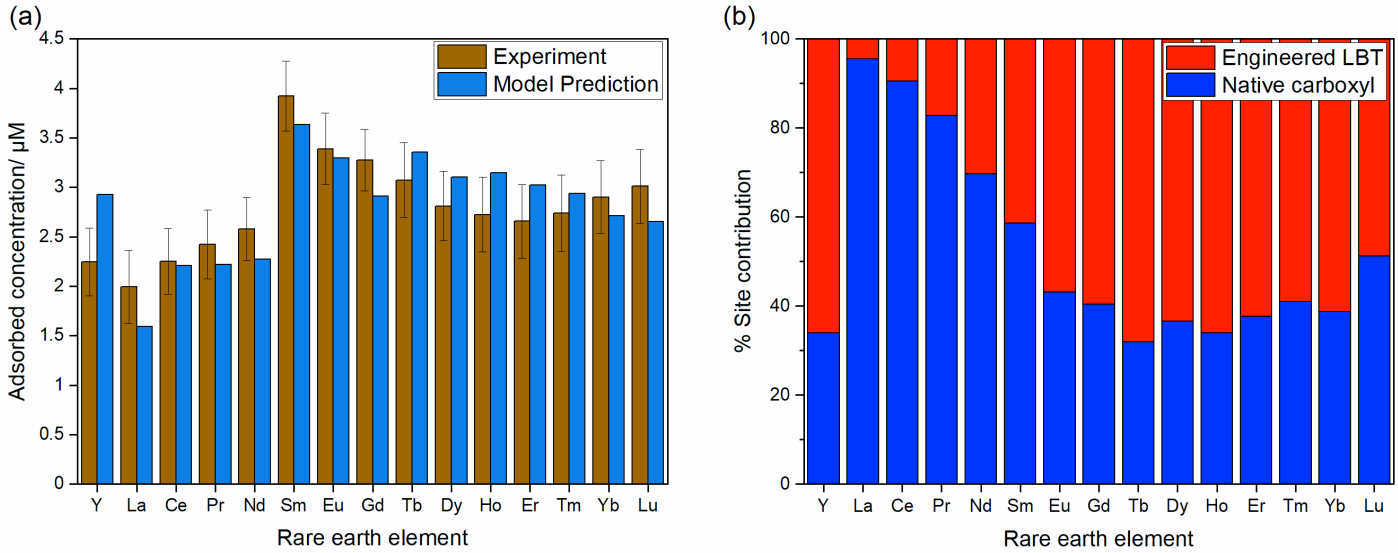

Figure 3.2 Batch adsorption data on PEGDA-encapsulated microbe beads for a mixed solution containing 5 µM of each rare earth and a cell suspension density of 0.36 dry g/L at pH 6. (a) Comparison of measured and modeled adsorption for the bulk adsorbent, and (b) modeled contributions of LBT and carboxyl sites to overall adsorption.

3.3.2 REE Separation from a Mixed Lanthanide Feedstock by Biosorption Under Flow

We coupled our validated chemical model describing REE adsorption with a physical dual-porosity model that describes both advective-diffusive inter-bead and diffusive intra-bead transport. Continuous flow experiments of Nd were used to calibrate a 1-D reactive transport model by solving for dispersion and intraparticle diffusion coefficients (Figure 3.3, Supporting Information 3.4, 3.5). Our estimates of 2.22×10^{-8} m^2/s and 1.31×10^{-12} m^2/s for the dispersion and intraparticle diffusion coefficients, respectively, were within reasonable range of previously determined literature values (H. J. Park and Tavlarides 2010; Zhou et al. 2013; D'Angelo and Panzer 2017; Aaron Brewer et al. 2019). An empirical Vermeulen model fit yields an intraparticle diffusion coefficient of 6.8×10^{-13} m^2/s for the same data set (Brewer et al., 2019). The close agreement between our model simulations and experimental breakthrough data with varying inlet Nd concentrations ranging from 50 to 1500 µM (Figure 3.3) provides a strong validation of the advection-reaction-diffusion modeling approach.

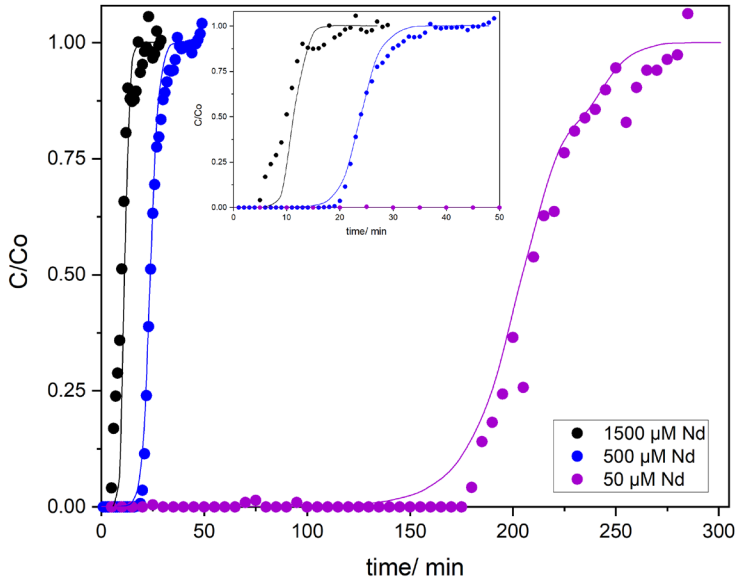

Figure 3.3 Experimental data (dots) and modeling predictions (lines) of breakthrough curves using a 15 x 0.5 cm column packed with 23 dry g/L dLBTx8 *E. coli* under 1 mL/min flow rate and varying inlet metal concentrations

Validation of the model for selective REE separation was investigated using a breakthrough curve for a fixed-bed column packed with the engineered strain of *E. coli*. We measured the breakthrough of 15 REEs using a 100 x 1 cm column with 23 dry g/L cell suspension under 1 mL/min flow rate (Figure 4a). The 500 µM equimolar inlet concentration of each rare earth saturated the column and caused breakthrough at approximately 78 min. The light rare earths including La and Ce had a breakthrough $C/C_o > 1.0$ due to selective displacement of these elements by the heavier REEs, indicating that the biosorbent has a weaker affinity for the LREEs. More specifically, the peaks exceeding C/C_o of 1.0 indicate regions of desorption, under which competition for surface sites of the bacteria cause less strongly sorbing species to be displaced by more tightly binding rare earths (Zhou et al. 2013).

We used our calibrated 1-D reactive transport model to simulate a continuous flow experiment of 500 μM inlet REEs under 1 mL/min flow rate at pH 6 on a 100 x 1 cm column. Our model predicts breakthrough time and C/C_o peaks exceptionally well (Figure 3.3a), with La showing peaks greater than 1.0 and middle/heavy rare earths such as Eu showing a slower breakthrough. We note a limitation in characterizing Y breakthrough, likely due to the overestimation in the thermodynamic Y-LBT or Y-carboxyl binding constants. This is evidenced by an overestimation in Y batch adsorption as well (Figure 3.2a), indicating that our estimated surface affinities for Y may require further refinement. Nonetheless, the model accurately predicts the biosorption of most rare earths to the immobilized bacteria, especially given a five fold increase in column length and a two fold increase in column diameter compared to the 20 x 0.5 cm dimensions of the calibration column. To more closely verify our model's performance, we computed the quantity of each REE bound to the 100 cm model column at varying post-breakthrough time points leading up to the 98th min (when we stopped our experimental collection of the effluent) and compared the values with experimental data. Most of the values fall on a 1:1 line, showing the strong predictive nature of the model (Figure 3.4b). As the time passes from the 78-minute breakthrough point to the 98-minute experiment end, the modelled adsorbed REE (mg) in the column converges to similar experimental values. The dynamic nature of REE separations in the fixed-bed column increases model uncertainty near breakthrough, as is shown by the model simulation points falling further away from the 1:1 model-experimental line at the 78-minute time step. We observed that the simulated values slightly overpredict adsorption compared to experimentally measured adsorbed REE amounts. As the column reaches closer to an equilibrium state, though, the model points fall closer to the 1:1 model-experiment line. This finding provides further evidence that our chemical model in batch accurately describes equilibrium REE adsorption to the engineered microbial surface. To check statistical significance, we performed a χ^2 test between modeled and experimentally generated adsorbed REE masses to the 100 cm column at the 78th, 84th, 90th, and 96th minute. With a null hypothesis that experimental and modeled data are not statistically different, we report χ^2 (degrees of freedom = 59) = 4.21, p = 1.0. Under a 95% confidence interval, we cannot reject the null hypothesis, suggesting that our model's predicted adsorbed REE masses are not statistically different from the experimentally generated data.

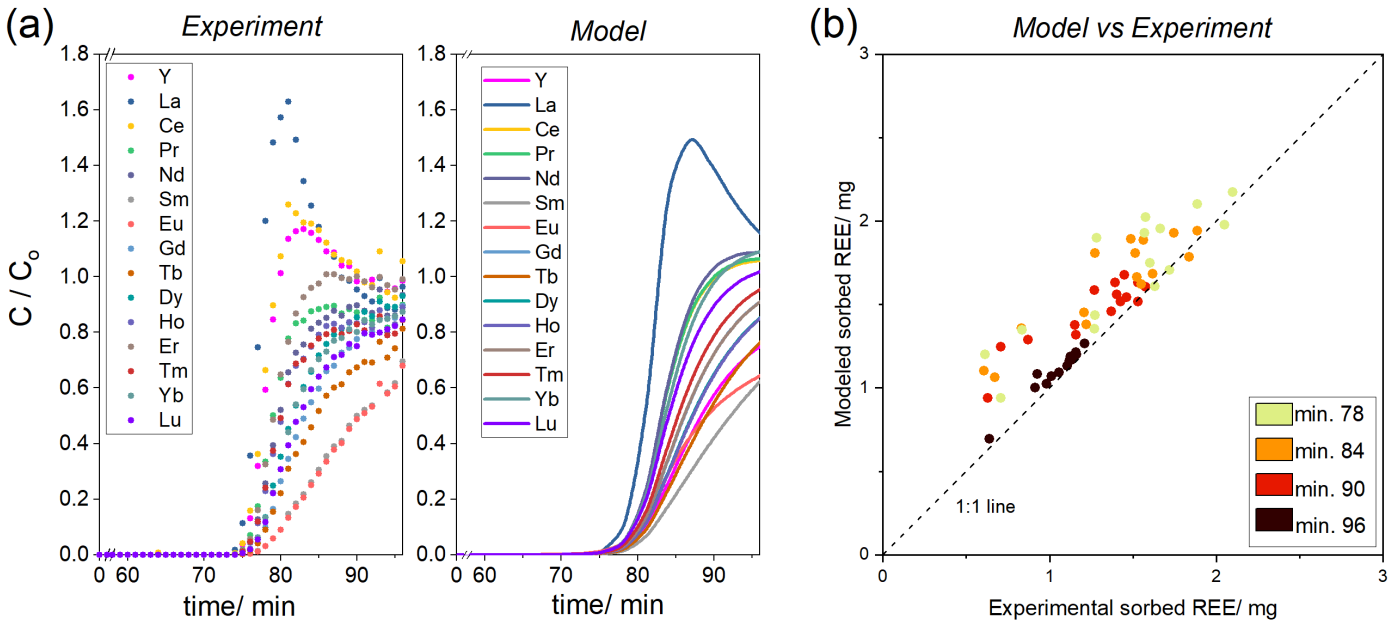

Figure 3.4 (a) Experimental and modeling results of breakthrough curves using a 100 x 1 cm column packed with 23 dry g/L dLBTx8 *E. coli* under 1 mL/min flow rate and a 500 µM equimolar mixed inlet solution of each rare earth, and (b) modeled vs. experimental results of adsorbed REEs for the same column at the 78th, 84th, 90th and 96th min. Modeled simulations of total sorbed REE are consistently found to be slightly greater than the experimentally determined sorbed REE amounts due to overestimated thermodynamic stability constants (see Figure 3.2a).

3.3.3 Time Evolution of Rare Earth Element Separation

Prior to complete equilibration of the column biosorbent material with the influent solution, the bulk REE composition of the biosorbent evolves dynamically over time, reflecting a complicated progression of site-specific competitive exchange reactions in a dynamically evolving intrabead pore fluid composition. The temporal evolution of bulk sorbent composition presents an opportunity to selectively tune the recovery of specific elements. Figure 3.5 illustrates the evolution of REE purity of the bulk adsorbent as a function of time, where the REE purity at a given time is defined as

$$(19)\ \text{Purity} = {}^{n_{REE,i}}\!/_{\sum n_{REE,i}} \times 100\%$$

where n is the surface excess of REE i, and Σn is the summation of all REE surface excess. Note that the total adsorbed REE content of the biosorbent also increases over time until the point of surface saturation, so the purity is not a complete measure of REE separation efficiency. The light rare earths such as La and Ce quickly decrease in percent purity in the adsorbed fraction after the 78-minute breakthrough mark (Figure 3.5). In contrast, middle/heavy rare earths such as Eu, Sm, and Tb increase in purity during the 18 minutes of modeled flow-through after breakthrough. As observed in Figure 4a, La decreases from $C/C_o \sim 1.6$ to 1.0 between breakthrough and the end of the experiment. At longer times (200 min), Eu is enriched relative to La by a factor of 3.03. The adsorbed composition of the 100 cm column over time (Figure 3.5) clearly demonstrates that a

competitive adsorption process occurs, where the more tightly binding middle/heavy REEs replace the light REEs post-breakthrough. The adsorbed column composition becomes enriched in these HREEs because these metals have a higher binding affinity to the cell surfaces compared to the light metals (Table 1). The elements Eu and La have similar carboxyl-REE $\log_{10}$K's of 4.92 and 4.62, respectively, so if binding to carboxyl sites alone were responsible for separation, Eu/La enrichment should not exceed a factor of 2. However, the LBT-REE binding constants for Eu (7.21) and La (5.46) are separated by almost two orders of magnitude. Despite the LBT sites being 3 times less prevalent than carboxyl sites (Chang et al. 2020a), LBTs contribute substantially to REE separations (Figure 3.6). We observe from the model output that one reason for an increase in Eu purity relative to La at breakthrough is because the concentration of Eu bound to LBTs overtakes La bound to carboxyl groups. Under this new regime where Eu-LBT binding is on the same order of magnitude as La-carboxyl binding, the low concentration, high affinity site type becomes an important adsorbing site and plays a critical role in separating the important rare earths. Another reason for an increase in Eu purity is the high-abundance carboxyl groups that are desorbing light REEs post-breakthrough, freeing up adsorption sites for Eu complexation (Figure 3.6).

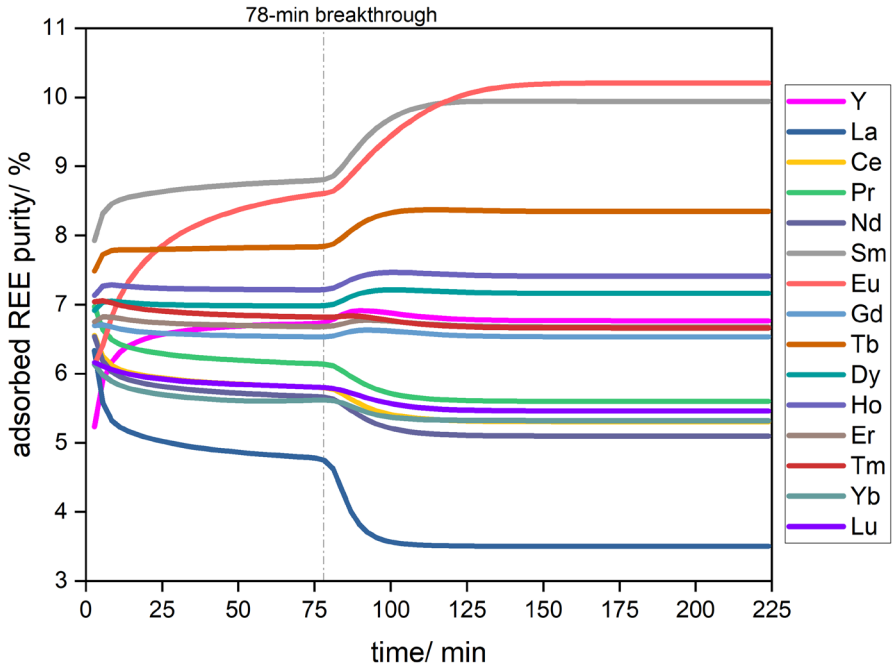

Figure 3.5 Modeled values of adsorbed REE purity as a function of time until equilibrium is reached. A 100 x 1 cm column packed with 23 dry g/L dLBTx8 *E. coli* was modeled under 1 mL/min flow rate of 500 µM equimolar inlet solution of each rare earth

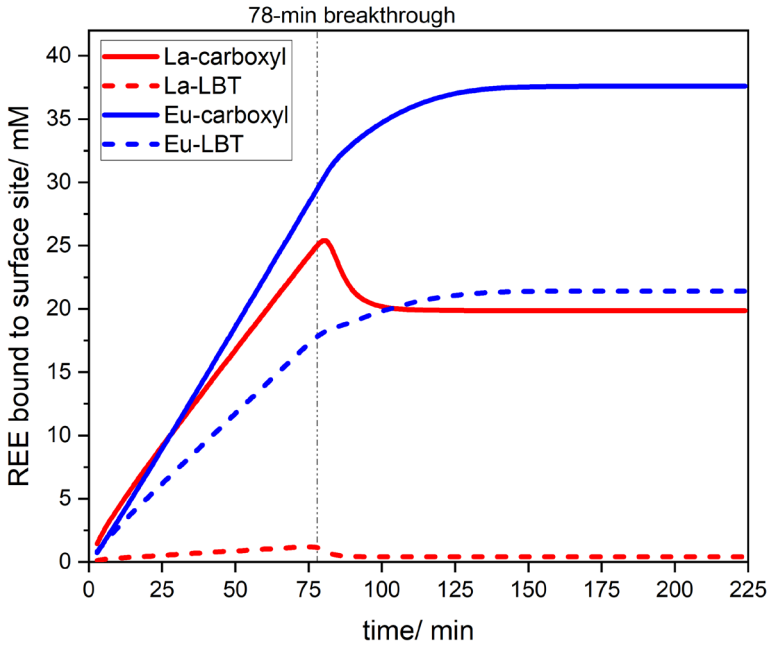

Figure 3.6 Modeling simulations of site-specific La and Eu binding. A 100 x 1 cm column packed with 23 dry g/L dLBTx8 *E. coli* was modeled under 1 mL/min flow rate of 500 µM equimolar inlet solution of each rare earth

Continued elution of the mixed solution through the column yields maximum separations of HREEs and LREEs at long times (200 min). However, the longer the extraction is run post-breakthrough, the lower the overall REE recovery efficiency, as increasing amounts of REEs are lost to the effluent. To quantify this, we define percent recovery for a given REE *i* as

$$(20)\ \%\ \text{Recovery} = \frac{m_{\text{REE},i}(t)}{m_{\text{REE},i}(t) + \varepsilon V(t) C_o + w_{\text{REE},i}(t)} \times 100\%$$

where $m_{\text{REE},i}(t)$ is the moles of REE *i* adsorbed to the column at time *t*, $\varepsilon V(t)$ refers to the volume filled at time *t* by the column pore fluid, and $w_{\text{REE},i}(t)$ is the moles of REE *i* not adsorbed and found in the effluent waste at time *t*. While separation quality, as exemplified by our Eu/La separation factor, increases over time post-breakthrough, we are also aware that some rare earths are lost as they pass through the saturated column (Figure 3.7). We observe a fast decrease in percent Eu recovered post-breakthrough because the column becomes saturated and significant amounts of Eu cannot displace other REEs for binding sites and are eluted. In contrast, Eu separation with respect to La increases post-breakthrough from two- to three-fold Eu enrichment. This tradeoff between separation quality and percent recovery should be weighed carefully and the optimal point to end the extraction process depends on important economic factors, such as the profit gained from enrichment of a target REE in contrast to the cost of eluting and wasting other REEs. One solution to this challenge is to run multiple columns in series, such that the residual waste of each rare earth during the 18 minutes post-breakthrough can be allowed to pass through and further collect in an unsaturated, fresh column. Importantly, these findings highlight the importance of developing a highly predictive chemical model for REE adsorption, as many

potential changes to the experimental setup and chromatographic separation approach (such as column length, width, and flow rate) can easily be simulated. In the following section, we discuss ways in which Eu can be further enriched compared to lanthanum by varying key chemical and physical factors.

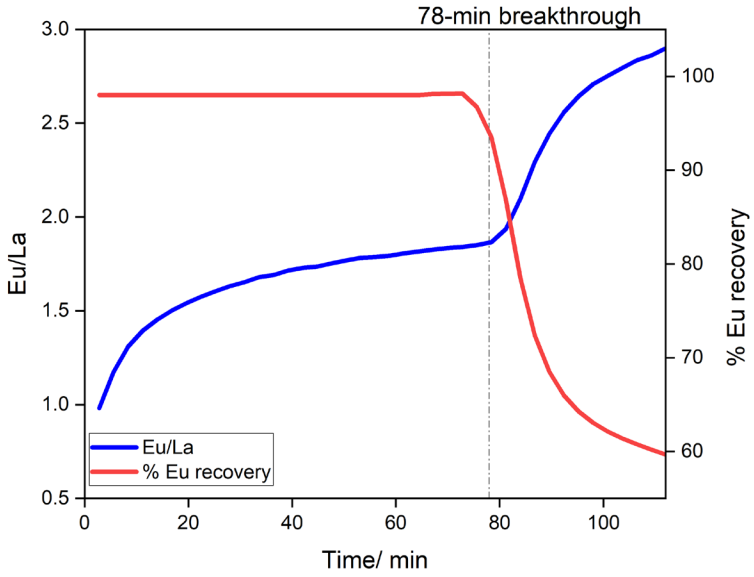

Figure 3.7 Modeled Eu/La separation tradeoff with Eu recovery efficiency as a function of time. The model simulated flow-through of a 500 µM equimolar inlet solution of 15 REEs under 1 mL/min for a 100 x 1 cm column

3.3.4 Process and Chemistry Modifications to Optimize Eu vs. La Separation

Having generated a model with strong predictive capabilities, we demonstrate one instance of how such a model can be effectively used. Implementation of empirical batch adsorption models such as Langmuir or Freundlich isotherms can only interpolate adsorption results based on the tested changes in chemical parameters such as ionic strength, pH, and biomass loading. However, using a quasi-mechanistic surface complexation modeling approach within a reactive transport model allows us to extrapolate beyond our experimentally generated data. To demonstrate the power of our quasi-mechanistic 1-D reactive transport model, we optimized our 100 x 1 cm column system by changing both physical and chemical factors. We highlight changes in cell density and pH as important chemical variables that influence the thermodynamics of the separation chemistry of rare earths. Cell density plays a key role in determining the total adsorption capacity of the column. Increasing cell density allows for more REEs to be adsorbed onto the column, but with the tradeoff that saturation and breakthrough occur at later time scales. pH is an important chemical parameter to investigate because it controls surface site speciation. While lower pH values will cause carboxyl and LBT groups to both be protonated, higher pH values will cause carboxyl groups to de-protonate, allowing those sites to more readily participate in REE binding. As surface complexation models account for the protonation of surface sites, changes in pH are easily accounted for as proton competition reactions with other sorbing species.

Taking Eu and La as proxies for middle/heavy and light rare earths that have quite different commercial applications, we simulated enrichment in Eu over La with varying cell density, pH,

and flow rate (Figure 3.8a,b). Higher densities of dLBTx8 *E. coli* can lead to an enrichment in middle/heavy rare earth elements (Park et al., 2017), but in this case do not significantly impact separation dynamics when simulating up to 98 minutes of flow-through. This is because a higher cell density increases the time taken to saturate the column and for the biosorbent to experience competitive displacement between middle/heavy and light REEs. In comparison, a low pH of 3.0-3.5 yield the largest separation of Eu from La when using a 100 x 1 cm column under 1 mL/min flow rate and a 500 μM equimolar inlet solution of each rare earth (Figure 3.8a). A decrease in pH results in the protonation of carboxyl groups (pK_a of 4.98 as reported by Chang et al., 2020), causing competition for the site type between protons and rare earths. This reduces the effectiveness of REE-carboxyl group adsorption and increases the middle/heavy rare earth enrichment effect of the lanthanide binding tag site type. Optimal REE separation at low pH regimes is promising because many REE-containing feedstocks, such as the Bull Hill Mine (WY) and the Round Top Mountain mineral deposit (TX), naturally exist at more acidic pH conditions (D. M. Park et al. 2017). Furthermore, high pH regimes beyond pH 6.5 can cause precipitation of rare earths as REE-hydroxides as observed by our model's positive saturation indices of particularly the heavy rare earths, such as Tb, and Lu, which result in lower available REE for biosorption.

We further optimized for Eu/La separation by adjusting flow rate as an important physical parameter (Figure 3.8b). At elevated flow rates, we observe a similar maximum Eu/La separation factor of ~3.6 by the 98-minute model simulation end. However, faster flow rates achieve this Eu/La = 3.6 enrichment 48 minutes earlier (Figure 3.8c), which poses benefits at the industrial scale when considering a daily production/enrichment target objective. Our quasi-mechanistic reactive transport modeling predictions shown in Figure 3.8 highlight the importance of exploring both chemical and physical parameter spaces with a consideration for time evolution. These combined factors can play an important role in influencing the total recovery, adsorbed column purity, and separation efficiency of specific REEs.

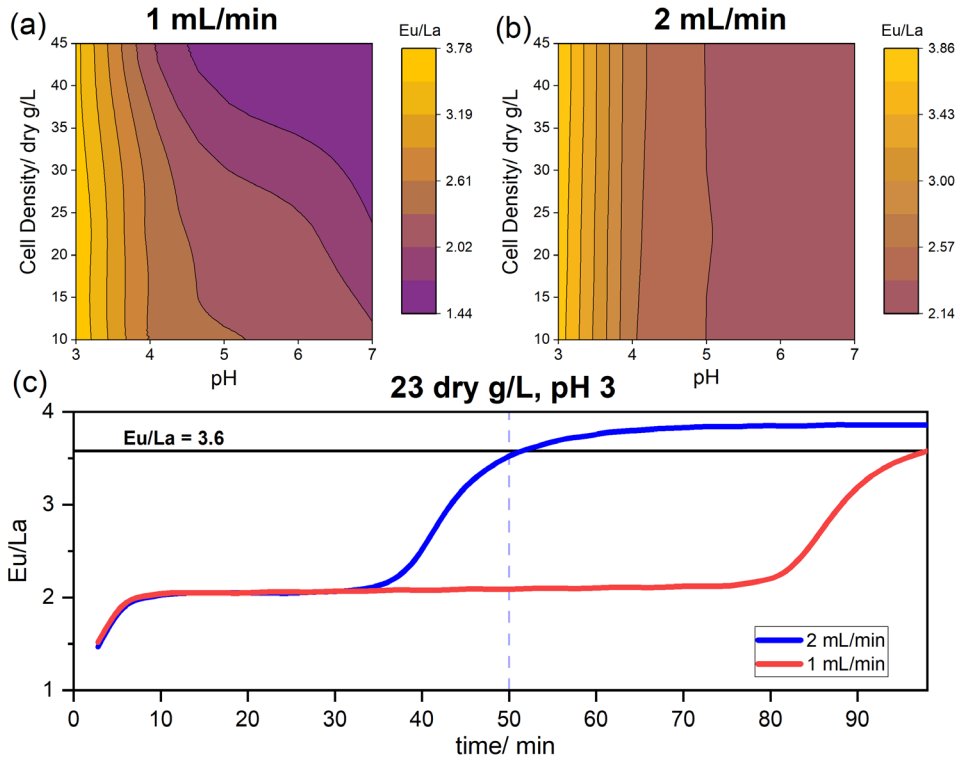

Figure 3.8 Simulated Eu/La separation for 100 x 1 cm columns with a range of cell densities after 98 minutes of flow-through of a 500 µM equimolar inlet solution of REEs over a pH range of 3-7 under (a) 1 mL/min and (b) 2 mL/min flow rates. (c) Eu/La separation time evolution for 2 mL/min and 1 mL/min flow-through simulations using 23 dry g/L cell suspension at pH 3

3.4 Conclusions

The foregoing results demonstrate a predictive modeling approach that allows targeted separation between middle/heavy versus light rare earth metals using fixed-bed columns of immobilized, LBT-engineered microbes. This study highlights the power of reactive transport modeling, allowing for simultaneous exploration of physical, chemical, and temporal factors that optimize Eu separation from La. While some experimental parameters are difficult to test in the lab or require extensive time to run, our calibrated model can not only be executed quickly, but also has the potential to account for variations in complicating factors such as changes in intra- and interbead porosities and competing heavy metals co-existing in naturally occurring feedstocks. As our careful validation and checks on both the thermodynamic and physical transport parameters show, our one-dimensional reactive transport model can significantly reduce time taken to optimize a wealth of both chemical and physical variables in achieving best separation of target rare earth elements. Future work should address the effects of higher ionic strength solution matrices on the surface complexation model component of the reactive transport model. Because rare earth elements present in geothermal fluids and mine tailings can exist in brine solutions at high ionic strengths (>1 M), it is critical to address both electrolyte cation competition for adsorption sites as well as the electrostatic treatment of the bacterial electric double layer. Such work will increase the potential applicability of this model to many naturally occurring environmental solutions containing rare earth elements.

CHAPTER 4

Arthrobacter nicotianae adsorption of neodymium to investigate multi-site surface complexation mechanisms of gram-positive soil bacteria

4.1 Introduction

Bacteria play an important role in the fate and transport of metals in surface and subsurface environments (Yee and Fein 2002). More specifically, the high surface area and negative electrostatic charge characteristic of bacterial cells under circumneutral pH conditions commonly found in soils result in metal adsorption to the anionic bacterial cell surface (Beveridge and Fyfe 1985; Fein 2000). Although underlying subsurface metal transport mechanisms have not been well elucidated yet, it is widely understood that bacteria can co-transport adsorbed metals through preferential flow paths in porous soil structures (McCarthy and Zachara 1989). Due to the high abundance of bacteria in soils and sediments, roughly on the order of 10^7 to 10^{10} cells/gram (Raynaud and Nunan 2014), bacterial surfaces can influence the mobility of metals. Relevant metals that bind to bacteria include uranium (Haas, Dichristina, and Wade 2001; Yung and Jiao 2014) and cadmium contaminants (Loukidou et al. 2005; Hatano and Tsuruta 2017; Butzen and Fein 2019) as well as trace rare earth elements (REEs) released from natural mineral deposits and geothermal brines (Wood 2001; Emmanuel et al. 2012; Takahashi et al. 2010a; Kang, Csetenyi, and Gadd 2019). REEs are particularly important metals to investigate in soil systems. While they are usually present at low concentrations (low ppm to ppb range), REEs may still pose a strong control over the cell surface's adsorption capability due to high-affinity REE surface complexation interactions (Andrès, Le Cloirec, and Texier 2003; Ngwenya et al. 2010; Martinez, Pourret, and Takahashi 2014). Because phosphate functional groups existing on gram-positive bacteria form highly stable surface complexes with REEs, bacteria preferentially adsorb these trivalent cations over more commonly occurring divalent heavy metals (Fein 2000; Fein, Martin, and Wightman 2001).

Gram-positive bacteria possess a variety of surface sites, including phosphodiester, carboxyl, phosphoryl, amine, amide, and hydroxyl groups (Figure 4.1) (Beveridge and Fyfe 1985; Ngwenya, Sutherland, and Kennedy 2003; Fein et al. 2005; Hong and Brown 2006). Carboxyl, amide, and hydroxyl functional groups exist in the form of N-acetylmuramic acids and N-acetylglucosamines. These functional groups are commonly found in the thick peptidoglycan mesh layer of the gram-positive bacterial surface. Covalently anchored to the peptidoglycan, wall teichoic acids (WTAs) contain repeating units of anionic glycopolymers that are linked by phosphodiester moieties. As WTAs protrude out of the cell membrane, moieties such as phosphodiester linkage units are prime available sites for adsorption of metal counterions (Thomas and Rice 2015). Lipoteichoic acids (LTAs) also possess phosphodiester-linked glycopolymers but are instead anchored to the bacterial bilipid membrane *via* glycolipids. As WTAs have repeating glycopolymer units ranging from 40 to 60 residues, the cell surface is naturally abundant in phosphodiester moieties (Brown, Santa Maria, and Walker 2013). Additional to phosphodiester sites, the cell surface also possesses phosphoryl functional groups in the form of the polar head groups found on the bilipid cell membrane.

Carbonyl-based amide functional groups commonly present in protein structures are typically neutrally charged and could be thought to have weaker electrostatic interactions with REEs in comparison with REE adsorption onto negatively charged surface ligands. Maleke et al. (2019), however, showed this to be a misconception as they observed europium adsorption onto

these site types for the thermophilic bacterium, *Thermus scotoductus*. This interaction occurs based on a resonance structure mechanism (Condamines and Musikas 1992; Feng, Schmidt, and Weiss 1996; Cui et al. 2007; Gholivand et al. 2018), whereby the delocalization of the C=O carbonyl pi-bond allows the formation of a C-O^- site (Figure 4.2). This process is driven by the presence of a strong Lewis acid, which can pull the electron density away from the initial C=O double bond. The resultant C-O^- site creates a particularly favorable electrostatic interaction with the trivalent rare earth metals and other charge-dense cation metals. Thus, when developing surface complexation models (SCMs) of gram-positive bacterial surfaces, each of these discussed functional groups should be carefully considered as important endmembers in characterizing the bulk REE adsorption process.

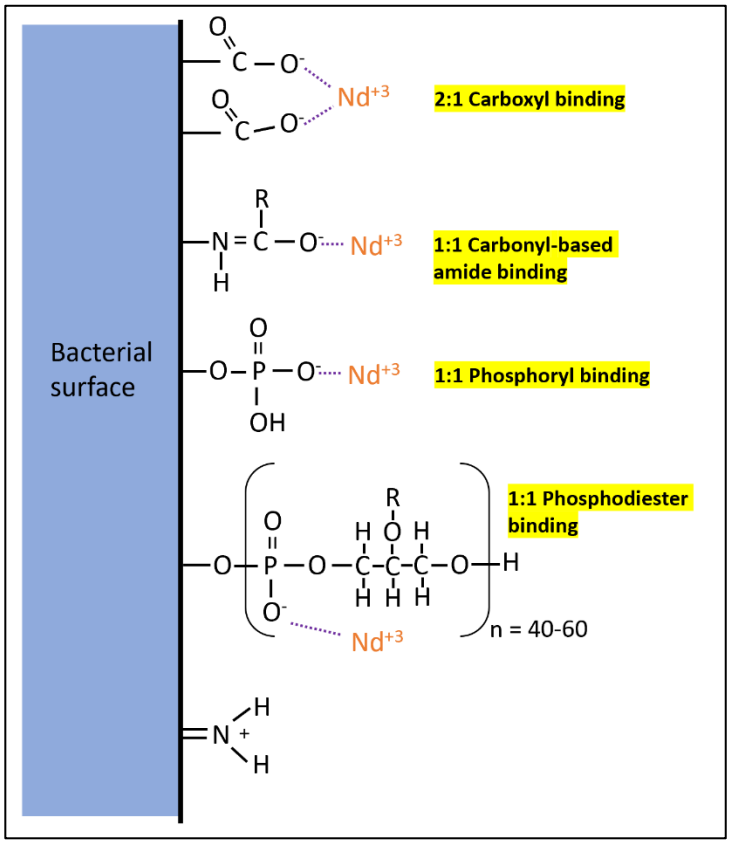

Figure 4.1 Schematic of a gram-positive bacterial surface including relevant surface sites and neodymium binding modes implemented in this study's surface complexation model

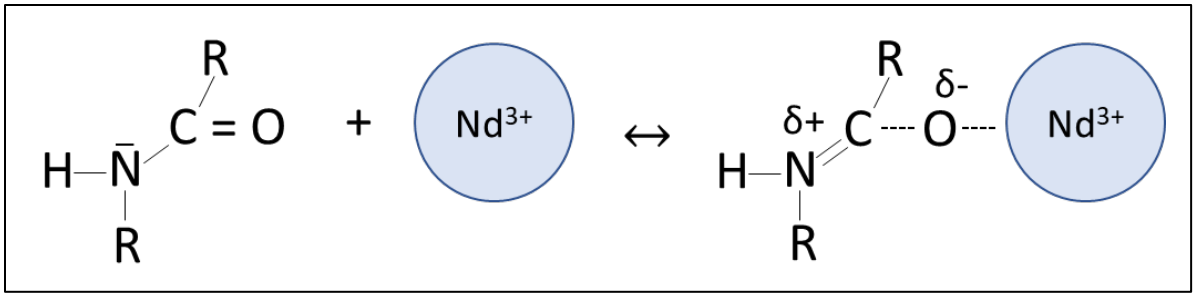

Figure 4.2 Resonance structure and pi-bond delocalization of a carbonyl-based amide functional group in the presence of neodymium, a strong Lewis acid

All of the aforementioned site types have been identified on the cell surface using fourier transform infrared spectroscopy (FTIR) (Heinrich et al. 2007; Tourney et al. 2008). Time resolved laser fluorescence spectroscopy (TRLFS) (Texier et al. 2000; Markai et al. 2003) and extended X-ray absorption fine structure (EXAFS) spectroscopy (Ngwenya et al. 2009; Takahashi et al. 2010a) present additional information on the metal binding mode and relative REE affinities to the cell surface. Carboxyl and phosphate sites have been suggested to be the predominant adsorbing functional groups on bacterial surfaces at REE concentrations and pH commonly found in soils (Ngwenya et al. 2010). However, while past studies investigating bacteria-based REE biosorption have successfully fitted adsorption edge and isotherm data to one- or two-site surface complexation models (Markai et al. 2003; Ngwenya et al. 2010), the majority of these studies do not consider the low pK_a phosphodiester or the carbonyl-based amide sites as readily active REE binding surface ligands. Likely, phosphodiester groups are overlooked because of their low acidity constant, causing all sites to be fully deprotonated in the pH 3.0 to 11.0 range commonly investigated in acid-base titrations of bacterial surfaces (Ngwenya, Sutherland, and Kennedy 2003; Tourney et al. 2008). However, although phosphodiesters are inactive for proton exchange in the relevant studied pH regime, these anionic sites are readily available for adsorption with trivalent REE cations (Ngwenya et al. 2009). Carbonyl-based amide functional groups have also been overlooked, mostly in part because of their common neutrally charged resonance state (Figure 4.2). However, in the presence of strong Lewis acids, such as actinides and lanthanides, lone pair electron delocalization of the nitrogen-containing amides in conjunction with pi-bond movement in the formation of $C\text{-}O^-$ sites lead to the presence of reactive ligands that strongly bind metals (Condamines and Musikas 1992).

In this study, we investigate the gram-positive soil bacterium, *Arthrobacter nicotianae*, as a model soil bacterium that can adsorb REEs. As *A. nicotianae* has the highest metal adsorbing capacity of any known bacteria in current literature (Tsuruta 2005), we highlight neodymium (Nd) surface complexation to *A. nicotianae* as an upper bound to the REE adsorption capacity of soil bacteria. We apply FTIR as an analytical technique to obtain qualitative site-specific adsorption information. FTIR is a commonly used technique to determine the presence of various functional groups in biological samples based on each moieties' unique absorption of the infrared laser (Naumann 1984). IR radiation is non-destructive to bacteria, and can be useful in investigating intact cells or isolated cell walls (Tourney et al. 2008; Castro et al. 2010). Adding an attenuated total reflectance (ATR) accessory to the FTIR analyzer (ATR-FTIR) allows easy, *in situ* analyses of wet cell suspensions without the need for traditional KBr pellet pre-processing. Because IR radiation for a diamond ATR crystal at a typical 45° incident angle and 1000 cm^{-1} wavenumber

penetrates the sample at a 1.66 μm depth (Bruker Optics 2011), single ATR-FTIR analyses do not collect surface-specific information on soil bacteria that are typically less than 0.5 μm in diameter (Bakken and Olsen 1987). However, as many batch adsorption studies indicate fully reversible, surface mediated adsorption mechanisms, conducting multiple ATR-FTIR analyses pre- and post-adsorbate addition can in fact provide valuable surface-specific metal adsorption information in the form of IR difference spectra.

In this chapter, I develop a novel surface complexation model for a gram-positive soil bacterium, *Arthrobacter nicotianae*, that extends beyond commonly accepted surface functional groups to include phosphodiester and carbonyl-based amide groups. Using the combined results of acid-base titration experiments, adsorption isotherm experiments, and ATR-FTIR spectra, I propose a set of surface complexation reactions that control neodymium biosorption by *A. nicotianae*. This four-site surface complexation model includes phosphodiester, carboxyl, phosphoryl, and amide-base adsorption mechanisms that are supported by qualitative ATR-FTIR measurements. The introduction of new REE adsorption mechanisms in the form of phosphodiester and carbonyl-based amide groups contrasts dramatically from previous SCMs whereby only one or two sites are assumed to exist on the cell surface. This study attempts to incorporate the complexities of gram-positive bacterial surfaces in order to better understand how competition between varying surface ligands control neodymium biosorption under various pH and metal loading conditions.

4.2. Materials

4.2.1 Growth and preparation of bacteria

De-frosted stock of *A. nicotianae* ATCC 15236 was inoculated in a test tube containing 4 mL of Luria broth medium and that was then incubated aerobically for 24 hours at 30 °C using a rotary shaker (220 RPM). One milliliter of cells was then sub-cultured into a larger fifty milliliter volume of fresh Luria broth and incubated for another 24 hours under the same physical conditions. Park et al. (2020) show that following this growth procedure results in spherically shaped *A. nicotianae* in stationary phase with an average 1 μm diameter. Cells were centrifuged at 4000g for 10 minutes and wet cell pellets were collected for same-day experiments. Prior to experiments, wet cell pellets were washed with sterile 0.1 M NaCl twice to remove any residual growth medium. Small aliquots of wet cell pellets were set aside and dried overnight at 65 °C to determine water content. Growth experiments were conducted in triplicate for acid-base titration and batch adsorption experiments to determine standard deviations of experimental error.

4.2.2 Acid-base titration experiments

We conducted triplicate acid-base titrations on wet *A. nicotianae* cell pellets in order to determine site densities and deprotonation constants for the relevant surface functional groups. Cell pellets were placed in 30 mL of 0.1 M NaCl electrolyte, which had been bubbled with N_2 to purge any dissolved CO_2. The bacterial cell suspensions were immediately sealed, and the headspace was kept under positive N_2 pressure. A Titronic 300 automatic titrator using a monotonic equivalence point titration method was implemented to add the same volume (0.05 mL) of 0.1 M HCl or 0.1 M NaOH to the bacterial suspensions. A pH range of 3.5 to 10.0 was investigated to avoid irreversible cell wall damage caused by highly acidic and alkaline

environments (Borrok, Turner, and Fein 2005). pH was initially adjusted to 3.5 prior to an up-titration to 10.0.

4.2.3 Batch adsorption experiments

Varying concentrations (0 to 250 μM) of Nd were prepared using anhydrous $NdCl_3$ (Fischer Scientific; 99.9%). Homopiperazine-1,4-bis(2-ethanesulfonic acid) (HomoPIPES) was used to buffer solutions at pH 4.0 whereas 2-(N-morpholino)ethanesulfonic acid (MES) was used to buffer solutions at pH 6.0. *A. nicotianae* cells were grown and harvested as discussed above. Wet cell pellets were suspended in the appropriate buffer solution to create stock wet cell suspension solutions of ~0.3 dry g bacteria/L. Varying concentrations of $NdCl_3$ (62.5, 125.0, 250.0 μM) were mixed with the cell stock solution to obtain varying metal loading conditions at pH 4.0 and 6.0. Dilutions due to the mixing of Nd-containing solution and cell suspension density were accounted for. Neodymium-containing cell solutions were shaken for 1 hour at room temperature. Solutions were then centrifuged at 20,000g for 8 minutes. Neodymium concentrations in the supernatants were analyzed colorimetrically with Arsenazo III (Brewer et al. 2019a) at an absorbance of 652 nm using a Spectra Max Plus microplate reader manufactured by Molecular Devices. Total adsorbed Nd concentrations were calculated by subtracting the Nd present in the supernatant from the Nd control solutions that did not contain bacterial cells.

Resulting data for batch adsorption isotherms conducted in this experiment were compared with similar experiments reported in Park et al. (2020). Results from both this current and Park et al.'s study were pooled together to establish datasets for surface complexation modeling.

4.2.4 ATR-FTIR analysis of wet bacterial cell suspensions after batch Nd adsorption

A background spectrum of the ATR diamond crystal was collected. Aliquots of 0.1 mL wet cell pellets were gently placed on the diamond crystal and analyzed with 1,000 scans under a 4 cm^{-1} resolution within a 4000 to 400 cm^{-1} wavenumber range. Wet cell pellets were filtered using a 0.1μm nylon membrane filter and supernatants were then analyzed. The crystal was cleaned of bacteria between each ATR-FTIR analysis by gently wiping off any sample using a cotton material and the ATR crystal was rinsed with a small volume of distilled water. Post-processing of the IR spectra consisted of first baseline correcting the solution matrix and bacteria spectra. Isolated bacteria IR absorption was obtained by subtracting out the solution matrix peaks. IR difference spectra were also generated by subtracting Nd-loaded bacteria IR peaks from control no-Nd bacteria spectra at varying metal loadings. Final spectra were smoothed using a Savitzky-Golay filter that incorporated a polynomial order of 2 and 20 points of window examined (Ferreira et al. 2020).

4.2.5 Modeling acid-base titration data of gram-positive bacteria

A four-site constant capacitance model was implemented to model the experimental acid-base titration data. A four-site model was chosen to reflect realistic possible site types present on the surfaces of gram-positive bacteria in the form of phosphodiester, carboxyl, phosphoryl, and amine functional groups. Because amides have a high pK_a of 15.1 (Sigel and Martin 1982), amides would not experience proton exchange within the investigated pH 3.5-10.0 range of this study. Thus, amides were excluded from participating in proton adsorption/desorption and were not included in the acid-base titration modeling. Each site type's proton dissociation reaction can be expressed as follows:

(1) $R\text{-}POOH \leftrightarrow R\text{-}POO^- + H^+$

(2) $R\text{-}COOH \leftrightarrow R\text{-}COO^- + H^+$

(3) $R\text{-}POH \leftrightarrow R\text{-}PO^- + H^+$

(4) $R\text{-}NH_3^+ \leftrightarrow R\text{-}NH_2 + H^+$

Where POOH, COOH, POH, and NH_3^+ refer to phosphodiester, carboxyl, phosphoryl, and amine site types. Associated thermodynamic equilibrium constants for each reaction can be written as:

(5) $K_1 = \frac{[R-POO^-]a_H{}^+}{[R-POOH]}$

(6) $K_2 = \frac{[R-COO^-]a_H{}^+}{[R-COOH]}$

(7) $K_3 = \frac{[R-PO^-]a_H{}^+}{[R-POH]}$

(8) $K_4 = \frac{[R-NH_2]a_H{}^+}{[R-NH_3^+]}$

Where K is the conditional stability constant for each given reaction and $a_H{}^+$ is the proton activity.

Staying consistent with cell geometry and associated cell suspension density information provided by Park et al. (2020), a 197 m^2/dry g surface area was used in the surface complexation model. A constant capacitance of 8 F/m^2 was also implemented as was done in chapters 2 and 3 of this dissertation. Because titrations were conducted between pH 3.5-10.0, the low pK_a phosphodiester site type was constrained to a pK_a of 2.1 (Thomas and Rice 2015) to minimize unconstrained optimization. The site density of phosphodiesters was allowed to vary. The remaining site types that would reflect carboxyl, phosphoryl, and amine functional groups, were allowed to vary in pK_a and site density. Optimization of variables and fitting to experimental data were conducted using two approaches: (1) modeling of site pK_a and site densities to fit individual triplicate experiments followed by averaging of the results, and (2) modeling of site pK_a and site densities to fit a pooled dataset of all triplicate experiment data. Standard deviation errors for resulting site density calculations were compared between the two approaches to determine the ideal optimization method for the triplicate acid-base titration modeling.

4.2.6 Constraining multi-site surface complexation modeling of gram-positive bacteria

Phosphate-based REE-ligand interactions have been suggested to be monodentate (Texier et al. 2000; Takahashi et al. 2005). We thus apply 1:1 phosphodiester:Nd and phosphoryl:Nd binding stoichiometries in our surface complexation model (SCM). Although another surface complexation modeling study by Ngwenya et al. (2009) has shown monodentate carboxyl binding can non-uniquely describe adsorption edge data, TRLFS results coupled with additional surface complexation modeling have also suggested the feasibility of a 2:1 bidentate mononuclear adsorption mechanism between carboxyl groups and REEs (Markai et al. 2003). If we take a closer look, Markai et al. (2003) shows a 2:1 carboxyl:Eu interaction with a gram-positive *Bacillus subtilis* bacterial surface whereas Ngwenya et al. (2009) shows a 1:1 carboxyl:Er interaction with a gram-negative *Pantoea agglomerans* bacterial surface. Due to this study's focus on gram-positive bacterial surface-REE interactions, a 2:1 bidentate mechanism was considered for

carboxyl:Nd adsorption in accordance with modeling and TRLFS results for a gram-positive bacterial strain presented by Markai et al. (2003). This assumption is supported by Martinez et al. (2014), where a non-monodentate adsorption reaction between carboxyl groups and REEs was strongly suggested for the gram-positive bacteria, *B. subtilis*. Wood et al. (2000) further demonstrated that Nd^{3+} aqueous complexation with acetate as a model carboxylic acid compound is controlled by bidentate mononuclear Nd-$Acetate_2^+$ aqueous complexes at high acetate ligand concentrations.

In addition to these sites, a carbonyl-based amide adsorption reaction for neodymium was also considered. Due to the pi-bond delocalization and electron movement of the resonance structure mechanism across the C=O bond, carbonyl-based amide-metal interactions are commonly thought to be monodentate (Gholivand et al. 2018). Because the site density of the actively complexing $C\text{-}O^-$ resonance structure from amide groups vary with Lewis acid concentration, $C\text{-}O^-$ site density was incorporated into the model as a mathematical function rather than a fixed value. The function was determined by first establishing the maximum carbonyl-based amide concentration as 1:1.5 carboxyl:amide ratio (Jiang et al. 2004) at the maximum adsorption capacity determined in our adsorption isotherms. At other surface excess points, a linear proportionality was assumed such that at lower concentrations of metal bound, there would also be lower $C\text{-}O^-$ sites. Each of the Nd stability constants for phosphodiester, carboxyl, phosphoryl, and amide-based adsorption reactions were optimized by fitting to both surface excess (adsorption capacity) and distribution coefficient (surface selectivity) data simultaneously (Chang et al. 2020a). Standard deviations were calculated for binding constants by optimizing upper bound and lower bound surface excess and distribution coefficient datasets. These bounds were determined by addition or subtraction of the experimental standard deviation (± 1 sd) from the average surface excess or distribution coefficient data.

Reactions for each site type's complexation reaction with neodymium can be expressed as follows:

(9) $R\text{-}POO^- + Nd^{+3} \leftrightarrow Nd(R\text{-}POO)^{+2}$

(10) $2\ R\text{-}COO^- + Nd^{+3} \leftrightarrow Nd(R\text{-}COO)_2^+$

(11) $R\text{-}PO^- + Nd^{+3} \leftrightarrow Nd(R\text{-}PO)^{+2}$

(12) $R\text{-}NHCO^- + Nd^{+3} \leftrightarrow Nd(R\text{-}NHCO)^{+2}$

Where POO^-, COO^-, PO^-, and $R\text{-}NHCO^-$ refer to deprotonated phosphodiester, carboxyl, phosphoryl sites and a resonance-structure anionic amide site type, respectively. Amines were not considered for neodymium surface complexation due to their high pK_a, making them positively charged surface ligands that do not interact favorably with trivalent REEs under the pH 4.0 to 6.0 range studied in this work. Associated thermodynamic equilibrium constants for reactions (9)-(12) can be written as:

(13) $$K_5 = \frac{[Nd(R-POO)^{+2}]}{[R-POO^-][Nd^{+3}]}$$

(14) $$K_6 = \frac{[Nd(R-COO)_2^+]/([Nd(R-COO)_2^+]+[R-COO^-]+[R-COOH])}{([R-COO^-]/([Nd(R-COO)_2^+]+[R-COO^-]+[R-COOH]))^2[Nd^{+3}]}$$

(15) $K_7 = \frac{[Nd(R-PO)^{+2}]}{[R-PO^{-}][Nd^{+3}]}$

(16) $K_8 = \frac{[Nd(R-NHCO)^{+2}]}{[R-NHCO^{-}][Nd^{+3}]}$

Where K is the conditional neodymium stability constant for each given reaction. We note that the PHREEQC modeling program used in this study implements mole fractions in the place of surface species concentrations. This eliminates a problematic dependence whereby equilibrium constants are conditional upon the surface site concentrations used (Wang and Giammar 2013). In equations 13, 15, and 16 that describe monodentate neodymium binding reactions, the total site concentrations used for mole fraction calculations cancel out in the numerator and denominator of the expressions. However, in reaction 14, the denominator of the equilibrium constant for bidentate carboxyl binding of neodymium is squared. This implies the important incorporation of the total site concentration of carboxyl groups in the neodymium equilibrium constant for 2:1 carboxyl:Nd adsorption.

4.3 Results and Discussion

4.3.1 IR spectra of wet bacterial cell suspensions and elucidated functional groups

The ATR-FTIR spectra generated for wet cell suspensions of *A. nicotianae* at pH 4.0 and pH 6.0 (Figures 4.3a, 4.4a) exhibited commonly observed peaks presented by other gram-positive bacteria FTIR studies (Jiang et al. 2004; Tourney et al. 2008). Amide I, amide II, and amide III peaks are clearly seen in both pH 4.0 and 6.0 spectra at 1635, 1540, and 1332 cm^{-1} (Figures 4.3a, 4.4a). While the amide I peak refers to the vibrations of the C-O carbonyl bond, the amide II and III peaks refer to a C-N stretching vibration (Mayne and Hudson 1991). The amide II peak is also sensitive to amide I-II coupling in peptide units (Deflores et al. 2009), making its changes in peak intensity difficult to uniquely assign to changes in C-N vibrations. The shoulder of amide I at 1741 cm^{-1} corresponds to protonated carboxylic acid groups (Heinrich et al. 2007). The normalized ~1741 cm^{-1} peak is more prominent in the pH 4.0 spectrum compared with the ~1727 cm^{-1} peak in the pH 6 spectrum, indicating higher concentrations of protonated carboxyl groups at lower pH. Bands at ~1400 cm^{-1} indicated the presence of symmetric stretching induced by de-protonated carboxyl groups. Inversely related to the ~1741 cm^{-1} protonated carboxyl peak, the pH 6.0 spectrum shows a more intense peak for de-protonated carboxyl groups compared to the pH 4.0 spectrum. Phosphodiester groups are identified at 1230 and 1076 cm^{-1} in both pH 4.0 and 6.0 spectra, though it is difficult to ascertain relative absorbance magnitude differences between the two IR spectra. Peaks ranging between 950 to 1150 cm^{-1} were convoluted by the presence of both $P(OH)_2$ phosphate peaks and C-OH and C-C bonds found in polysaccharides and alcohols (Jiang et al. 2004). A peak at ~1458 cm^{-1} is associated with methyl/methylene deformation modes (Heinrich et al. 2007) and $-CH_2$ scissoring vibrations (Jiang et al. 2004). These ATR-FTIR measurements qualitatively confirm the presence of carboxyl, phosphate, and amide-based ligands within the *A. nicotianae* wet cell suspensions.

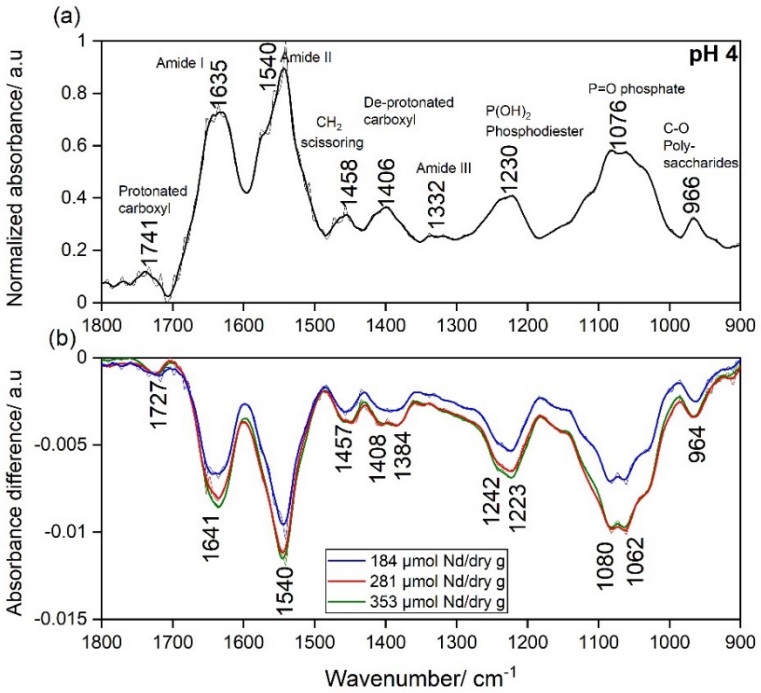

Figure 4.3 (a) Normalized ATR-FTIR spectra of wet cell suspensions of *A. nicotianae* at pH 4.0 and (b) associated difference spectra at varying Nd metal loadings. Thin and thick lines indicate non-smoothed and smoothed ATR-FTIR measurements, respectively.

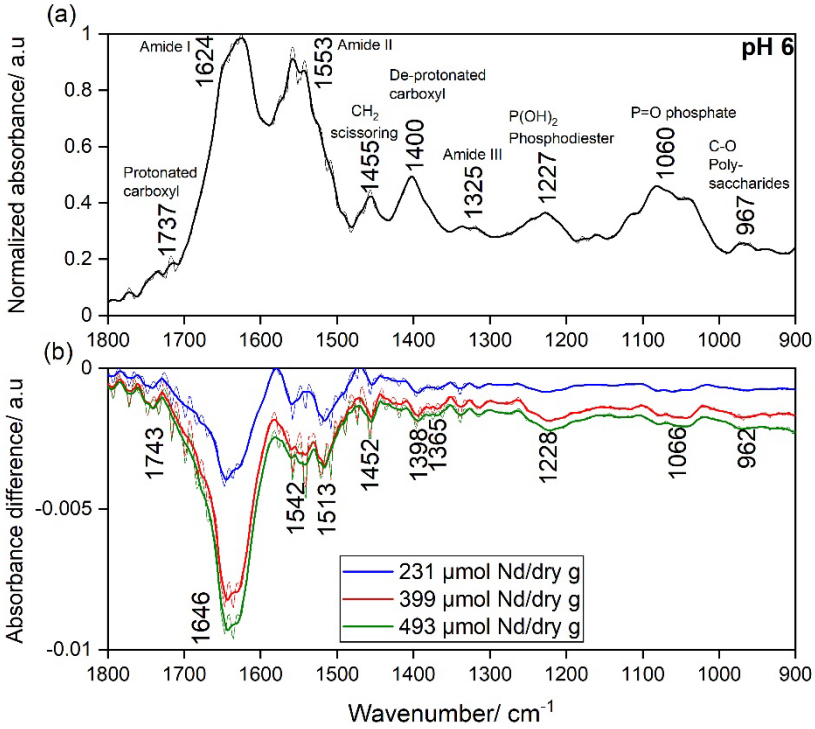

Figure 4.4 (a) Normalized ATR-FTIR spectra of wet cell suspensions of *A. nicotianae* at pH 6.0 and (b) associated difference spectra at varying Nd metal loadings. Thin and thick lines indicate non-smoothed and smoothed ATR-FTIR measurements, respectively.

4.3.2 IR difference spectra highlight important rare earth adsorption mechanisms

Difference spectra were generated by subtracting the ATR-FTIR spectra of control wet cell suspensions at pH 4.0 and 6.0 by spectra of microbes which were loaded with varying concentrations of Nd (Figures 4.3b, 4.4b). At pH 4.0, clear increases in the negative absorbance difference at 1641 and 1540 cm^{-1} peaks were observed at the amide I and II peaks, indicating the participation of carbonyl-based amide adsorption of Nd. Increase in negative absorbance difference at ~1400 cm^{-1} was also observed, indicating carboxyl-based adsorption. A splitting effect at the 1406 cm^{-1} de-protonated carboxyl peak indicated both the decrease of free de-protonated carboxyl sites at 1408 cm^{-1} and the increase in new Nd-carboxyl bonds as identified by the ingrowing 1384 cm^{-1} peak. This splitting phenomenon due to the formation of new metal-surface ligand complexes has also been observed in the FTIR measurements of eggshell biosorption of divalent Pb and Zn ions (Putra et al. 2014) and zeolite coordination of Cu^{+} cations (Zdravkova et al. 2015). Similar splitting effects were observed for phosphodiester and phosphate peaks, strongly suggesting the binding of Nd onto these functional groups. The increased absorbance intensity of the splitting patterns found in the difference spectra at higher surface excess indicated that as more Nd was added to the cell suspension, more Nd-surface ligand complexes were formed. Similar trends were also observed for pH 6.0, though the relative magnitudes were quite different. Unlike the pH 4.0 spectra, IR absorbance results from the pH 6.0 condition were dominated by a stronger absorbance change in the 1646 cm^{-1} amide I peak. On a qualitative level, IR spectra at pH 6.0 could reflect higher adsorption of Nd onto carbonyl-based amide groups compared with pH 4.0. This is consistent with our modeling assumption of the carbonyl-based amide site density function we defined: higher overall Nd surface excess is related to higher densities of $C\text{-}O^{-}$ sites on the bacterial surface.

4.3.3 Acid-base titration modeling of A. nicotianae

Pooled triplicate experiment optimization and individual experiment optimization were first compared (Figure 4.5) to determine the modeling approach that would yield the best convergence in calculated site densities of the relevant functional groups. Although average site density values were within standard deviation error between the two optimization methods, the resulting calculations using a pooled triplicate experiment dataset yielded lower standard deviation error for each investigated site type (Figure 4.5). Thus, the acid-base titration modeling results using the pooled triplicate dataset were used moving forward (Figure 4.6). *A. nicotianae* exhibit high concentrations of phosphodiester, carboxyl, and amine sites (Table 4.1). In comparison with acid-base titration modeling of wild-type *E. coli* discussed in Ch. 2 (Chang et al. 2020a), *A. nicotianae* possess 62.1% more carboxyl groups and 97.0% more phosphate groups per unit mass of dry bacteria. As carboxyl groups are commonly found on the thick peptidoglycan layer of gram-positive bacteria and phosphodiesters are present in large concentrations on the WTAs and LTAs of gram-positive bacteria, this difference between gram-positive and -negative bacteria is expected. As carboxyl and phosphate-based moieties are large contributors to REE adsorption, an increase in both those site types could explain the large adsorption capacity of the *A. nicotianae* cell surface. We note that the phosphate-based ligands can be divided into 70.4% phosphodiester and 29.6% phosphoryl functional groups. These results highlight the importance of accounting for the low pK_a phosphodiester functional group present on the thick peptidoglycan layer and WTA and LTA chains of gram-positive bacteria.

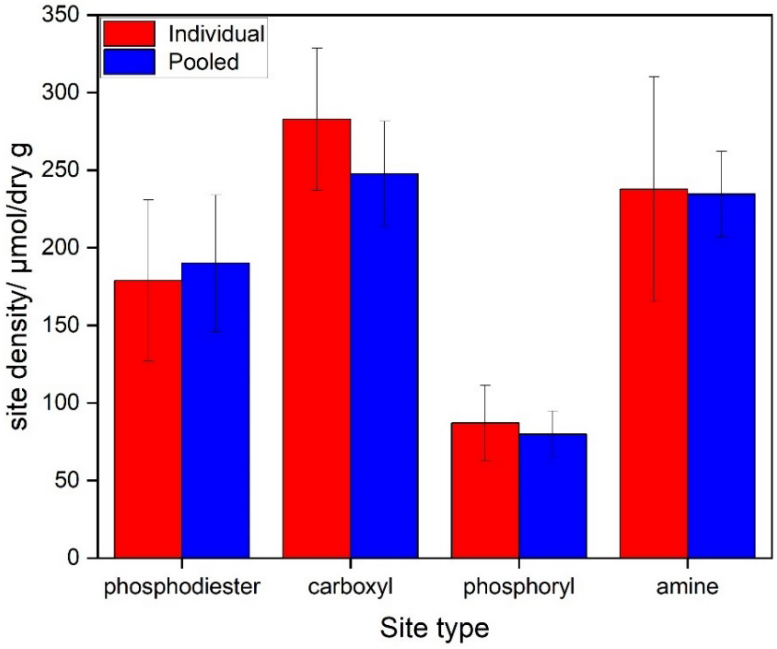

Figure 4.5 Comparison of site densities and associated standard deviation errors for each protonatable site type as modeled using individual triplicate optimization vs. pooled triplicate optimization (described in the methods section 4.2.5)

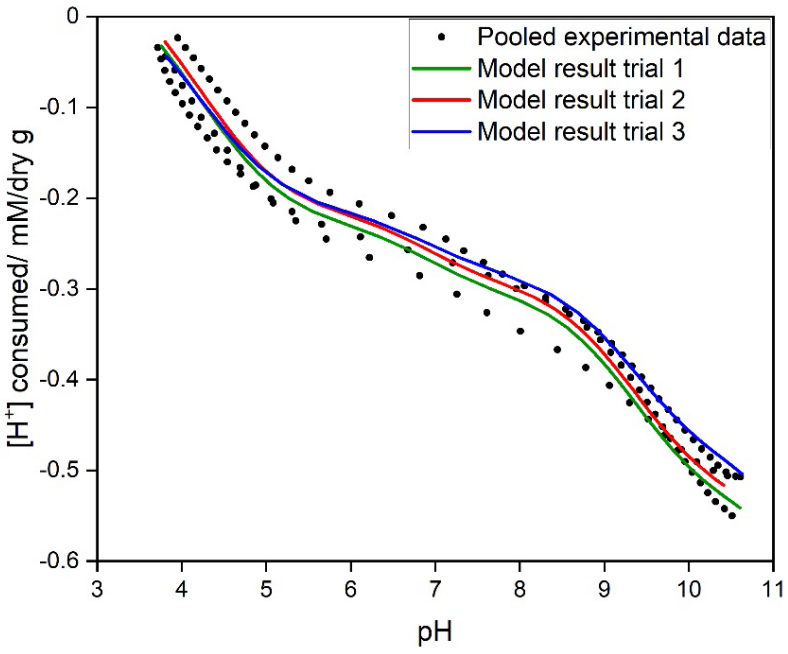

Figure 4.6 Pooled experimental data of acid/base titrations run in triplicate (filled circles) with corresponding 4-protonation site *A. nicotianae* CCMs (colored curves). Site concentrations and pK_a's for the modeling fits are specified in Table 4.1.

The acidity constants for each site type were consistent with those found in literature (Ngwenya, Sutherland, and Kennedy 2003; Borrok, Turner, and Fein 2005; Wightman et al. 2001). Phosphodiesters had a fixed pK_a of 2.1, carboxyl groups had a pK_a of 4.2 ± 0.2, phosphoryl groups had a pK_a of 6.9 ± 0.4, and amine groups had a pK_a of 9.5 ± 0.2 (Table 4.1). Low standard deviations in site densities for carboxyl, phosphoryl, and amine functional groups further confirm that a pseudo-constrained modeling approach that incorporates a fixed pK_a for phosphodiester sites may be a useful method in carrying out acid-base titrations to incorporate all relevant functional groups of the bacterial surface. Unconstrained modeling whereby phosphodiester pK_a was allowed to vary yielded larger standard deviations for site density values and unrealistic pK_a convergences (not shown here).

Table 4.1 Fixed and optimized pK_a and site densities of relevant functional groups present on the gram-positive bacterium, *A. nicotianae*, as determined from acid-base titration modeling. Amide sites with pK_a of 15.1 (Sigel and Martin 1982) would not participate in proton exchange between experimental pH 3.5 and 10.0. It was thus not included in the acid-base titration modeling.

Site type	pK_a	Site density/ µmol/dry g
Phosphodiester	2.1 (fixed)	190 ± 44
Carboxyl	4.2 ± 0.2	248 ± 34
Phosphoryl	6.9 ± 0.4	80 ± 15
Amine	9.5 ± 0.2	234 ± 28
Amide	--	$(2.26 \times 10^{-3}) \times$ *surface excess*

4.3.4 Multi-site surface complexation modeling of A. nicotianae

Data were pooled together using pH 4.0, 5.0, and 6.0 neodymium adsorption isotherms collected from Park et al. (2020) and pH 4.0 and 6.0 neodymium adsorption isotherms conducted in this study. Isotherm conditions of 0.1 M ionic strength and 25 °C temperature was consistent between both sets of pooled data. Experimentally measured surface excess and distribution coefficient values determined in this work were consistent with Park et al. (2020) (Figure 4.7). Increases in pH yielded greater maximum adsorption capacity as well as higher surface selectivity for Nd as presented by pH-dependent increases in both surface excess and distribution coefficients. Optimal adsorption of Nd was determined to be at pH 6.0 under high >300 µM aqueous Nd concentrations. Modeled Nd-stability constants (Table 4.2) indicate high affinity site types mostly in the form of phosphate-based ligands. Both 1:1 phosphodiester and phosphoryl-Nd surface complexation reactions have high $\log_{10}K$ binding constants of 6.32 ± 0.07 and 6.69 ± 0.08, respectively (Table 4.2). The deconvolution of phosphate groups as phosphodiester and

phosphoryl moieties with pK_as of 2.1 and 6.9, respectively, presents a significant difference from most previous surface complexation models of bacterial surfaces, which invoke only a phosphoryl site type (Markai et al. 2003; Ngwenya et al. 2009; Guiné et al. 2006). We note that this new phosphodiester adsorption mechanism is invoked specifically for gram-positive bacteria due to the large presence of peptidoglycan-anchored wall teichoic acids and bilipid plasma membrane-anchored lipoteichoic acids (Brown, Santa Maria, and Walker 2013). The phosphate-Nd binding constants reported in this study are significantly lower than the Nd-phosphate $\log_{10}K$ values of 8.14 ± 0.5 and 8.50 ± 0.05 reported by Markai et al. (2003) and Ngwenya et al. (2009), respectively. This can be partially explained by the differences in phosphate site concentrations imposed by both studies. While Markai et al. (2003) reports a phosphoryl site density of 51.3 ± 19.4 µmol/dry g, Ngwenya et al. (2009) uses a value of 220 ± 60 µmol/dry g. The present study reports a phosphoryl site density of 80 ± 15 µmol/dry g, which is close to within error of the value of 51.3± 19.4 µmol/dry g reported in Markai et al. (2003). However, despite similar phosphoryl site densities being reported from acid-base titration modeling, the present study invokes additional multi-site reactions that allow for simultaneous competitive adsorption of neodymium onto a variety of surface site ligands. Multi-site surface complexation is supported by EXAFS and TRLFS studies (Markai et al. 2003; Takahashi et al. 2010b) and should thus be considered in the implementation of thermodynamic surface models.

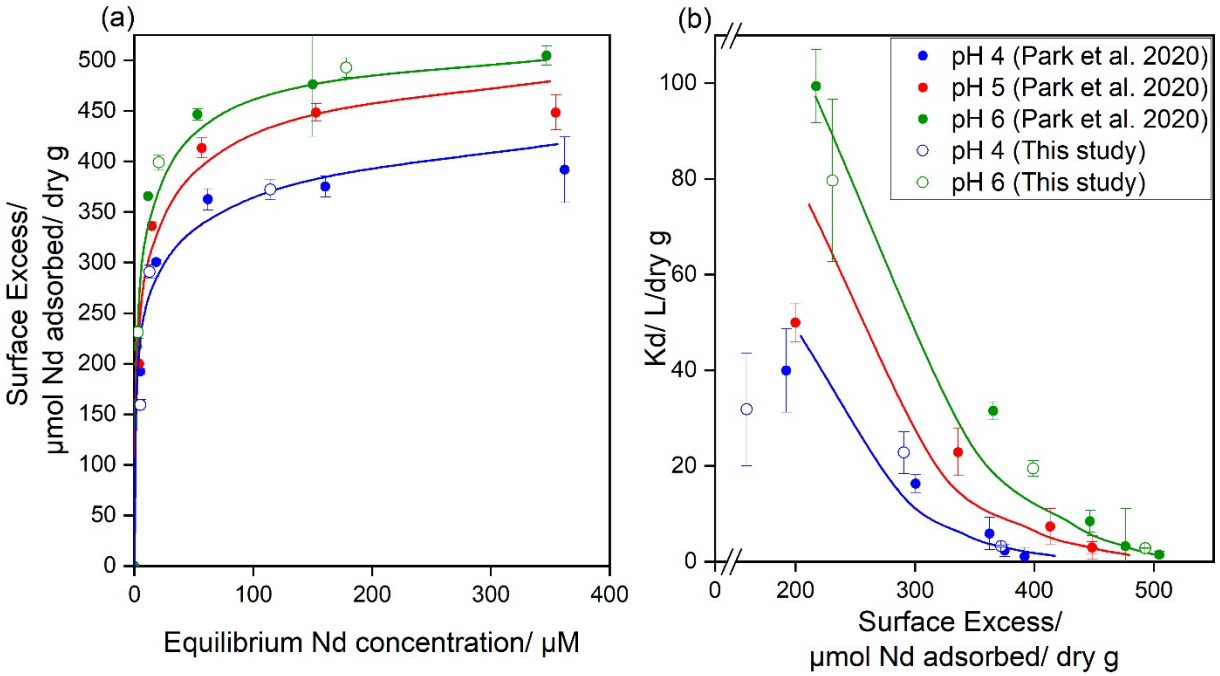

Figure 4.7 Pooled (a) surface excess and (b) distribution coefficient data of neodymium adsorption isotherms from Park et al. (2020) (filled circles) and results from this study (open circles). Modeling results (colored lines) correspond with a 4-site constant capacitance model incorporating adsorption via phosphodiester, carboxyl, phosphoryl, and carbonyl-based amide functional groups. Site-based Nd stability constants are reported in Table 4.2.

Neodymium-carboxyl adsorption was modeled as having a much lower $\log_{10}K = 4.65 \pm 0.75$ binding constant compared with the phosphate-based ligands' Nd stability constants. Notably, this calculated 4.65 ± 0.75 carboxyl stability constant was similar to the 4.76 Nd-carboxyl binding constant determined by Chang et al. (2020b)'s linear free energy relationship discussed in Chapter 3. This low Nd stability constant is consistent with other biosorption studies that indicate that carboxyl-based surface ligands on bacterial surfaces are abundant, non-selective site types with relatively low metal stability constants (Fein et al. 1997; Daughney and Fein 1998; Chang et al. 2020a).

In contrast, I report a high Nd $\log_{10}K$ of 6.41 ± 0.23 for carbonyl-based amides (Table 4.2), similar to the values determined in this study for phosphate-based Nd adsorption. This high stability constant can be explained by the strong Lewis acid nature of trivalent neodymium and the ability for a large concentration of neutrally charged C=O linked amides to form $C\text{-}O^-$ sites from the resonance-induced delocalization of pi-bond electrons. This mechanism is qualitatively supported by our ATR-FTIR difference spectra, whereby large absorbance changes in the carbonyl-based amide I peak are observed when the bacteria is loaded with increasing amounts of neodymium. This resonance-based adsorption mechanism implies the presence of a potentially high selectivity site type for lanthanide surface complexation. Because ion-amide complexes increase in strength with higher ionic potential cations (Feng, Schmidt, and Weiss 1996), trivalent lanthanides pose the strongest control over the complexation of these site types in comparison with other co-occurring divalent metals, such as Zn^{2+} and Cd^{2+}, present in soils.

4.3.5 Relative surface site contributions in the adsorption of Nd onto A. nicotianae

Surface complexation models pose significant advantages over empirically derived Langmuir and Freundlich-type models. In addition to the incorporation of thermodynamic stability constants and more mechanistic adsorption modeling in the form of electrostatic surface treatment and bulk solution aqueous speciation, surface complexation modeling can also help elucidate the competition of varying site types in a bulk adsorption process. Fitting and modeling of batch adsorption isotherm data in this study (Figure 4.7) present one possible solution in multi-site competitive surface complexation of the moieties found on the complex *A. nicotianae* bacterial surface. Although acidity constants and titration-fitted site densities help constrain the optimization of Nd-carboxyl, phosphodiester, phosphoryl, and amide stability constants, surface complexation models may still be limited due to modeling having multiple possible, non-unique solutions. To this extent, ATR-FTIR analyses in this work help apply qualitative constraints in the SCM approach.

Table 4.2 Optimized Nd-surface ligand stability constants and invoked binding stoichiometries for relevant functional groups present on the gram-positive bacteria, *A. nicotianae*.

Site type	Site density/ µmol/dry g	Nd binding stoichiometry invoked in model (Ligand:Nd)	Nd-site $\log_{10}K$ stability constant
Phosphodiester	190 ± 44	1:1	6.32 ± 0.07
Carboxyl	248 ± 34	2:1	4.65 ± 0.75
Phosphoryl	80 ± 15	1:1	6.69 ± 0.08
Amine	234 ± 28	--	--
Amide	$(2.26 \times 10^{-3}) \times$ *surface excess*	1:1	6.41 ± 0.23

Site-specific surface excess results from our surface complexation model highlight the large contributions of phosphodiester and amide-based functional groups in the uptake of Nd. (Figure 4.8). This is corroborated by our IR difference spectra at pH 4, where amide I and II and phosphodiester peaks are shown to be most affected by increases in metal loading (Figure 4.3b). Modeled carboxyl and phosphoryl adsorption at pH 4.0 is shown to contribute much less to the Nd adsorption budget in comparison with amide and phosphodiester groups. This is also observed in the pH 4.0 IR spectra, where carboxyl peak changes are much less intense than changes occurring at the amide and phosphodiester peaks. As pH increases from pH 4.0 to pH 5.0, total surface excess also increases. The higher total surface excess can be attributed to an increase in adsorption due to carboxyl and phosphoryl sites (Figure 4.8). At higher loadings, both carboxyl and phosphoryl sites begin to increase in contribution to the overall Nd adsorption budget. With pK_as of 4.2 and 6.9, carboxyl and phosphoryl functional groups begin to deprotonate with a change in pH from 4.0 to 5.0. The increase in anionic site concentrations enhances the surface's ability to complex trivalent Nd ions. With a further increase in pH from 5.0 to 6.0, carboxyl sites begin to saturate at high Nd loadings, leaving the Nd adsorption to be influenced more by phosphoryl sites. Surface complexation modeling thus suggests the saturation of site types with increasing Nd loading between pH 4.0 and 6.0 to be in the following order: phosphodiester ≥ amide > carboxyl > phosphoryl. IR difference spectra (Figures 4.3b, 4.4b) qualitatively corroborate this trend. At lower Nd surface excess, changes in IR absorbance are mostly present in amide I and II and phosphodiester peaks. In particular, at pH 4.0, higher Nd surface excess causes IR absorbance changes in the carboxyl peaks with minimal changes in amide peaks (Figure 4.3b). This further suggests that at higher loadings, amide sites become saturated, allowing for lower affinity site types such as carboxyl groups to then influence the overall Nd adsorption process.

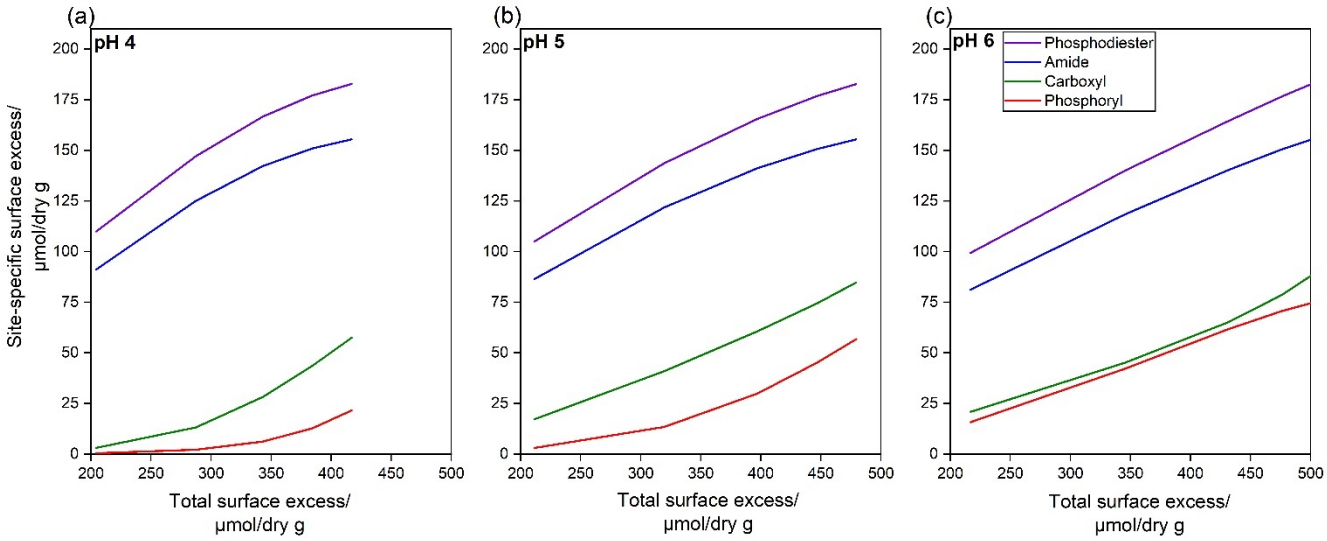

Figure 4.8 Site-specific Nd surface excess modeling results from optimizing phosphodiester, carboxyl, phosphoryl, and carbonyl-based amide surface complexation stability constants at (a) pH 4.0, (b) 5.0, and (c) 6.0. Binding mode and strength of each reaction is reported in Table 4.2.

4.4 Conclusions

Significant progress has been made in the recent two decades from spectroscopic and batch adsorption edge and isotherm studies to describe REE adsorption onto bacterial surfaces (Texier et al. 2000; Andrès, Le Cloirec, and Texier 2003; Markai et al. 2003; Ngwenya et al. 2009; Takahashi et al. 2010b; Bonificio and Clarke 2016). In comparison, surface complexation modeling of this process has made less progress by misrepresenting the cell surface with simplified one- or two-site surface models. As this study shows, phosphodiester and carbonyl-based amide sites contribute to the high neodymium adsorption capacity of *A. nicotianae*. Previous surface complexation models of gram-positive bacteria that lack these sites in lieu of incorporating only carboxyl and phosphoryl sites dramatically simplify and misrepresent the true cell surface adsorption chemistry. This study attempts to clarify the multi-site complexation nature of Nd adsorption onto the gram-positive bacterium, *A. nicotianae*. In contrast to prior work, our modeling and IR difference spectra suggests amide and phosphodiester sites strongly influence bulk adsorption at low metal loadings between pH 4.0 and 6.0. At higher metal loadings >500 µmol/dry g, it is likely that carboxyl and phosphoryl sites could also participate in contributing to the Nd adsorption budget due to amide and phosphodiester site saturation.

Future research directions for this work include quantitative ATR-FTIR analysis whereby integration of functional group peaks could further elucidate the multi-site competitive surface complexation reactions taking place. Challenges for this particular advancement include peak deconvolution methods, particularly at carboxyl and phosphodiester peaks that split due to the formation of new Nd-surface ligand complexes. In addition, future work should include a deeper investigation of carbonyl-based amide adsorption via bacterial surfaces: (1) do these sites exist commonly on other soil microbial surfaces? (2) are there variations in amide site concentrations across gram-negative and gram-positive strains? (3) how does the presence of amides affect

microbial surface selectivity of lanthanides in the presence of co-occurring divalent metals with lower ionic potential? These questions all point towards a necessity to further study and understand how naturally occurring soil bacteria can play a role in the transport of cation metals found in surface and subsurface environments. This study presents a new step towards better characterizing gram-positive soil bacteria through a novel four-site surface complexation modeling approach that incorporates amide- and phosphodiester-Nd reactions for the first known time in the bacterial surface biosorption of lanthanides.

CHAPTER 5

Concluding remarks: Bacterial surfaces teach us important lessons in soil contaminant transport and selective metal extraction

5.1 Engineered bacterial surfaces in unconventional extraction projects

This dissertation highlights the complexity of bacterial surface interactions with REEs. Through a combination of multi-site surface complexation modeling and experiments, this dissertation provides more accurate ways of characterizing how bacterial surface processes impact bulk water solution chemistry.

As discussed in Chapters 2 and 3 of this dissertation, genetically engineered bacterial surfaces can provide a sustainable unconventional means of extracting and separating REEs from other co-occurring metals. One promising application of this technology is the extraction and recycling of REEs from electronic waste, geothermal fluids, or coal fly-ash leachates (A. Brewer et al. 2019). By using fixed-bed columns packed with dLBTx8 induced *E. coli*, Brewer et al. have separated precious rare earths such as neodymium from other metals such as nickel and zinc found in end-of-life NdFeB magnet scraps of mobile device speakers (Brewer et al., 2019a). Because the LBT sites present on the engineered *E. coli* cell surface preferentially adsorb and chelate REEs over divalent metals, targeting low-grade environmental feedstocks can also be advantageous. To this extent, scientists have recently demonstrated the disproportionate cell surface binding of rare earths in the presence of co-existing heavy metals found in Lower Radical, Togo, and Round Top Mountain mine leachates (Park et al., 2017).

Future research directions for the engineering application of bacterial surface-based extraction methods should include studying the scalability of this technology, as well as introducing highly selective surface sites onto inorganic substrates. While Ch. 3 discusses the successful scaling of a fixed-bed column from 5 cm to 100 cm, the 20-fold increase is induced in the length (y-axis) of the column. Changes in the radius of the column will likely have consequences in how effectively one-dimensional reactive transport modeling can be implemented. At higher column radii, 3-dimensional transport modeling will likely need to be incorporated by adding additional x- and z-based axes for both interbead advective and intrabead diffusive flow. Additional research should also be conducted on modeling temperature change effects on surface ligand-metal stability constants. One preliminary step may include using Van't Hoff plots to establish relationships between metal-bacterial surface binding constants and temperature (Brewer et al., 2019). Instead of using fixed metal stability constants as is done in most surface complexation models today, temperature-based functions can be derived to establish temperature-dependent metal stability constants for bacterial surface ligands. This will ultimately improve the flexibility and applicability of reactive transport modeling of fixed-bed columns because temperature optimization can have large chemical engineering implications on the efficacy of bioreactor-based metal extraction. Lastly, a life cycle assessment and financial cost analysis should also be conducted to assess the feasibility of these novel technologies.

The investigation of the aforementioned topics presents an exciting new frontier for the selective extraction of precious metals using complex multi-site surfaces. Engineering of bacteria-based surface chemistry provides a useful case study for future efforts to create selective metal separation on novel engineered substrates. Furthermore, as is discussed in Ch. 4, resonance of carbonyl-based amide sites allows for especially selective metal interactions whereby high ionic

potential metal cations form particularly stable surface complexes in comparison with less charge-dense cations. Unique electrostatic interactions such as these illustrate the many important lessons that can be learned from studying naturally occurring soil bacteria, such as *A. nicotianae*. The transformation of an inert neutrally-charged C=O carbonyl site into a strongly binding $C\text{-}O^-$ carbonyl-based amide site poses new and exciting questions regarding how we can exploit the large differences in ionic potential between REEs and alkaline earth metals in order to produce more valuable, higher-grade REE extractants.

5.2 Soil bacterial surfaces in subsurface geochemical processes

In Ch. 4, I discuss the involvement of multiple organic acid functional groups in the form of carboxyl, phosphate, and carbonyl-based amide adsorption mechanisms present on the surface of a gram-positive soil bacterium, *A. nicotianae*. Importantly, many of these functional groups are de-protonated and readily available for favorable electrostatic interactions with positively charged metals found in the environment at naturally occurring soil pH values ranging from of 4.0 to 6.0. High affinity bacteria-REE interactions are particularly relevant at low concentration metal regimes, where REEs may control subsurface heavy metal fate and transport (Fein, Martin, and Wightman 2001). As bioaccumulation of uranium is controlled largely by phosphate cell surface moieties (polysaccharides and teichoic acids) (Panak et al. 2000), bacterial surface interactions with REEs can also impact nuclear waste radionuclide migration. In addition, REEs have in the past been used as tracers for pedogenesis and soil fractionation (Laveuf, Cornu, and Juillot 2008; Vázquez-Ortega et al. 2015). As REE tracing can provide spatial and temporal insights into erosion processes not possible using traditional methods (Zhang et al. 2003), understanding bacterial cell surface-rare earth metal binding in soil sediments may also provide useful additional information in the characterization of soil erosion dynamics.

Future research directions should include investigating the flexibility and applicability of surface complexation models in multi-component soil systems that contain pore solution, mineral surface, and bacterial surface interfaces (Fein 2006). Using linear free energy relationships to describe carboxyl-metal adsorption binding is a particularly effective strategy for studying gram-negative soil bacteria. Similar relationships should be developed for phosphodiester- and phosphoryl-based REE adsorption binding to elucidate gram-positive soil bacteria metal interactions. The surface complexation models presented in this work are limited by the electrostatic constant capacitance model invoked due to assumptions of inner-sphere complexation mechanism and a linear surface charge-potential relationship (Sposito 2016). The improvement and fine tuning of other models such as the charge distribution-multisite complexation model (CD-MUSIC) may help the applicability and flexibility of surface complexation models. However, current challenges scientists face include the presence of too many unconstrained variables, such as optimizable protonation constant and site densities for each site type as well as electrostatic terms such as capacitance/surface potential values. Furthermore, the implementation of these models become limited under high ionic strength (>1 μM) conditions, where the thickness of the Stern layer and the activity coefficients for adsorbates may come into question. While this dissertation provides one way of characterizing bacterial surface-metal adsorption using the constant capacitance model simplification, improved descriptions of electrical double layer structure and chemistry (in particular the dielectric properties) are required to predict adsorption behavior on highly charged surfaces.

SUPPORTING INFORMATION

Supporting Information 2.1

Useful estimates:

- 140 m^2/dry gram surface area
- 100,000 OmpA per *E. coli* cell
- 6,280,000 nm^2 (6.28 μm^2) surface area per *E. coli* cell
- A dLBTx8 strain refers to 16 lanthanide binding tags on each OmpA
    - (d stands for double; 2 x 8 tags = 16 tags per OmpA).

Calculations:

$$100{,}000\ \frac{\text{OmpA}}{\text{cell}} \times \frac{1}{6{,}280{,}000}\frac{\text{cell}}{\text{nm}^2} \times\ 16\ \frac{\text{lanthanide binding tags}}{\text{OmpA}} = 0.255\ \frac{LBT\ sites}{nm^2}$$

$$0.255\ \frac{\text{LBT sites}}{\text{nm}^2} \times\ 140\ \frac{\text{m}^2}{\text{dry gram}} \times\ 10^{18}\frac{\text{nm}^2}{\text{m}^2} \times \frac{1}{6.02 \times 10^{23}}\frac{\text{mole}}{\text{sites}}$$
$$= \mathbf{5.93 \times 10^{-5}}\frac{\textbf{moles of LBTs}}{\textbf{dry gram bacteria}}$$

Supporting Information 3.1

Batch adsorption experiments

50 mM Nd stock solution was prepared by dissolving $NdCl_3$ (Sigma Aldrich) in 1 mM HCl. Nd solutions for batch adsorption work were prepared by subsequent dilutions in 10 mM, pH 6 MES solution. Batch adsorption capacity experiments were conducted with 0.05 wet grams of microbe beads exposed to a range of Nd concentrations in 5 mL total volume. Nd concentrations were measured colorimetrically using Arsenazo III and subtracted from the initial Nd concentration to determine the total adsorbed Nd.

Supporting Information 3.2

Arsenazo III assay for Nd quantification

We colorimetrically determined Nd concentrations using Arsenazo III for Nd batch experiments and breakthrough curve effluents (no other rare earth elements were present in these experiments). Each sample was mixed with filtered 0.1% Arsenazo III and the absorbance at 625 nm wavelength was measured and compared to Nd standards to determine Nd concentrations in

each sample. A more detailed procedure may be found in Brewer et al. (2019).(Aaron Brewer et al. 2019)

Supporting Information 3.3

Surface complexation modeling of batch Nd adsorption isotherms

The model predictions for Nd adsorption as a function of metal loading compared well to experimental Nd batch adsorption isotherm data (Figure SI-1). The modeled surface excess (µmol Nd sorbed/dry g bacteria) was within ± 1 standard deviation of the experimental results. While the surface excess in Figure SI-1a informs us of maximum sorption capacity, the distribution coefficient ($K_d = \frac{\text{surface excess}}{\text{equilibrium Nd in solution}}$) informs us of the surface's sorption affinity (Figure SI-1b). At low surface excess <100 µmol Nd/dry g, the model slightly overpredicts K_d. However, at higher surface excess >150 µmol Nd/dry g, the model fit improves. Given that we are using Nd-carboxyl and Nd-LBT stability constants as estimated by literature, we conclude that these thermodynamic estimates are useful in successfully predicting Nd adsorption to the engineered surface of dLBTx8 *E. coli* cells.

Supporting Information 3.4

Calibrating physical parameters for 1-D reactive transport modeling of Nd

In our dual porosity model of Nd adsorption to a packed 20 x 0.5 cm column, we calibrated dispersivity and intraparticle diffusion coefficient by allowing those variables to be optimized to best fit the experimental breakthrough curve (main manuscript Ch. 3-Figure 3.3). We report a dispersion coefficient of 2.22×10^{-8} m^2/s, which is comparable to the axial dispersion coefficients of 1.09 to 1.11×10^{-8} m^2/s as determined by Zhou et al. (2013)(Zhou et al. 2013) for a series of organic molecules passing through a microporous resin. Park and Tavlarides (2010)(H. J. Park and Tavlarides 2010) also report a dispersion coefficient of 2.27×10^{-9} m^2/s for Nd transport through a phosphorous based sol-gel adsorbent. Despite not conducting tracer experiments, our model's optimized dispersion coefficient falls within a reasonable range as compared with other literature values. Intraparticle diffusion coefficient was also optimized and determined to be 1.31×10^{-12} m^2/s, which is slightly different from the 6.83×10^{-13} m^2/s intraparticle diffusion coefficient reported by Brewer et al. (2019) for the same system using an empirically based Bohart-Adams model. Our optimized value is comparable to D'Angelo and Panzer (2017)'s intraparticle diffusion coefficient of 1.01×10^{-12} m^2/s for lithium ion transport in a PEGDA polymer. We present good calibration fit to the experimental data as shown Main Manuscript Ch. 3-Figure 3.3, and both optimized dispersivity and intraparticle diffusion coefficient terms were justified by comparison with other literature values.

Supporting Information 3.5

1-D reactive transport modeling of Nd under varying conditions

REE-containing feedstocks such as geothermal fluids and mining leachates have a large range of rare earth concentrations, and the dominant REE-complexing surface sites vary dramatically with aqueous concentration (Chang et al. 2020a). Thus, we investigated the ability of our model to accurately predict Nd breakthrough curves with varying inlet concentrations. Furthermore, we tested our model's ability to adjust to a change in column length – we used a packed 15 cm column with the same 23 dry g/L cell suspension density rather than the packed 20 cm column used for calibrating the model. As expected, the higher 500 and 1500 µM Nd inlet concentration feedstocks had a significantly earlier breakthrough time than the 50 µM Nd inlet solution (main manuscript Ch. 3-Figure 3.3). Furthermore, the spread of the 50 µM Nd inlet solution breakthrough curve is much more pronounced compared to the slopes of the 500 and 1500 µM Nd inlet solutions. We attribute this to a dominance in the hydrodynamic dispersion term (second term of main manuscript Ch. 3, equation 14) when lower concentration gradients are used (first term of main manuscript Ch. 3, equation 14). Our model-projected breakthrough curves compared well with experimentally generated data (main manuscript-Figure 3.3), suggesting good calibration of our model with appropriate intraparticle diffusion and hydrodynamic dispersion coefficients.

Figure SI-1 Model and experimental results comparison for (a) batch Nd sorption isotherm and (b) distribution coefficient vs surface excess data. Error bars indicate standard deviations obtained from triplicate experiments.

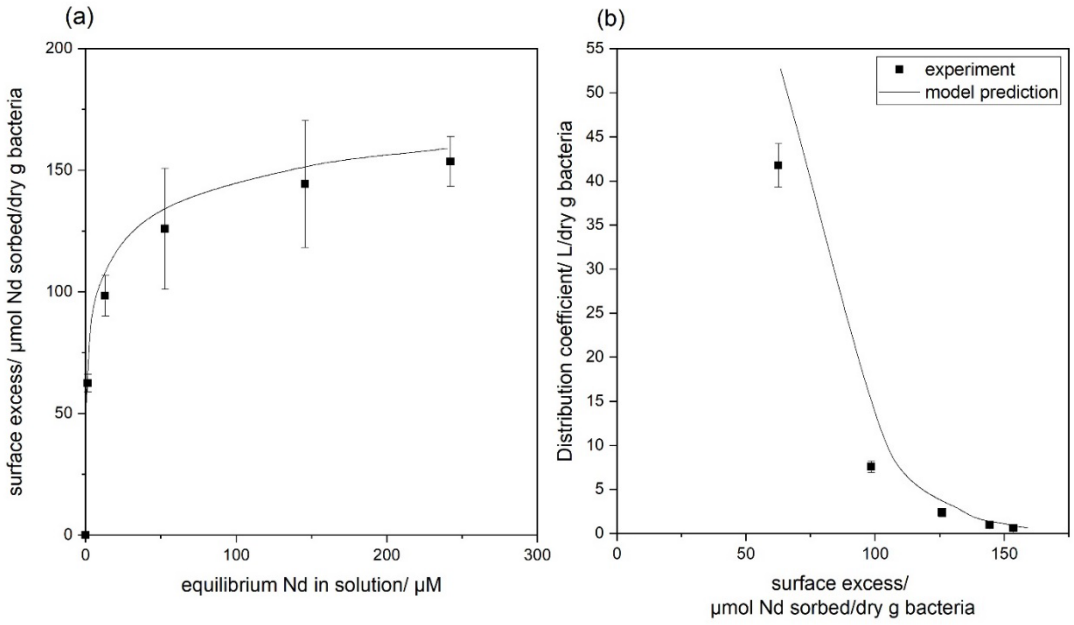

Supporting Information References

1. Brewer, A. *et al.* Microbe Encapsulation for Selective Rare-Earth Recovery from Electronic Waste Leachates. *Environ. Sci. Technol.* **53**, acs.est.9b04608 (2019).

2. Zhou, J. *et al.* Modeling of breakthrough curves of single and quaternary mixtures of ethanol, glucose, glycerol and acetic acid adsorption onto a microporous hyper-cross-linked resin. *Bioresour. Technol.* **143**, 360–368 (2013).

3. Park, H. J. & Tavlarides, L. L. Adsorption of neodymium(III) from aqueous solutions using a phosphorus functionalized adsorbent. *Ind. Eng. Chem. Res.* **49**, 12567–12575 (2010).

4. D'Angelo, A. J. & Panzer, M. J. Enhanced Lithium Ion Transport in Poly(ethylene glycol) Diacrylate-Supported Solvate Ionogel Electrolytes via Chemically Cross-linked Ethylene Oxide Pathways. *J. Phys. Chem. B* **121**, 890–895 (2017).

5. Chang, E., Brewer, A. W., Park, D. M., Jiao, Y. & Lammers, L. N. Surface complexation model of rare earth element adsorption onto bacterial surfaces with lanthanide binding tags. *Appl. Geochemistry* **112**, 104478 (2020).

REFERENCES

Ahmed, E, and S J M Holmström. 2014. “Minireview Siderophores in Environmental Research : Roles and Applications.” *Microbial Biotechnology* 7 (3). https://doi.org/10.1111/1751-7915.12117.

Alonso, Elisa, Andrew M. Sherman, Timothy J. Wallington, Mark P. Everson, Frank R. Field, Richard Roth, and Randolph E. Kirchain. 2012. “Evaluating Rare Earth Element Availability: A Case with Revolutionary Demand from Clean Technologies.” *Environmental Science and Technology* 46 (6): 3406–14. https://doi.org/10.1021/es203518d.

Andrès, Y., P. Le Cloirec, and A. C. Texier. 2003. “Rare Earth Elements Removal by Microbial Biosorption: A Review.” *Environmental Technology (United Kingdom)* 24 (11): 1367–75. https://doi.org/10.1080/09593330309385681.

Bakken, Lars R., and Rolf A. Olsen. 1987. “The Relationship between Cell Size and Viability of Soil Bacteria.” *Microbial Ecology* 13 (2): 103–14. https://doi.org/10.1007/BF02011247.

Bank, T.; Roth, E.; Tinker, P.; Granite, E. 2016. “Analysis of Rare Earth Elements in Geologic Samples Using Inductively Coupled Plasma Mass Spectrometry.” *US DOE Topical Report - DOE/NETL-2016/1794*, 10.

Bayer, M. E., and M. H. Bayer. 1991. “Lanthanide Accumulation in the Periplasmic Space of Escherichia Coli B.” *Journal of Bacteriology* 173 (1): 141–49. https://doi.org/10.1128/jb.173.1.141-149.1991.

Beinum, Wendy Van, Johannes C.L. Meeussen, Anthony C. Edwards, and Willem H. Van Riemsdijk. 2000. “Transport of Ions in Physically Heterogeneous Systems; Convection and Diffusion in a Column Filled with Alginate Gel Beads, Predicted by a Two- Region Model.” *Water Research* 34 (7): 2043–50. https://doi.org/10.1016/S0043-1354(99)00371-1.

Beveridge, T. J., and W. S. Fyfe. 1985. “Metal Fixation by Bacterial Cell Walls.” *Canadian Journal of Earth Sciences* 22 (12): 1893–98. https://doi.org/10.1139/e85-204.

Bonificio, William D., and David R. Clarke. 2016. “Rare-Earth Separation Using Bacteria.” *Environmental Science and Technology Letters* 3 (4): 180–84. https://doi.org/10.1021/acs.estlett.6b00064.

Borrok, David, Jeremy B. Fein, and Charles F. Kulpa. 2004. “Proton and Cd Adsorption onto Natural Bacterial Consortia: Testing Universal Adsorption Behavior.” *Geochimica et Cosmochimica Acta* 68 (15): 3231–38. https://doi.org/10.1016/j.gca.2004.02.003.

Borrok, David, Benjamin F. Turner, and Jeremy B. Fein. 2005. “A Universal Surface Complexation Framework for Modeling Proton Binding onto Bacterial Surfaces in Geologic Settings.” *American Journal of Science* 305 (6-8 SPEC. ISS.): 826–53. https://doi.org/10.2475/ajs.305.6-8.826.

Brewer, A., E. Chang, D.M. Park, T. Kou, Y. Li, L.N. Lammers, and Y. Jiao. 2019. “Recovery of Rare Earth Elements from Geothermal Fluids through Bacterial Cell Surface Adsorption.” *Environmental Science and Technology* 53 (13). https://doi.org/10.1021/acs.est.9b00301.

Brewer, Aaron, Alice Dohnalkova, Vaithiyalingam Shutthanandan, Libor Kovarik, Elliot Chang, April M. Sawvel, Harris E. Mason, et al. 2019. “Microbe Encapsulation for Selective Rare-Earth Recovery from Electronic Waste Leachates.” Research-article. *Environmental Science & Technology* 53: acs.est.9b04608. https://doi.org/10.1021/acs.est.9b04608.

Brown, Stephanie, John P. Santa Maria, and Suzanne Walker. 2013. “Wall Teichoic Acids of Gram-Positive Bacteria.” *Annual Review of Microbiology* 67: 313–36. https://doi.org/10.1146/annurev-micro-092412-155620.

Bruker Optics. 2011. “Application Note AN # 79 Attenuated Total Reflection (ATR) – a Versatile Tool for FT-IR Spectroscopy Refractive Index.” https://www.bruker.com/fileadmin/user_upload/8-PDF-Docs/OpticalSpectrospcopy/FT-IR/ALPHA/AN/AN79_ATR-Basics_EN.pdf.

Butzen, Margaret L., and Jeremy B. Fein. 2019. “Influence of Extracellular Polymeric Substances on the Adsorption of Cadmium onto Three Bacterial Species.” *Geomicrobiology Journal* 36 (5): 412–22. https://doi.org/10.1080/01490451.2018.1564804.

Castro, Felipe D., Jacqueline Sedman, Ashraf A. Ismail, Bahareh Asadishad, and Nathalie Tufenkji. 2010. “Effect of Dissolved Oxygen on Two Bacterial Pathogens Examined Using ATR-FTIR Spectroscopy, Microelectrophoresis, and Potentiometric Titration.” *Environmental Science and Technology* 44 (11): 4136–41. https://doi.org/10.1021/es903692u.

Cavalier-Smith, Thomas, Martin Brasier, and T. Martin Embley. 2006. “Introduction: How and When Did Microbes Change the World?” *Philosophical Transactions of the Royal Society B: Biological Sciences* 361 (1470): 845–50. https://doi.org/10.1098/rstb.2006.1847.

Chakhmouradian, Anton R. 1996. “On the Development of Niobium and Rare-Earth Minerals in Monticellite - Calcite Carbonatite of the Oka Complex, Quebec.” *Canadian Mineralogist* 34 (2): 479–84.

Chang, Elliot, Aaron W. Brewer, Dan M. Park, Yongqin Jiao, and Laura N. Lammers. 2020a. “Surface Complexation Model of Rare Earth Element Adsorption onto Bacterial Surfaces with Lanthanide Binding Tags.” *Applied Geochemistry* 112 (May 2019): 104478. https://doi.org/10.1016/j.apgeochem.2019.104478.

Chang, Elliot, Aaron W Brewer, Dan M Park, Yongqin Jiao, and Laura N Lammers. 2020b. “Selective Biosorption of Valuable Rare Earth Elements Among Co-Occurring Lanthanides.” *Environmental Engineering Science* 00 (00): 1–11. https://doi.org/10.1089/ees.2020.0291.

Coelho, Clívia D., Agnes Caroline S. Faria, and Eduardo Antonio G. Marques. 2017. “Comparative Analysis of Different Boundary Conditions and Their Influence on Numerical Hydrogeological Modeling of Palmital Watershed, Southeast Brazil.” *Journal of Hydrology: Regional Studies* 12 (December 2016): 210–19. https://doi.org/10.1016/j.ejrh.2017.05.006.

Condamines, N., and C. Musikas. 1992. *The Extraction by n, n-Dialk Ylamides. II. Extraction of Actinide Cations*. *Solvent Extraction and Ion Exchange*. Vol. 10. https://doi.org/10.1080/07366299208918093.

Cotton, Simon. 2006. *Lanthanide and Actinide Chemistry*. *Lanthanide and Actinide Chemistry*. https://doi.org/10.1002/0470010088.

Cui, Haixia, Jianmin Chen, Huidi Zhou, and Yanhua Lu. 2007. "Synthesis and Infrared and Fluorescent Spectra of Rare Earth Complexes with a New Amide Ligand." *Spectrochimica Acta - Part A: Molecular and Biomolecular Spectroscopy* 68 (3): 478–83. https://doi.org/10.1016/j.saa.2006.12.060.

D'Angelo, Anthony J., and Matthew J. Panzer. 2017. "Enhanced Lithium Ion Transport in Poly(Ethylene Glycol) Diacrylate-Supported Solvate Ionogel Electrolytes via Chemically Cross-Linked Ethylene Oxide Pathways." *Journal of Physical Chemistry B* 121 (4): 890–95. https://doi.org/10.1021/acs.jpcb.6b10125.

Daughney, Christopher J., and Jeremy B. Fein. 1998. "The Effect of Ionic Strength on the Adsorption of H+, Cd2+, Pb2+ and Cu2+ by Bacillus Subtilis and Bacillus Licheniformis: A Surface Complexation Model." *Journal of Colloid and Interface Science* 198 (1): 53–77. https://doi.org/10.1006/jcis.1997.5266.

Deflores, Lauren P., Ziad Ganim, Rebecca A. Nicodemus, and Andrei Tokmakoff. 2009. "Amide I′-II′ 2D IR Spectroscopy Provides Enhanced Protein Secondary Structural Sensitivity." *Journal of the American Chemical Society* 131 (9): 3385–91. https://doi.org/10.1021/ja8094922.

Dent, Peter C. 2012. "Rare Earth Elements and Permanent Magnets (Invited)." *Journal of Applied Physics* 111 (7): 1–6. https://doi.org/10.1063/1.3676616.

Dodson, Jennifer R., Helen L. Parker, Andrea Muñoz García, Alexandra Hicken, Kaana Asemave, Thomas J. Farmer, He He, James H. Clark, and Andrew J. Hunt. 2015. "Bio-Derived Materials as a Green Route for Precious & Critical Metal Recovery and Re-Use." *Green Chemistry* 17 (4): 1951–65. https://doi.org/10.1039/c4gc02483d.

Du, Xiaoyue, and T. E. Graedel. 2011. "Global In-Use Stocks of the Rare Earth Elements: A First Estimate." *Environmental Science and Technology* 45 (9): 4096–4101. https://doi.org/10.1021/es102836s.

Edington, Sean C., Andrea Gonzalez, Thomas R. Middendorf, D. Brent Halling, Richard W. Aldrich, and Carlos R. Baiz. 2018. "Coordination to Lanthanide Ions Distorts Binding Site Conformation in Calmodulin." *Proceedings of the National Academy of Sciences of the United States of America* 115 (14): E3126–34. https://doi.org/10.1073/pnas.1722042115.

Ellwood, D. C. 1970. "The Wall Content and Composition of Bacillus Substilis Var. Niger Grown in a Chemostat." *The Biochemical Journal* 118 (3): 367–73. https://doi.org/10.1042/bj1180367.

Emmanuel, E. S.Challaraj, T. Ananthi, B. Anandkumar, and S. Maruthamuthu. 2012. "Accumulation of Rare Earth Elements by Siderophore-Forming Arthrobacter Luteolus Isolated from Rare Earth Environment of Chavara, India." *Journal of Biosciences* 37 (1): 25–31. https://doi.org/10.1007/s12038-011-9173-3.

Fein, Jeremy B. 2000. "Quantifying the Effects of Bacteria on Adsorption Reactions in Water-Rock Systems." *Chemical Geology* 169 (3–4): 265–80. https://doi.org/10.1016/S0009-

2541(00)00207-2.

———. 2006. “Thermodynamic Modeling of Metal Adsorption onto Bacterial Cell Walls: Current Challenges.” *Advances in Agronomy* 90 (06): 179–202. https://doi.org/10.1016/S0065-2113(06)90005-4.

Fein, Jeremy B., Jean François Boily, Nathan Yee, Drew Gorman-Lewis, and Benjamin F. Turner. 2005. “Potentiometric Titrations of Bacillus Subtilis Cells to Low PH and a Comparison of Modeling Approaches.” *Geochimica et Cosmochimica Acta* 69 (5): 1123–32. https://doi.org/10.1016/j.gca.2004.07.033.

Fein, Jeremy B., Christopher J. Daughney, Nathan Yee, and Thomas A. Davis. 1997. “A Chemical Equilibrium Model for Metal Adsorption onto Bacterial Surfaces.” *Geochimica et Cosmochimica Acta* 61 (16): 3319–28. https://doi.org/10.1016/S0016-7037(97)00166-X.

Fein, Jeremy B., Aaron M. Martin, and Peter G. Wightman. 2001. “Metal Adsorption onto Baterial Surfaces: Development of a Predictive Approach.” *Geochimica et Cosmochimica Acta* 65 (23): 4267–73. https://doi.org/10.1016/S0016-7037(01)00721-9.

Feng, Yi, Asher Schmidt, and R. A. Weiss. 1996. “Compatibilization of Polymer Blends by Complexation. 1. Spectroscopic Characterization of Ion-Amide Interactions in Ionomer/Polyamide Blends.” *Macromolecules* 29 (11): 3909–17. https://doi.org/10.1021/ma951722r.

Ferreira, Izabella C.C., Emília M.G. Aguiar, Alinne T.F. Silva, Letícia L.D. Santos, Léia Cardoso-Sousa, Thaise G. Araújo, Donizeti W. Santos, et al. 2020. “Attenuated Total Reflection-Fourier Transform Infrared (ATR-FTIR) Spectroscopy Analysis of Saliva for Breast Cancer Diagnosis.” *Journal of Oncology* 2020. https://doi.org/10.1155/2020/4343590.

Genuchten, M. Th., Dalton, F.N. Van. 1986. “Models for Simulating Salt Movement in Aggregated Field Soils.” *Geoderma* 38: 165–83.

Gholivand, Khodayar, Mohammad Kahnouji, Yazdan Maghsoud, Ehsan Masumian, and Mahdieh Hosseini. 2018. “A Theoretical Study on the Coordination Behavior of Some Phosphoryl, Carbonyl and Sulfoxide Derivatives in Lanthanide Complexation.” *Journal of Molecular Modeling* 24 (11). https://doi.org/10.1007/s00894-018-3865-7.

Goldberg, S. 1992. “ScienceDirect - Advances in Agronomy : Use of Surface Complexation Models in Soil Chemical Systems.” *Advances in Agronomy*. http://linkinghub.elsevier.com/retrieve/pii/S0065211308604927%5Cnpapers2://publication/uuid/01C9419F-EEDD-41C0-B69D-7F9DCA1404F7.

Gram, and C. 1884. “Ueber Die Isolirte Farbung Der Schizomyceten in Schnitt-Und Trockenpraparaten.” *Fortschritte Der Medicin* 2: 185–89. http://ci.nii.ac.jp/naid/10010576549/en/.

Guiné, V., L. Spadini, G. Sarret, M. Muris, C. Delolme, J. P. Gaudet, and J. M.F. Martins. 2006. “Zinc Sorption to Three Gram-Negative Bacteria: Combined Titration, Modeling, and EXAFS Study.” *Environmental Science and Technology* 40 (6): 1806–13. https://doi.org/10.1021/es0509811.

Haas, Johnson R., Thomas J. Dichristina, and Roy Wade. 2001. “Thermodynamics of U(VI) Sorption onto Shewanella Putrefaciens.” *Chemical Geology* 180 (1–4): 33–54. https://doi.org/10.1016/S0009-2541(01)00304-7.

Haas, Johnson R., Everett L. Shock, and David C. Sassani. 1995. “Rare Earth Elements in Hydrothermal Systems: Estimates of Standard Partial Molal Thermodynamic Properties of Aqueous Complexes of the Rare Earth Elements at High Pressures and Temperatures.” *Geochimica et Cosmochimica Acta* 59 (21): 4329–50. https://doi.org/10.1016/0016-7037(95)00314-P.

Hatano, Tomonobu, and Takehiko Tsuruta. 2017. “Removal and Recovery of Chromium(III) from Aqueous Chromium(III) Using <I>Arthrobacter Nicotianae</I> Cells.” *Advances in Microbiology* 07 (06): 487–97. https://doi.org/10.4236/aim.2017.76038.

Heinrich, Hannah T M, Phil J Bremer, Christopher J Daughney, and A James Mcquillan. 2007. “Acid - Base Titrations of Functional Groups on the Surface of the Thermophilic Bacterium Anoxybacillus Fla W Ithermus : Comparing a Chemical Equilibrium Model with ATR-IR Spectroscopic Data,” no. 10: 2731–40. https://doi.org/10.1021/la062401j.

Hong, Yongsuk, and Derick G. Brown. 2006. “Cell Surface Acid-Base Properties of Escherichia Coli and Bacillus Brevis and Variation as a Function of Growth Phase, Nitrogen Source and C:N Ratio.” *Colloids and Surfaces B: Biointerfaces* 50 (2): 112–19. https://doi.org/10.1016/j.colsurfb.2006.05.001.

Humphries, Marc. 2013. “Rare Earth Elements:The Global Supply Chain.” http://fas.org/sgp/crs/natsec/R41347.pdf.

Jiang, Wei, Anuradha Saxena, Bongkeun Song, Bess B. Ward, Terry J. Beveridge, and Satish C.B. Myneni. 2004. “Elucidation of Functional Groups on Gram-Positive and Gram-Negative Bacterial Surfaces Using Infrared Spectroscopy.” *Langmuir* 20 (26): 11433–42. https://doi.org/10.1021/la049043+.

Kamenopoulos, Sotiris N., Deborah Shields, and Zacharias Agioutantis. 2015. *Sustainable Development Criteria and Indicators for the Assessment of Rare Earth Element Mining Projects*. *Rare Earths Industry: Technological, Economic, and Environmental Implications*. Elsevier Inc. https://doi.org/10.1016/B978-0-12-802328-0.00006-1.

Kang, Xia, Laszlo Csetenyi, and Geoffrey Michael Gadd. 2019. “Biotransformation of Lanthanum by Aspergillus Niger.” *Applied Microbiology and Biotechnology* 103 (2): 981–93. https://doi.org/10.1007/s00253-018-9489-0.

Kinniburgh, David G., Cooper, David M. 2019. “Phreeplot-Creating Graphical Output with PHREEQC.” http://www.phreeplot.org.

Kolat, Robert Stanley. 1970. “A Study of the Rare-Earth Metal Complexes,” no. 1961.

Komeili, Arash. 2012. “Molecular Mechanisms of Compartmentalization and Biomineralization in Magnetotactic Bacteria.” *FEMS Microbiology Reviews* 36 (1): 232–55. https://doi.org/10.1111/j.1574-6976.2011.00315.x.

Laveuf, Cédric, Sophie Cornu, and Farid Juillot. 2008. “Rare Earth Elements as Tracers of Pedogenetic Processes.” *Comptes Rendus - Geoscience* 340 (8): 523–32.

https://doi.org/10.1016/j.crte.2008.07.001.

Long, Keith R., Bradley S. Van Gosen, Nora K. Foley, and Daniel Cordier. 2012. "The Principal Rare Earth Elements Deposits of the United States: A Summary of Domestic Deposits and a Global Perspective." *Non-Renewable Resource Issues: Geoscientific and Societal Challenges*, 131–55. https://doi.org/10.1007/978-90-481-8679-2_7.

Loukidou, M. X., T. D. Karapantsios, A. I. Zouboulis, and K. A. Matis. 2005. "Cadmium(II) Biosorption by Aeromonas Caviae: Kinetic Modeling." *Separation Science and Technology* 40 (6): 1293–1311. https://doi.org/10.1081/SS-200052207.

Maleke, Maleke, Angel Valverde, Jan G. Vermeulen, Errol Cason, Alba Gomez-Arias, Karabelo Moloantoa, Liza Coetsee-Hugo, Hendrik Swart, Esta Van Heerden, and Julio Castillo. 2019. "Biomineralization and Bioaccumulation of Europium by a Thermophilic Metal Resistant Bacterium." *Frontiers in Microbiology* 10 (JAN): 1–10. https://doi.org/10.3389/fmicb.2019.00081.

Markai, S., Y. Andrès, G. Montavon, and B. Grambow. 2003. "Study of the Interaction between Europium (III) and Bacillus Subtilis: Fixation Sites, Biosorption Modeling and Reversibility." *Journal of Colloid and Interface Science* 262 (2): 351–61. https://doi.org/10.1016/S0021-9797(03)00096-1.

Martelli, Fausto, Sacha Abadie, Jean Pierre Simonin, Rodolphe Vuilleumier, and Riccardo Spezia. 2013. "Lanthanoids(III) and Actinoids(III) in Water: Diffusion Coefficients and Hydration Enthalpies from Polarizable Molecular Dynamics Simulations." *Pure and Applied Chemistry* 85 (1): 237–46. https://doi.org/10.1351/PAC-CON-12-02-08.

Martin, Langdon J., Martin J. Hähnke, Mark Nitz, Jens Wöhnert, Nicholas R. Silvaggi, Karen N. Allen, Harald Schwalbe, and Barbara Imperiali. 2007. "Double-Lanthanide-Binding Tags: Design, Photophysical Properties, and NMR Applications." *Journal of the American Chemical Society* 129 (22): 7106–13. https://doi.org/10.1021/ja070480v.

Martinez, Raul E., Olivier Pourret, and Yoshio Takahashi. 2014. "Modeling of Rare Earth Element Sorption to the Gram Positive Bacillus Subtilis Bacteria Surface." *Journal of Colloid and Interface Science* 413: 106–11. https://doi.org/10.1016/j.jcis.2013.09.037.

Mayne, Leland C., and Bruce Hudson. 1991. "Resonance Raman Spectroscopy of N-Methylacetamide: Overtones and Combinations of the C-N Stretch (Amide II′) and Effect of Solvation on the C=O Stretch (Amide I) Intensity." *Journal of Physical Chemistry* 95 (8): 2962–67. https://doi.org/10.1021/j100161a006.

McCarthy, John F., and John M. Zachara. 1989. "Subsurface Transport of Contaminants." *Environmental Science and Technology* 23 (5): 496–502. https://doi.org/10.1021/es00063a001.

Mishra, Bhoopesh, Elizabeth Shoenfelt, Qiang Yu, Nathan Yee, Jeremy B. Fein, and Satish C.B. Myneni. 2017. "Stoichiometry of Mercury-Thiol Complexes on Bacterial Cell Envelopes." *Chemical Geology* 464: 137–46. https://doi.org/10.1016/j.chemgeo.2017.02.015.

Moriwaki, Hiroshi, Reiko Masuda, Yuki Yamazaki, Kaoru Horiuchi, Mari Miyashita, Jun Kasahara, Tatsuhito Tanaka, and Hiroki Yamamoto. 2016. "Application of Freeze-Dried

Powders of Genetically Engineered Microbial Strains as Adsorbents for Rare Earth Metal Ions." *ACS Applied Materials and Interfaces* 8 (40): 26524–31. https://doi.org/10.1021/acsami.6b08369.

Moriwaki, Hiroshi, and Hiroki Yamamoto. 2013. "Interactions of Microorganisms with Rare Earth Ions and Their Utilization for Separation and Environmental Technology." *Applied Microbiology and Biotechnology* 97 (1): 1–8. https://doi.org/10.1007/s00253-012-4519-9.

Naumann, D. 1984. "Some Ultrastructural Information on Intact, Living Bacterial Cells and Related Cell-Wall Fragments as given by FTIR." *Infrared Physics* 24 (2–3): 233–38. https://doi.org/10.1016/0020-0891(84)90075-7.

Ngwenya, Bryne T., Marisa Magennis, Valerie Olive, J. Fred W. Mosselmans, and Robert M. Ellam. 2010. "Discrete Site Surface Complexation Constants for Lanthanide Adsorption to Bacteria as Determined by Experiments and Linear Free Energy Relationships." *Environmental Science and Technology* 44 (2): 650–56. https://doi.org/10.1021/es9014234.

Ngwenya, Bryne T., J. Fred W. Mosselmans, Marisa Magennis, Kirk D. Atkinson, Janette Tourney, Valerie Olive, and Robert M. Ellam. 2009. "Macroscopic and Spectroscopic Analysis of Lanthanide Adsorption to Bacterial Cells." *Geochimica et Cosmochimica Acta* 73 (11): 3134–47. https://doi.org/10.1016/j.gca.2009.03.018.

Ngwenya, Bryne T., Ian W. Sutherland, and Lynn Kennedy. 2003. "Comparison of the Acid-Base Behaviour and Metal Adsorption Characteristics of a Gram-Negative Bacterium with Other Strains." *Applied Geochemistry* 18 (4): 527–38. https://doi.org/10.1016/S0883-2927(02)00118-X.

Nitz, Mark, Manashi Sherawat, Katherine J. Franz, Ezra Peisach, Karen N. Allen, and Barbara Imperiali. 2004. "Structural Origin of the High Affinity of a Chemically Evolved Lanthanide-Binding Peptide." *Angewandte Chemie - International Edition* 43 (28): 3682–85. https://doi.org/10.1002/anie.200460028.

Ozaki, Takuo, Yoshinori Suzuki, Takuya Nankawa, Takahiro Yoshida, Toshihiko Ohnuki, Takaumi Kimura, and Arokiasamy J. Francis. 2006. "Interactions of Rare Earth Elements with Bacteria and Organic Ligands." *Journal of Alloys and Compounds* 408–412: 1334–38. https://doi.org/10.1016/j.jallcom.2005.04.142.

Panak, By P J, J Raff, G Geipel, G Bernhard, and H Nitsche. 2000. "Complex Formation of U (VI) with Bacillus -Isolates from a Uranium Mining Waste Pile," no. September 2016. https://doi.org/10.1524/ract.2000.88.2.071.

Park, Dan M., Aaron Brewer, David W. Reed, Laura N. Lammers, and Yongqin Jiao. 2017. "Recovery of Rare Earth Elements from Low-Grade Feedstock Leachates Using Engineered Bacteria." *Environmental Science and Technology* 51 (22): 13471–80. https://doi.org/10.1021/acs.est.7b02414.

Park, Dan M., David W. Reed, Mimi C. Yung, Ali Eslamimanesh, Malgorzata M. Lencka, Andrzej Anderko, Yoshiko Fujita, Richard E. Riman, Alexandra Navrotsky, and Yongqin Jiao. 2016. "Bioadsorption of Rare Earth Elements through Cell Surface Display of Lanthanide Binding Tags." *Environmental Science and Technology* 50 (5): 2735–42. https://doi.org/10.1021/acs.est.5b06129.

Park, Dan, Andrew Middleton, Ryan Smith, Gauthier Deblonde, Dan Laudal, Nolan Theaker, Heileen Hsu-Kim, and Yongqin Jiao. 2020. “A Biosorption-Based Approach for Selective Extraction of Rare Earth Elements from Coal Byproducts.” *Separation and Purification Technology* 241 (February): 116726. https://doi.org/10.1016/j.seppur.2020.116726.

Park, Hyung Jun, and Lawrence L. Tavlarides. 2010. “Adsorption of Neodymium(III) from Aqueous Solutions Using a Phosphorus Functionalized Adsorbent.” *Industrial and Engineering Chemistry Research* 49 (24): 12567–75. https://doi.org/10.1021/ie100403b.

Peng, Liu, Liu Yi, Lu Zhexue, Zhu Juncheng, Dong Jiaxin, Pang Daiwen, Shen Ping, and Qu Songsheng. 2004. “Study on Biological Effect of La3+ on Escherichia Coli by Atomic Force Microscopy.” *Journal of Inorganic Biochemistry* 98 (1): 68–72. https://doi.org/10.1016/j.jinorgbio.2003.08.012.

Pranata Putra, Wiwid, Azlan Kamari, Siti Najiah Mohd Yusoff, Che Fauziah Ishak, Azmi Mohamed, Norhayati Hashim, and Illyas Md Isa. 2014. “Biosorption of Cu(II), Pb(II) and Zn(II) Ions from Aqueous Solutions Using Selected Waste Materials: Adsorption and Characterisation Studies.” *Journal of Encapsulation and Adsorption Sciences* 04 (01): 25–35. https://doi.org/10.4236/jeas.2014.41004.

Price, R. C., C. M. Gray, R. E. Wilson, F. A. Frey, and S. R. Taylor. 1991. “The Effects of Weathering on Rare-Earth Element, Y and Ba Abundances in Tertiary Basalts from Southeastern Australia.” *Chemical Geology* 93 (3–4): 245–65. https://doi.org/10.1016/0009-2541(91)90117-A.

Rabie, K. A., S. A. Sayed, T. A. Lasheen, and I. E. Salama. 2007. “Europium Separation from a Middle Rare Earths Concentrate Derived from Egyptian Black Sand Monazite.” *Hydrometallurgy* 86 (3–4): 121–30. https://doi.org/10.1016/j.hydromet.2006.10.007.

Rao, P. S.C., D. E. Rolston, R. E. Jessup, and J. M. Davidson. 1980. “Solute Transport in Aggregated Porous Media: Theoretical Experimental Evaluation.” *Soil Science Society of America Journal* 44 (6): 1139–46. https://doi.org/10.2136/sssaj1980.03615995004400060003x.

Raynaud, Xavier, and Naoise Nunan. 2014. “Spatial Ecology of Bacteria at the Microscale in Soil.” *PLoS ONE* 9 (1). https://doi.org/10.1371/journal.pone.0087217.

Roden, Eric E., and Timothy D. Scheibe. 2005. “Conceptual and Numerical Model of Uranium(VI) Reductive Immobilization in Fractured Subsurface Sediments.” *Chemosphere* 59 (5): 617–28. https://doi.org/10.1016/j.chemosphere.2004.11.007.

Rotter, B. E., D. A. Barry, J. I. Gerhard, and J. S. Small. 2008. “Modeling U(VI) Biomineralization in Single- and Dual-Porosity Porous Media.” *Water Resources Research* 44 (8). https://doi.org/10.1029/2007WR006301.

Sigel, Helmut, and R. Bruce Martin. 1982. “Coordinating Properties of the Amide Bond. Stability and Structure of Metal Ion Complexes of Peptides and Related Ligands.” *Chemical Reviews* 82 (4): 385–426. https://doi.org/10.1021/cr00050a003.

Sposito, Gary. 2016. “The Chemistry of Soils.” *Oxford University Press*, no. Third Edition.

Takahashi, Yoshio, Xavier Châtellier, Keiko H. Hattori, Kenji Kato, and Danielle Fortin. 2005.

"Adsorption of Rare Earth Elements onto Bacterial Cell Walls and Its Implication for REE Sorption onto Natural Microbial Mats." *Chemical Geology* 219 (1–4): 53–67. https://doi.org/10.1016/j.chemgeo.2005.02.009.

Takahashi, Yoshio, Mika Yamamoto, Yuhei Yamamoto, and Kazuya Tanaka. 2010a. "EXAFS Study on the Cause of Enrichment of Heavy REEs on Bacterial Cell Surfaces." *Geochimica et Cosmochimica Acta* 74 (19): 5443–62. https://doi.org/10.1016/j.gca.2010.07.001.

———. 2010b. "EXAFS Study on the Cause of Enrichment of Heavy REEs on Bacterial Cell Surfaces." *Geochimica et Cosmochimica Acta* 74 (19): 5443–62. https://doi.org/10.1016/j.gca.2010.07.001.

Tan, K. L., and B. H. Hameed. 2017. "Insight into the Adsorption Kinetics Models for the Removal of Contaminants from Aqueous Solutions." *Journal of the Taiwan Institute of Chemical Engineers* 74 (April): 25–48. https://doi.org/10.1016/j.jtice.2017.01.024.

Texier, A. C., Y. Andrés, M. Illemassene, and P. Le Cloirec. 2000. "Characterization of Lanthanide Ions Binding Sites in the Cell Wall of Pseudomonas Aeruginosa." *Environmental Science and Technology* 34 (4): 610–15. https://doi.org/10.1021/es990668h.

Thomas, Kieth J., and Charles V. Rice. 2015. "Equilibrium Binding Behavior of Magnesium to Wall Teichoic Acid." *Biochimica et Biophysica Acta - Biomembranes* 1848 (10): 1981–87. https://doi.org/10.1016/j.bbamem.2015.05.003.

Tourney, Janette, Bryne T Ngwenya, J W Fred Mosselmans, Laurence Tetley, and Gregory L Cowie. 2008. "The Effect of Extracellular Polymers (EPS) on the Proton Adsorption Characteristics of the Thermophile Bacillus Licheniformis S-86" 247: 1–15. https://doi.org/10.1016/j.chemgeo.2007.09.012.

Tsuruta, Takehiko. 2005. "Removal and Recovery of Lithium Using Various Microorganisms." *Journal of Bioscience and Bioengineering* 100 (5): 562–66. https://doi.org/10.1263/jbb.100.562.

Tukker, Arnold. 2014. "Rare Earth Elements Supply Restrictions: Market Failures, Not Scarcity, Hamper Their Current Use in High-Tech Applications." *Environmental Science and Technology* 48 (17): 9973–74. https://doi.org/10.1021/es503548f.

Tyler, Germund. 2004. "Rare Earth Elements in Soil and Plant Systems - A Review." *Plant and Soil* 267 (1–2): 191–206. https://doi.org/10.1007/s11104-005-4888-2.

Vázquez-Ortega, Angélica, Julia Perdrial, Adrian Harpold, Xavier Zapata-Ríos, Craig Rasmussen, Jennifer McIntosh, Marcel Schaap, et al. 2015. "Rare Earth Elements as Reactive Tracers of Biogeochemical Weathering in Forested Rhyolitic Terrain." *Chemical Geology* 391: 19–32. https://doi.org/10.1016/j.chemgeo.2014.10.016.

Walter, A. L., E. O. Frind, D. W. Blowes, C. J. Ptacek, and J. W. Molson. 1994. "Modeling of Multicomponent Reactive Transport in Groundwater: 1. Model Development and Evaluation." *Water Resources Research* 30 (11): 3137–48. https://doi.org/10.1029/94WR00955.

Wang, Zimeng, and Daniel E Giammar. 2013. "Mass Action Expressions for Bidentate Adsorption in Surface Complexation Modeling : Theory and Practice," no. 2.

Watson, E.B. 1980. “Some Experimentally Determined Zircon/Liquid Partition Coefficients for the Rare Earth Elements.” *Geochimica et Cosmochimica Acta* 44: 895 to 897.

Wightman, Peter G., Jeremy B. Fein, David J. Wesolowski, Tommy J. Phelps, Pascale Bénézeth, and Donald A. Palmer. 2001. “Measurement of Bacterial Surface Protonation Constants for Two Species at Elevated Temperatures.” *Geochimica et Cosmochimica Acta* 65 (21): 3657–69. https://doi.org/10.1016/S0016-7037(01)00763-3.

Wood, Scott A. 2001. “Behavior of Rare Earth Element In Geothermal Systems: A New Exploration / Exploitation Tool,” 1–95.

Wood, Scott A., David J. Wesolowski, and Donald A. Palmer. 2000. “The Aqueous Geochemistry of the Rare Earth Elements IX. A Potentiometric Study of Nd3+ Complexation with Acetate in 0.1 Molal NaCl Solution from 25°C to 225°C.” *Chemical Geology* 167 (1–2): 231–53. https://doi.org/10.1016/S0009-2541(99)00210-7.

Yee, Nathan, and Jeremy B. Fein. 2002. “Does Metal Adsorption onto Bacterial Surfaces Inhibit or Enhance Aqueous Metal Transport? Column and Batch Reactor Experiments on Cd-Bacillus Subtilis-Quartz Systems.” *Chemical Geology* 185 (3–4): 303–19. https://doi.org/10.1016/S0009-2541(01)00412-0.

Yu, Qiang, and Jeremy B. Fein. 2015. “The Effect of Metal Loading on Cd Adsorption onto Shewanella Oneidensis Bacterial Cell Envelopes: The Role of Sulfhydryl Sites.” *Geochimica et Cosmochimica Acta* 167: 1–10. https://doi.org/10.1016/j.gca.2015.06.036.

Yung, Mimi C., and Yongqin Jiao. 2014. “Biomineralization of Uranium by PhoY Phosphatase Activity Aids Cell Survival in Caulobacter Crescentus.” *Applied and Environmental Microbiology* 80 (16): 4795–4804. https://doi.org/10.1128/AEM.01050-14.

Zaharescu, Dragos G, Carmen I Burghelea, Katerina Dontsova, Jennifer K Presler, Raina M Maier, Travis Huxman, Kenneth J Domanik, et al. 2017. “Ecosystem Composition Controls the Fate of Rare Earth Elements during Incipient Soil Genesis,” no. February: 1–15. https://doi.org/10.1038/srep43208.

Zdravkova, Videlina, Nikola Drenchev, Elena Ivanova, Mihail Mihaylov, and Konstantin Hadjiivanov. 2015. “Surprising Coordination Chemistry of Cu+ Cations in Zeolites: FTIR Study of Adsorption and Coadsorption of CO, NO, N2, and H2O on Cu-ZSM-5.” *Journal of Physical Chemistry C* 119 (27): 15292–302. https://doi.org/10.1021/acs.jpcc.5b03213.

Zhang, X. C., M. A. Nearing, V. O. Polyakov, and J. M. Friedrich. 2003. “Using Rare-Earth Oxide Tracers for Studying Soil Erosion Dynamics.” *Soil Science Society of America Journal* 67 (1): 279–88. https://doi.org/10.2136/sssaj2003.2790.

Zhou, Jingwei, Jinglan Wu, Yanan Liu, Fengxia Zou, Jian Wu, Kechun Li, Yong Chen, Jingjing Xie, and Hanjie Ying. 2013. “Modeling of Breakthrough Curves of Single and Quaternary Mixtures of Ethanol, Glucose, Glycerol and Acetic Acid Adsorption onto a Microporous Hyper-Cross-Linked Resin.” *Bioresource Technology* 143: 360–68. https://doi.org/10.1016/j.biortech.2013.06.009.

Appendix 1. Phreeplot script for acid-base titration modeling of *A. nicotianae*

```
CHEMISTRY

SELECTED_OUTPUT
    -high_precision true
    -reset false

SURFACE_MASTER_SPECIES
Slyrphosdi SlyrphosdiOH  #phosphodiester site
Slyrcarb  SlyrcarbOH     #carboxyl site
Slyrphos SlyrphosOH      #phosphoryl site
Slyramine SlyramineH+    #amine site

SURFACE_SPECIES

SlyrphosdiOH = SlyrphosdiOH
  log_k 0

SlyrphosdiOH = SlyrphosdiO- + H+
  log_k <log_k1>

SlyrcarbOH = SlyrcarbOH
  log_k 0

SlyrcarbOH = SlyrcarbO- + H+
  log_k <log_k2>

SlyrphosOH = SlyrphosOH
  log_k 0

SlyrphosOH = SlyrphosO- + H+
  log_k <log_k3>

SlyramineH+ = SlyramineH+
  log_k 0

SlyramineH+ = Slyramine + H+
  log_k <log_k4>
```

```
SOLUTION 1 # 0.1 M HCl titrant
units mol/L
temp 25.0
pH 12 charge
Na 0.1
-water <L_titrant>
save SOLUTION 1

SOLUTION 2 #solution of bacteria
units mol/L
temp 25.0
pH <pH_start>
Na 0.1
Cl 0.1
-water <L_solution>
save SOLUTION 2

MIX 1
1 1
2 1
save SOLUTION 3

SURFACE 1
-sites_units density
Slyrphosdi <site_density1> 197 0.32 # sites/nm^2, m^2/dry g, dry g
-ccm 8
Slyrcarb <site_density2> 197 0.32
-ccm 8
Slyrphos <site_density3> 197 0.32
-ccm 8
Slyramine <site_density4> 197 0.32
-ccm 8
save SURFACE 1
```

Appendix 2. Phreeplot script for optimization of Nd-stability constants in a 4-site constant capacitance model characterization of *A. nicotianae* biosorption

```
CHEMISTRY

PHASES

Fix_H+
H+ = H+
log_k 0.0

SURFACE_MASTER_SPECIES
Slyrphosdi SlyrphosdiOH          #phosphodiester site
Slyrcarb  SlyrcarbOH             #carboxyl site
Slyrphos  SlyrphosOH             #phosphoryl site
Slyramine SlyramineH+            #amine site
Slyrcarbonylm SlyrcarbonylmO-    #carbonyl-based amide site

## Surface protonation ##

SURFACE_SPECIES

SlyrphosdiOH = SlyrphosdiOH
  log_k 0

SlyrphosdiOH = SlyrphosdiO- + H+
  log_k -2.1


SlyrcarbOH = SlyrcarbOH
  log_k 0

SlyrcarbOH = SlyrcarbO- + H+
  log_k -4.17


SlyrphosOH = SlyrphosOH
  log_k 0

SlyrphosOH = SlyrphosO- + H+
  log_k -6.88


SlyramineH+ = SlyramineH+
  log_k 0

SlyramineH+ = Slyramine + H+
  log_k -9.48

SlyrcarbonylmO- = SlyrcarbonylmO-
  log_k 0
```

```
## Surface adsorption of REE ##

SlyrphosdiO- + Nd+3 = Nd(SlyrphosdiO)+2
  log_k <log_k0>

2SlyrcarbO- + Nd+3 = Nd(SlyrcarbO)2+
  log_k <log_k1>

SlyrphosO- + Nd+3 = Nd(SlyrphosO)+2
  log_k <log_k2>

SlyrcarbonylmO- + Nd+3 = NdSlyrcarbonylmO+2
  log_k <log_k3>

SURFACE 1
-sites_units density #absolute
Slyrphosdi 0.58 197 0.0001575
-ccm 8
Slyrcarb 0.76 197 0.0001575
-ccm 8
Slyrphos 0.24 197 0.0001575
-ccm 8
Slyramine 0.72 197 0.0001575
-ccm 8
Slyrcarbonylm <site1> 197 0.0001575
### site1 = 2.26*(10^-3)*<n_experiment> ###
-ccm 8
save SURFACE 1

EQUILIBRIUM_PHASES 1
 Fix_H+  -6  NaOH 0.01
 save Equilibrium_Phases 1

EQUILIBRIUM_PHASES 2
 Fix_H+  -5  NaOH 0.01
 save Equilibrium_Phases 2

EQUILIBRIUM_PHASES 3
 Fix_H+  -4  NaOH 0.01
 save Equilibrium_Phases 3
```